

Erik Andreas Jørgensen

Fischer-Tropsch Synthesis: Conversion of Bio-Syngas to Hydrocarbons

Master's thesis in Chemical Engineering

Supervisor: Edd Anders Blekkan

June 2019

Erik Andreas Jørgensen

Fischer-Tropsch Synthesis: Conversion of Bio-Syngas to Hydrocarbons

Master's thesis in Chemical Engineering
Supervisor: Edd Anders Blekkan
June 2019

Norwegian University of Science and Technology
Faculty of Natural Sciences
Department of Chemical Engineering



Norwegian University of
Science and Technology

Sammendrag

Dette prosjektet omhandler Fischer-Tropsch syntese over cobolt-baserte katalysatorer. Tolv eksperimenter ble utført i en to-reaktor rigg ved en rekke reaksjonsbetingelser, med formål om å innhente eksperimentell data til modellering og tilpasning av en mekanistisk modell for Fischer-Tropsch syntese. Totalt 3500 timer med eksperimenter ble gjennomført hvor effektene av syntesegassammensetning, temperatur, reaksjonstid, eksternt tilsatt vann og regenerering ble undersøkt. To katalysatorer ble testet, en syntetisert på laboratoriet ved våtimpregnering og en kommersiell type katalysator anskaffet fra Equinor – begge med formulering 20 %Co0.5 %Re/ γ -Al₂O₃.

Katalysatorene ble karakterisert ved røntgendiffraksjon, N₂-fysisorpsjon, H₂-kjemisorpsjon og temperaturprogrammert reduksjon, og siden resultatene for de separate katalysatorene kun viste små forskjeller i katalytiske egenskaper var det derfor forventet at de også ville vise omtrent lik ytelse i Fischer-Tropsch-sammenheng. Det ble imidlertid observert forskjeller i både selektivitet og robusthet overfor deaktivering. Gitt at de to katalysatorene hadde samme formulering ble det foreslått at de observerte forskjellene kunne tilegnes forskjellige forhold under katalysatorsyntese.

Den kommersielle typen katalysator ble valgt for videre undersøkelse og eksperimenter ved forskjellige reaksjonsbetingelser ble utført. Disse forsøkene viste at kinetisk aktivitet, selektivitet og deaktiveringsgrad var avhengig av både temperaturen og fødegassammensetningen. Det ble også funnet at både temperatur og fødegassammensetning påvirket den kinetiske responsen til eksternt tilsatt vann, og derfor foreslått at reaksjonsbetingelsene i tillegg til poreegenskaper dikterer responsen. En lineær deaktiveringsfunksjon ble observert å være tilstrekkelig i korte eksperimenter (> 160 timer), mens deaktivering observert over lengre tidsrammer lignet en to-trinns deaktivering. Sintering ble foreslått som den viktigste deaktiveringsmekanismen i de tidlige stadier av operasjon, med en kombinasjon av reoksidasjon og karbonavleiring som de viktigste deaktiveringsmekanismene ved langsiktig drift. Et lineært forhold mellom temperaturen og deaktiveringsraten ble observert. Basert på den katalytiske aktiviteten i eksperimentene utført ved forskjellige temperaturer ble aktiveringsenergien for Fischer-Tropsch-syntese beregnet å være i området 90-95 kJ/mol.

To regenereringsprosedyrer ble forsøkt på katalysatoren, men ingen nevneverdig forbedring av katalytisk aktivitet ble observert. Det beste resultatet ble oppnådd ved regenereringsprosedyren som innebar flushing av reaktorene ved driftstrykk- og temperatur før reduksjon, hvor en 15% økning i kinetisk aktivitet ble observert. På grunn av den dårlige effekten av regenerering ble det foreslått at en oksidativ regenereringsprosedyre hvor katalysatoren kalsineres før reduksjon ville gi et bedre resultat.

Abstract

Fischer-Tropsch synthesis over cobalt-based catalysts has been performed experimentally in this project. Twelve experiments were conducted in a two-reactor fixed-bed rig at a range of reaction conditions, with the purpose of obtaining experimental data that could be used in the development and fitting of a mechanistic model. The total experimental run-time clocked into about 3500 hours, where the effects of all synthesis gas composition, temperature, reaction time, externally added water and catalyst regeneration were investigated. Two catalysts were tested, one synthesized *in-house* (standard catalyst) by incipient wetness impregnation and one commercial type catalyst procured from Equinor – both being 20%Co0.5%Re/ γ -Al₂O₃.

The catalysts were characterized by X-ray diffraction, N₂ physisorption, H₂ chemisorption, and temperature-programmed reduction, displaying only small discrepancies in the catalytic properties, indicating that the catalysts should exhibit similar performance results. However, during Fischer-Tropsch synthesis, both differences in selectivities and robustness towards deactivation were observed. Given that the two catalysts had the same formulation, it was suggested that the observed differences could be due to different conditions during catalyst synthesis.

The commercial type catalyst was chosen for further investigation, and experiments at a variety of reaction conditions were performed. These experiments revealed that all kinetic activity, selectivity, and rate of deactivation were dependent on both the temperature and the feed gas composition. It was also found that both the temperature and feed gas composition influences the kinetic response to externally added water, and hence suggested that reaction conditions in addition to pore characteristics dictate the response. Linear deactivation functions were observed to be sufficient in short experiments (>160 hours), while the deactivation observed over longer time frames resembled a two-step deactivation. Sintering was proposed as the main deactivation mechanism relevant in the early stages of operation, with a combination of re-oxidation and coking as the main deactivation mechanisms for long-term operation. A linear relationship between the temperature and the rate of deactivation was observed. Based on the catalytic activity of the three experiments, the activation energy for Fischer-Tropsch synthesis was calculated to be in the range 90-95 kJ/mol.

Two catalyst regeneration procedures were attempted. Neither was able to rejuvenate the catalytic activity noteworthy. The best result was obtained when purging the reactor systems at operating pressure and temperature before reduction, whereas a 15% increase in kinetic activity was observed. Due to the poor effect of regeneration, it was suggested that an oxidative regeneration procedure in which the catalyst is calcined prior to reduction would yield a better result.

Preface

This thesis is a part of the course TKP4900; Chemical Process Technology Master's Thesis, a 21-week-long project-based course culminating in this final report. The thesis is a continuation of the specialization project course TKP4580 conducted during the autumn of 2018, and therefore are parts of the results presented in this thesis obtained during that course. This is mentioned in the text where it is relevant. Several technical challenges arose during the execution of the experimental work associated with the thesis. The main challenge was associated with a malfunctioning gas chromatograph, which held the work back for three weeks in the initial phase of the project. Other issues encountered include faulty mass flow controllers and discrepancies regarding the composition of the synthesis gas that was ordered. Disregarding the technical issues, a total of 3500 hours of experiments were performed and considering that the overall goal of this work was to obtain experimental data for kinetic modeling of Fischer-Tropsch synthesis on cobalt catalysts, it is tempting to declare the experimental work a success. The work was carried out at the Department of Chemical Engineering at the Norwegian University of Science and Technology (NTNU).

I would like to manifest my utter and wholehearted gratitude to Post-Doc Ljubiša Gavrilović for his excellent guidance and cooperation associated with the experimental work in this thesis. Furthermore, I want to express my sincerest admiration and recognition of the unfathomable knowledge on the Fischer-Tropsch process of my supervisor Professor Edd Anders Blekkan, whose mentoring and assistance has been second to none. Thanks also goes out to Research Scientist at SINTEF Rune Myrstad for his much appreciated technical help with the operation rig, and to the collaboratory 'modelling guys' Adjunct Professor Erling Rytter, Professor Magne Hillestad, Adjunct Associate Professor and Research Scientist at SINTEF Kumar R. Rout, Post-Doc Poteswara R. Putta, Ph.D Candidate Umesh Pandey, and Master Student Anders Runningen for letting me in on your fruitful discussions during group meetings.

Table of Contents

Sammendrag	i
Abstract	iii
Preface	v
Table of Contents	ix
List of Tables	xi
List of Figures	xiv
Symbols	xv
Abbreviations	xvii
1 Introduction	1
2 Theory	7
2.1 Fischer-Tropsch Synthesis	7
2.1.1 Reaction Mechanism	7
2.1.2 Catalysts	9
2.1.3 Product Distribution	12
2.1.4 Reactors	13
2.2 Catalyst Preparation	16
2.2.1 Incipient Wetness Impregnation	16

2.2.2	Drying	16
2.2.3	Calcination	16
2.3	Catalyst Characterization	17
2.3.1	X-Ray Diffraction	17
2.3.2	H ₂ Chemisorption	18
2.3.3	N ₂ Physisorption	19
2.3.4	Temperature-Programmed Reduction	21
2.4	Catalyst Performance	22
2.4.1	Activity	22
2.4.2	Selectivity	23
2.4.3	Stability	23
2.5	Gas Chromatography	24
3	Experimental	27
3.1	Catalyst Preparation	27
3.2	Catalyst Characterization	28
3.2.1	X-ray Diffraction	28
3.2.2	H ₂ Chemisorption	28
3.2.3	N ₂ Physisorption	29
3.2.4	Temperature-Programmed Reduction	29
3.3	Fischer-Tropsch Synthesis	29
3.3.1	Apparatus	29
3.3.2	Procedure	30
4	Results and Discussion	35
4.1	Catalyst Characterization	35
4.1.1	X-ray Diffraction & H ₂ Chemisorption	35
4.1.2	N ₂ Physisorption	37
4.1.3	Temperature-Programmed Reduction	38
4.2	Fischer-Tropsch Synthesis	39
4.2.1	Comparison of Catalysts	39
4.2.2	Effect of Temperature	43

4.2.3	Effect of Reaction Time	46
4.2.4	Effect of Feed Gas Composition	50
4.2.5	Catalyst Regeneration	54
4.2.6	Water-Gas Shift Activity	58
4.2.7	Observations Relevant for All Experiments	61
5	Conclusion and Further Work	65
	Appendices	75
A	Sample Calculations	77
A.1	Catalyst Synthesis Calculations	77
A.2	Calculation of Liquid Flow Rate of Water	78
A.3	Calculations of Activity and Selectivities	79
A.3.1	Experimental Data	79
A.3.2	Selectivity Calculations	81
A.3.3	Calculation of Site Time Yield	86
B	Additional Experimental Data	87
B.1	Effect of Reaction Time, 230 °C	87
C	Raw Data	89
C.1	Adsorption/Desorption Curves	89
D	Python Code	91
D.1	Main Script	91
D.1.1	Function: Collecting the Experimental Data	93
D.1.2	Function: Collecting the Feed Gas Analysis Data	96
D.1.3	Function: Collecting the GC Calibration Data	97
D.1.4	Function: Making All Calculations	99
E	Risk Assessment	105

List of Tables

3.1	Reaction conditions for the various experiments	32
4.1	Characterization results, XRD and H ₂ chemisorption	36
4.2	Characterization results, N ₂ physisorption	37
4.3	Activity and selectivity, catalyst comparison	40
4.4	Activity and selectivities, effect of reaction time	48
4.5	Olefin-to-paraffin ratios, effect of reaction time	49
4.6	Water effect, effect of feed gas composition	52
4.7	Activity and selectivities, effect of feed gas composition	53
4.8	Olefin-to-paraffin ratios, catalyst regeneration – LPR procedure	55
4.9	Selectivities, catalyst regeneration – OCR procedure	56
4.10	Catalyst performance, simulated conversion	63
5.1	Summary of effects	66
A.1	Pore volume of the support	77
A.2	TCD data for calculating the activity and selectivity	79
A.3	FID data for calculating the activity and selectivity	80
A.4	Feed gas analysis and calibration data	80
A.5	Experimental data for calculating the activity and selectivity.	80

List of Figures

1.1	Biomass conversion routes	2
2.1	Carbide and enol mechanisms	8
2.2	Chain propagation	9
2.3	Chain termination	9
2.4	Chain-growth probability	13
2.5	Fluidized bed reactors for Fischer-Tropsch synthesis	14
2.6	Fixed-bed and slurry type reactors for Fischer-Tropsch synthesis	15
2.7	Schematic illustration of the Bragg equation	17
2.8	Langmuir isotherm	19
2.9	Schematic illustration of a BET isotherm	20
2.10	Typical activity trend for a catalytic process	23
2.11	Schematic illustration of a gas chromatograph	25
4.1	X-ray diffractograms	35
4.2	Pore size distributions	37
4.3	TPR profiles	38
4.4	Activity and selectivity, catalyst comparison	39
4.5	Olefin-to-paraffin ratio, catalyst comparison	41
4.6	Deactivation, catalyst comparison	42
4.7	Deactivation, effect of temperature	43
4.8	Selectivity, effect of temperature	44
4.9	Olefin-to-paraffin ratios, effect of temperature	44

4.10	Arrhenius plot	45
4.11	Course of experiment, effect of reaction time – 210 °C	46
4.12	Deactivation, effect of reaction time	48
4.13	Deactivation, effect of feed gas composition – 210 °C	50
4.14	Deactivation, effect of feed gas composition – 230 °C	51
4.15	Effect of adding water, effect of feed gas composition	52
4.16	Activity and selectivity, catalyst regeneration – LPR procedure	54
4.17	Activity and selectivity, catalyst regeneration – OCR procedure	56
4.18	WGS activity, indigenous water	58
4.19	WGS activity, external and indigenous water	59
4.20	Selectivity variation with conversion	61
4.21	Selectivity variation with simulated high conversions	62
A.1	Sample chromatogram	79
B.1	Course of experiment, effect of reaction time – 230 °C	87
C.1	Adsorption/desorption curves	89

Symbols

α	Chain growth probability	n	Order of reflection
β	Peak width	n_m	Number of moles that covers the monolayer
θ	Angle	n_x	Number of moles of x
λ	Wavelength	N_A	Avogadro's number
ρ	Specific mass	p	Pressure
σ	Surface tension	p_0	Saturated vapor pressure
σ_{N_2}	Cross-section area of N_2	P_{ref}	Reference pressure
A_x^{cali}	Area of peak of x from calibration	p_x	Pressure of component x
A_x^{FGA}	Area of peak of x from feed gas analysis	r	Pore radius
A_x^{FID}	Area of FID peak of x in the sample	r_P	Rate of propagation
A_x^{TCD}	Area of TCD peak of x in the sample	r_T	Rate of termination
c	Constant	r_X	Reaction rate based on component X
d	Lattice spacing	R	Universal gas constant
d_p	Particle size	RRF_x	Relative response factor of x
$d_p(x)$	Particle size of x	S_{BET}	BET surface area
S	Surface area	S_Y	Selectivity for formation of component Y
D	Dispersion	T	Temperature
f	Fraction of exposed surface	T_{ref}	Reference temperature
F	One-atom coverage	v_{ads}	Adsorbed volume
F_{new}	New flow rate	V	Volume
F_{old}	Previous flow rate of syngas	v_{id}	Ideal gas volume
F_{syngas}	Total flow of syngas	V_m	Volume of an adsorbed monolayer
F_X	Flow rate of component X	w_i	Weight fraction of chain length i
$F_{X,o}$	Feed flow rate of component X	$W_{cat.}$	Total mass of catalyst
i	Number of carbon atoms	x_x	Weight fraction of component x
k	A constant	X_{new}	Desired conversion
L_{hkl}	Crystallite thickness	X_{old}	Previous registered conversion
m	Mass	X_X	Conversion of component X
m_x	Mass of component x	Y_X	Percentage of component X in the feed
M_m	Molar mass	Y_x^{cali}	Volume fraction of x in calibration bottle
M_S	Surface metal atom	Y_x^{feed}	Volume fraction of x in syngas bottle
M_X	Molar mass of component X		

Abbreviations

ASF	Anderson-Schulz-Flory
BET	Brunauer-Emmet-Teller
BJH	Barret-Joyner-Halenda
BTL	Biomass-to-Liquids
CTL	Coal-to-Liquids
FID	Flame Ionization Detector
FT(S)	Fischer-Tropsch (Synthesis)
FWHM	Full Width at Half Maximum
GC	Gas Chromatograph
GTL	Gas-to-liquids
HTFT	High Temperature Fischer-Tropsch
IWI	Incipient Wetness Impregnation
IWP	Incipient Wetness Point
LFC	Liquid Flow Controller
LPR	Low Pressure Regeneration
LTFT	Low Temperature Fischer-Tropsch
MFC	Mass Flow Controller
MS	Mass Spectrometer
OCR	Operating Conditions Regeneration
PC	Pressure Controller
P&ID	Piping and Instrumentation Diagram
SEM	Scanning Electron Microscopy
STY	Site Time Yield
TCD	Thermal Conductivity Detector
TEM	Transmission electron microscopy
TOF	Turnover Frequency
TOS	Time on Stream
TPR	Temperature-Programmed Reduction
WGS	Water-Gas Shift
XPS	X-ray Photoelectron Spectroscopy
XRD	X-Ray Diffraction

Introduction

Access to sustainable and clean energy is a major challenge of our time. The substantial growth in global population the past century is projected to increase further in the foreseeable future, and the worldwide energy demand correspondingly.^[1] The energy demand is estimated to increase by 28 % by the year 2040, with the transportation sector covering a major portion of the overall consumption^{[2][3]}. According to a study by Centre for Sustainable Energy Studies (CenSES), the proportion of the total global energy use associated with the transportation sector is expected to grow additionally in the future.^[4] The increased global energy exploitation adheres to higher greenhouse gas emissions. The average concentration of CO₂ in the atmosphere has increased by about 40 % since the mid-1800s, at an increased rate the past 10 years, culminating in average growth of 2 ppm/year.^[3]

Thus, the current global energy scenario and the environmental deterioration aspect highly motivate the substitution of fossil fuels with renewable energy resources. Particularly of interest is finding sources of fuels that can be implemented directly into existing networks of distribution, meaning that the continuation of liquid fuels is auspicious.^[5]

Cellulosic biomass exists in great abundance and points out as a possible source. Conversion of biomass to liquid fuels may proceed by either of the routes shown in Figure 1.1, by hydrolysis to form aqueous sugars or lignin, by pyrolysis to form bio-oils or by gasification to form syngas.^[6] Liquid fuels produced via the Fischer-Tropsch process from biomass-derived syngas promises an attractive, clean, carbon-neutral and sustainable energy source.^{[7][8]} And according to the well-to-wheel report by the European Commission Joint Research Centre^[9], biofuels produced by Fischer-Tropsch synthesis are among the bio-derived fuels with the lowest life cycle anthropogenic CO₂ emissions. Besides, since biomass is considered carbon-neutral, this pathway is especially of interest, both in environmental and economic terms.^[10]

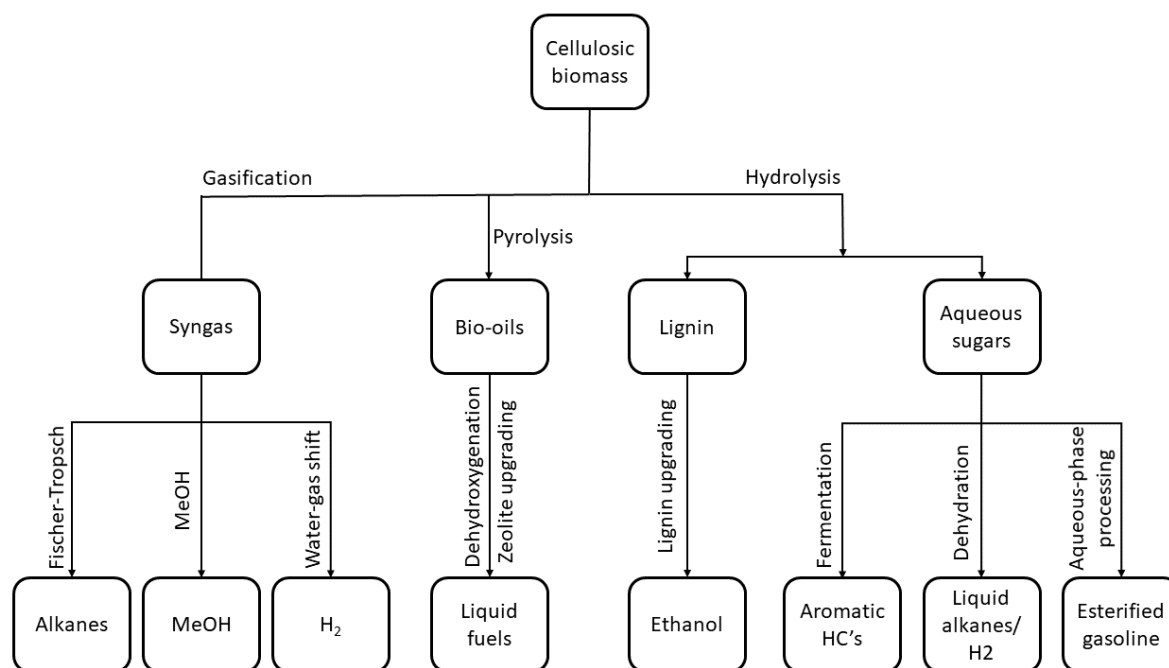


Figure 1.1: Biomass conversion routes. Figure adapted from “Progress in biofuel production from gasification”.^[11]

The Fischer-Tropsch synthesis converts synthesis gas (syngas) into a wide range of hydrocarbons such as diesel, gasoline and other aliphatic hydrocarbons. In addition to the aforementioned pathway for syngas production – gasification of biomass – syngas may also be derived from natural gas and coal. The related processes of producing liquid fuels from the respective sources are typically abbreviated GTL (gas-to-liquids), CTL (coal-to-liquids) and BTL (biomass-to-liquids).

Depending on the origin of the feedstock, the purity and composition of the syngas may vary, however, the Fischer-Tropsch products are only dependent on the catalyst and the process conditions.^[12] Both the GTL and CTL are already established processes, but the complex nature of biomass composition gives rise to several challenges regarding the economic viability of a potential BTL plant. Biomass contains a range of species that is undesired in the Fischer-Tropsch process, for instance, due to their deactivating effects on the FT catalyst, e.g. alkali species, sulfur, ammonia and hydrogen cyanide for Co catalysts.^{[13][14][15]} The syngas purification steps are therefore of great importance in regards to BTL production.

Fischer-Tropsch synthesis on cobalt catalysts have been subject to thorough investigations since Fischer and his co-workers developed the first cobalt FT catalyst in the 1920s-1930s.^[16] These investigations have shown that cobalt-based catalysts are of particular interest for industrial applications due to their significant specifications. A cobalt-based catalyst displays high activity at low temperatures, high selectivity towards long-chained alkanes, high resistance to deactivation and long life-time. Compared to iron-based catalysts, which also have been investigated thoroughly in affiliation with Fischer-Tropsch synthesis, the cobalt-based catalyst have catalyst durability of up to 5 years, opposed to about 6 months for the iron catalyst.^[17]

This project is part of a collaborative project called “Bio Fischer-Tropsch (BioFT) – Staging and Multiple Hydrogen Feed of Biomass to Fischer-Tropsch Fuel Synthesis”, which aims at developing a Fischer-Tropsch kinetic model for reactor design. The objective of this thesis is to obtain experimental data from the Fischer-Tropsch synthesis that can be used in the kinetic model, where the effect of water – which is formed as a by-product in the FTS – is of particular interest, since it has been found that water has a significant positive impact on the formation of heavy hydrocarbons.^{[18][19][20]} The experiments aim to encompass process conditions and their effects on the Fischer-Tropsch synthesis on rhenium promoted cobalt catalysts supported on γ -alumina (20 %Co0.5 %Re/ γ -Al₂O₃). The topical process conditions undergoing investigation are temperature, syngas conversion, reaction time, feed gas composition, and external water added in the feed. In addition, the effect of catalyst regeneration is investigated.

Already pointed out is the positive effect external water in the feed has on the formation of heavy hydrocarbons. The addition of external water is a common strategy for simulating high conversion levels without altering the residence time, as the partial pressure of water is increased. Doing so Storsæter *et al.*^[21] found both increased C₅₊ selectivity and decreased selectivity to methane on both promoted and unpromoted cobalt catalysts supported on all titania, silica, and alumina. The correlation between conversion level and selectivities was suggested to be a product of two separate effects; increased residence time and higher partial pressure of water. When the conversion level is increased at dry conditions (i.e. without adding water to the feed) the residence time is increased, with following higher probability of secondary reactions of primary products. In addition, the higher conversion leads to a higher partial pressure of water, which is proposed to have an inhibiting effect on the hydrogenation reactions.^[22] The latter instance is, therefore, the effect at work when simulating high conversions by adding water to the feed.

The effect of water on the kinetics, on the other hand, is more unpredictable. In the same paper, Storsæter *et al.* reported an increased rate of deactivation during their experiments, culminating in an effective drop in kinetic activity. In a review paper by Blekkan *et al.*^[23], the authors have collected and listed the effects from several different studies. The results are highly conflicting considering all positive, negative and neutral effects were reported. Borg *et al.*^[24] performed experiments on a set of catalysts only differing in pore characteristics, and also reported both positive and negative effects of external water on the kinetics. However, the positive effects were observed only for wide-pore catalysts, with the negative effects exclusive to narrow-pore catalysts. Their concluding remark was that the kinetic effect of external water was likely determined by the pore characteristics. This is supported by the work of Rytter *et al.*,^[25] who claimed that catalysts with broad pore size distributions were more susceptible to displaying negative effects of external water on the kinetics, while the opposite was true for catalysts with well-adapted pore size distributions, wide pores, and sufficiently large cobalt crystallites. The size of the cobalt particles is another factor highly influencing the selectivities, whereas Borg *et al.*^[26] found that the C₅₊ selectivity increased with increasing particle size, however, only up to about 8 nm, after which the selectivity dropped. Based on this there seems to exist an optimum in particle size of the cobalt where the C₅₊ fraction is maximized while the formation of light hydrocarbons is minimized.

The effect of feed gas composition on the kinetics of the Fischer-Tropsch synthesis is well

established, where the rate of reaction increases with increasing H_2/CO ratio.^[27] Based on the combined stoichiometry of the reactions taking place during Fischer-Tropsch synthesis, the consumption ratio is typically reported as 2.06:1 for $H_2:CO$. Hence, using synthesis gas ratios lower than that will cater hydrogen deficiency for the reactions, lowering the theoretical limit of CO conversion.^[28] Another ramification of this is shifts in the surface concentrations of adsorbed species, i.e. lower concentration of hydrogen and higher $-CH_2$ monomer concentration.^[29] This materializes in higher chain-growth probability and lower hydrogenation activity, consequently favoring the formation of olefins and heavier hydrocarbons prior to methane and saturated hydrocarbon chains. A. H. Lillebø^[30] reported a virtually linear relationship between the selectivity to C_{5+} and the syngas composition, in the range $H_2/CO = 2.55$ to 1.04.

The temperature is also an important factor that dictates both the kinetic activity and selectivity. Pendyala *et al.*^[31] performed experiments on aqueous-phase Fischer-Tropsch synthesis, in which they increased the temperature during the experiments. They observed a higher rate of formation of both methane and CO_2 and a lower rate of formation of heavier hydrocarbons when increasing the temperature. This was explained using thermodynamic considerations. The endothermic nature of the desorption process predicts that increasing the temperature favors a shift in the product slate towards shorter hydrocarbon chains, predominantly methane. Meaning that the lighter products display a higher degree of stability at elevated temperatures compared to heavier products. This covariance of temperature and selectivity to methane has been observed irrespective of the type of catalyst.^[32] Similarly does kinetic considerations via the Arrhenius equation predict that increased temperature leads to higher kinetic activity, i.e. higher CO conversion rate.^[33] One side effect of this is a higher degree of water formation, which accompanied by the higher temperature facilitates the formation of oxidized cobalt species, culminating in a higher activity for the water-gas shift reaction. The cycle ends with the H_2 that was formed in the WGS reaction reacting further in the Fischer-Tropsch reactions, balancing the syngas ratio, favoring the formation of methane.^[34] Another repercussion of this is the heightened formation of CO_2 . These effects are, however, heavily dependent on the temperature, and do not necessarily constitute a large contribution to the overall end products.

The kinetic stability of a cobalt FTS catalyst is determined by the rate of deactivation. Several deactivation mechanisms have been proposed, whereas two main mechanisms are somewhat observable during FTS experiments, namely re-oxidation of metallic cobalt and sintering.^[34] Water, as the most abundant product in Fischer-Tropsch synthesis, is an oxidizing agent, and although bulk oxidation of metallic cobalt is thermodynamically infeasible under realistic FTS conditions^[35], it has been calculated that highly dispersed cobalt particles smaller than 5 nm behaves differently than the bulk in these terms, and therefore may oxidize under conventional FT conditions.^[36] Re-oxidation causes phase transformation of metallic cobalt to FT inactive cobalt oxides, resulting in fewer active cobalt sites on the catalyst, thus negatively affecting the activity. Also, the re-structuring of the catalytic surface results in changes in the selectivities, whereas the cobalt oxides that are formed, for instance, facilitates the water-gas shift reaction, such that more CO_2 is formed in the reactions.^[37] Schanke *et al.*^[35] studied the role of water on deactivation on alumina supported cobalt Fischer-Tropsch catalysts and found that the addition of water to the feed led to significant deactivation. A large extent of re-oxidation of bulk cobalt was

only observed in hydrogen-free atmospheres, with hardly any re-oxidation when hydrogen was present. However, using XPS studies they observed significant surface oxidation of cobalt even at low $\text{H}_2\text{O}/\text{H}_2$ ratios and concluded that surface oxidation or oxidation of highly dispersed cobalt phases was responsible for the observed deactivation.

The exothermic nature of the FT reactions introduces a high potential for sintering. Sintering of cobalt particles leads to an overall reduction of the active surface area, culminating in lower reaction rates. Iglesia^[38] stated that small crystallites appear to be less active for the hydrogenation of CO than larger crystals, such that sintering of cobalt particles, i.e. increasing the crystallite size, also leads to alterations in selectivities. Both sintering and re-oxidation of cobalt particles are highly dependent on the temperature.^[34] Claeys *et al.*^[39] studied the impact of process conditions on sintering in Fischer-Tropsch synthesis on a platinum promoted alumina supported cobalt catalyst and used *in-situ* magnetic measurements to determine the change in the content of metallic cobalt in the catalyst bed during their experiments. The experiments were initially performed in a water-hydrogen atmosphere before CO was introduced after a certain time. Three different temperatures were studied, 210 °C, 220 °C and 230 °C, and they found that no sintering occurred in the pure water-hydrogen phase, whilst the introduction of CO led to immediate sintering. However, while feeding CO sintering appeared as a strong function of the partial pressure of water. Thus they suggested that the sintering mechanism may be CO assisted. They also found that the extent of sintering was more pronounced at elevated temperatures, that almost no sintering occurred at low CO partial pressures (> 1.0 bar), and that sintering seemed to come to a conclusion after around 24 h to 48 h time on stream. Hence, it appears that sintering is the preeminent deactivation mechanism in the early stages of operation. This phenomenon has also been reported by Sadeqzadeh *et al.*^[40], who designed deactivation models for FT catalysts. In these experiments, three models were used: 1) Sintering, 2) Oxidation, 3) Fouling by coking. The models were fitted to experimental data, suggesting that sintering was the main reason for initial deactivation, while a combination of surface oxidation and carbon deposition mainly caused long-term deactivation. The latter is substantiated by the work of Moodley *et al.*^[41], who studied catalyst deactivation by periodically sampling spent catalyst from a slurry bubble column reactor during 6 months of operation. The catalyst was cleaned with inert solvent to remove wax deposits before it was characterized by temperature-programmed hydrogenation and oxidation, chemisorption, and transmission electron microscopy (TEM). They found that carbon was present in both atomic and polymeric form, whereas the latter is determined to be resistant to hydrogen treatment at temperatures above FT synthesis temperature. Polymeric carbon was found both on the support and on cobalt, and the amount of polymeric carbon correlated well with observed long-term deactivation. Hence, they concluded that carbon deposition was the main cause of long-term deactivation.

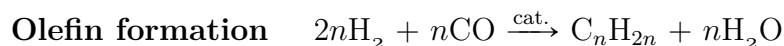
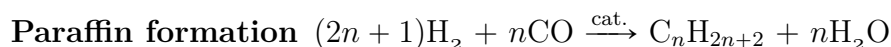
Although FT catalysts can be modified to preserve the catalytic activity for longer time frames, catalyst deactivation is inevitable. An important factor regarding the commercialization of catalytic processes is the durability of the catalyst, especially if the catalyst consists of noble metals or other precious compounds. Catalyst regeneration is a common strategy for maximizing the utility and the life span of a catalyst.^[33] Saib *et al.*^[42] studied the deactivation of a 20wt.% cobalt on alumina promoted with 0.5wt.% platinum over a time frame of 56 days, while operating at realistic conditions (230 °C, 20 bar, H_2/CO ratio of about 1.8 and at CO conversion levels of 50-70 %). After the 56 days of opera-

tion the catalyst was regenerated using an oxidative regeneration treatment, and doing so they successfully rejuvenated FTS performance of the spent catalyst to that of the fresh catalyst. Oxidation was claimed to be key to remove deposited carbon, whilst both the oxidation and reduction steps were suggested to be of great importance for the reversal of deactivation by sintering, as it re-disperses the sintered cobalt crystallites.

Theory

2.1 Fischer-Tropsch Synthesis

The Fischer-Tropsch synthesis is a process route for converting syngas (CO and H₂) to hydrocarbon products. It offers means to utilize coal, natural gas and/or biomass for production of liquid fuels such as gasoline, diesel, and wax.^[12] The two main classes of products from FTS are *paraffins* and *olefins*, with their respective chemical equations shown below.



The reactions are followed by secondary reactions that occur when primary products desorb and interact with new active sites. The secondary reactions include hydrogenation, insertion, hydrogenolysis, isomerization and cracking.^[33] The reaction conditions and choice of catalyst highly influence the product distribution, such that the process may be modified to produce large quantities of the desired products.

The FT reactions are highly exothermic, e.g. formation of one mole of $-\text{CH}_2$ generates approximately 165 kJ of heat.^[12] Therefore, a major consideration regarding FTS plants is the implementation of a heat exchange system to ensure ideal reaction conditions.

2.1.1 Reaction Mechanism

The Fischer-Tropsch synthesis is a surface polymerization reaction that occurs on the surface of the catalyst. In such reactions, it is often distinguished between the initiation step, chain-growth, and termination. The exact reaction mechanism to take place in the synthesis has been greatly debated and to this day there is no agreement on which one most accurately describes the process, and neither offers means to predict products under various conditions or produces satisfactory explanations of the observations made.^[43] Three main mechanisms have been proposed based on different monomer species. The *carbide* mechanism proposed by Fischer and Tropsch in 1926 was recognized for decades

after being publicized. It involves dissociation of CO to form metal carbide which is further hydrogenated to the monomer species CH_x . However, experimental work performed by Kummer et al.^[44] which included the use of radioactive ^{14}C isotopes as tracers in FTS proved that no more than 8-30 % of the methane formed as a result of the hydrogenation of metal carbide. This finding led most investigators to abandon the hypothesis of the formation of metal carbide as an intermediate in the FTS mechanism.^[45]

A new mechanism proposal was made around 1950 that was denoted *the enol* mechanism and received widespread acceptance. In this mechanism adsorbed CO reacts with surface hydrogen to form oxymethylene (CHOH), which further acts as the monomer species. It was later found that this mechanism was supported by the mentioned ^{14}C tracer experiments.^[46] In the 1970s the *CO insertion* mechanism was proposed.^[47] This mechanism involves the insertion of CO into a metal-methyl or metal-methylene carbon bond, followed by hydrogenation to form the final products.

In total, it is highly probable that all the aforementioned mechanisms contribute to some extent in the FTS, and it is likely that no single mechanism is capable of sufficiently describing the reactions taking place. In addition, there is evidence that the mechanism is different for all the various catalysts^[48], which present further complexity.

For simplification, only the *carbide* and the *enol* mechanisms will be presented in the following as a basis for the FTS. The initiation steps in both mechanisms are shown in Figure 2.1.

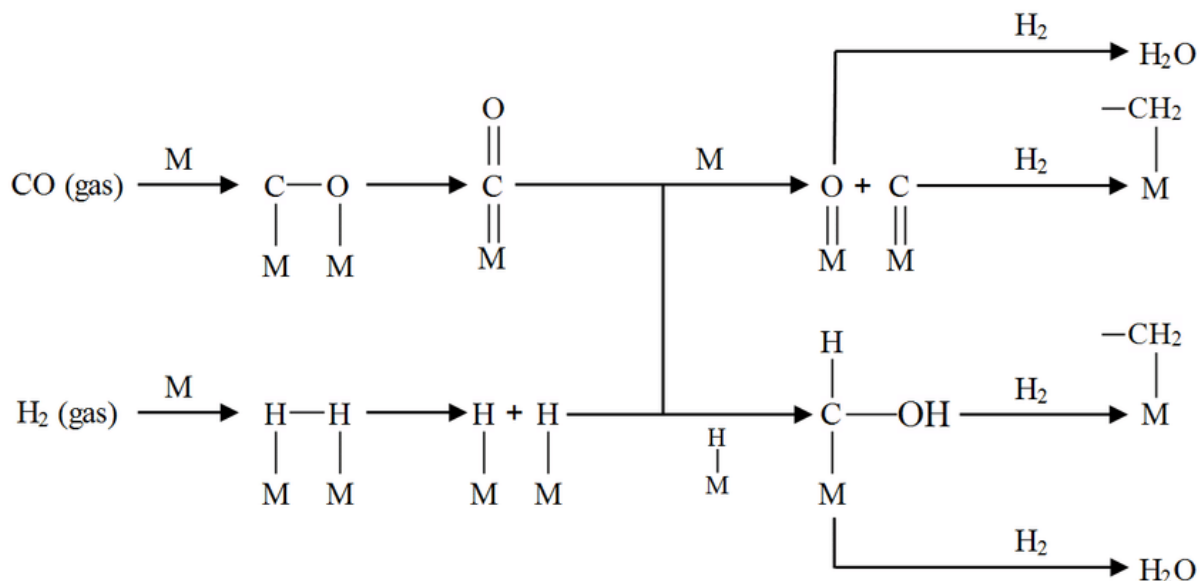


Figure 2.1: Carbide and enol mechanisms.^[49]

In the initiation step, CO is first adsorbed onto active sites on the surface of the catalyst. The CO can be either occupy two active sites by configuring in a bridge mode on the surface, or it may occupy one active site when associatively chemisorbed. It is assumed that the two modes are equilibrated. In the carbide mechanism, this step is followed by dissociation of the adsorbed CO to form surface C and surface O, before the initiation step is finalized by hydrogenation of the surface species to form surface methyl groups and water, respectively. In the enol mechanism, the chemisorbed CO does not, however,

dissociate, instead, it directly reacts with surface H to form surface CHOH, which further reacts with H₂ to form methyl groups and water. Simultaneously H₂, as the second reactant, is chemisorbed and dissociates on the surface, before it reacts with chemisorbed CO in a similar manner as described above.

The subsequent chain propagation follows the reaction path shown in Figure 2.3. The surface methyl groups initially react with each other in the propagation to form a chained hydrocarbon, which further reacts with new surface methyl groups causing the formation of long-chained hydrocarbons.

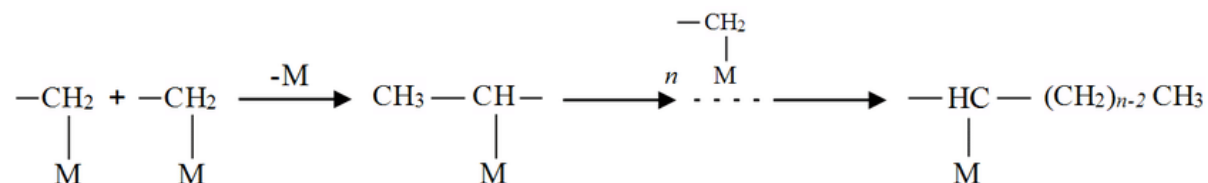


Figure 2.2: Chain propagation of the surface methyl monomers.^[49]

Chain termination, shown in Figure 2.2, most likely proceed via either of the following paths: paraffins are formed by either hydrogenation of the adsorbed surface alkyl group or combination with adsorbed CH₃, while olefins are formed by β-elimination of the hydrogen by reaction with an empty active site.

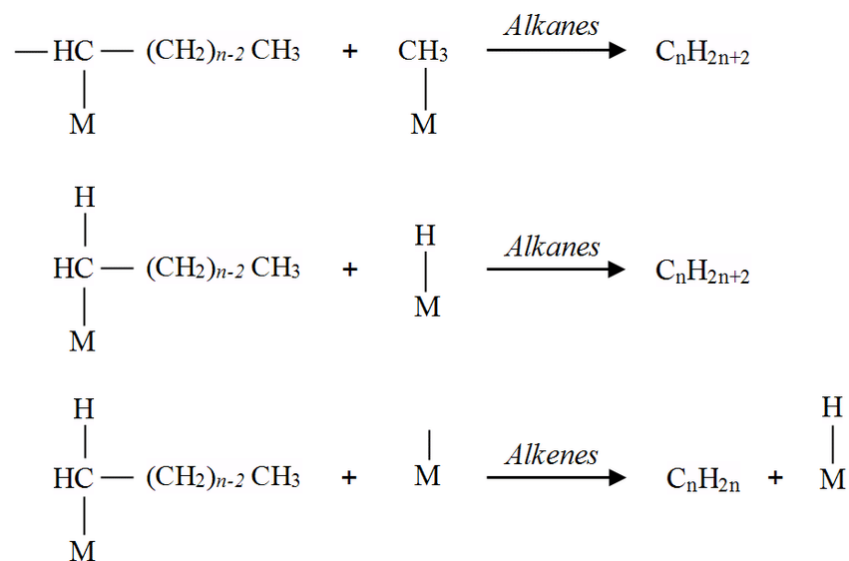


Figure 2.3: Probable routes for chain termination.^[49]

2.1.2 Catalysts

In order to warrant application of the Fischer-Tropsch synthesis, the catalyst of choice must have a high activity for the hydrogenation of carbon monoxide. It has been shown that iron, cobalt, nickel, and ruthenium all inherit this feature, however, the high cost and low availability of ruthenium metal eliminates it as a candidate for large-scale applications. Nickel catalysts also exhibit major drawbacks for this purpose; nickel facilitates

the formation of volatile carbonyls which results in a continuous loss of the active metal during the reaction, and – compared to cobalt and iron catalysts – the nickel catalyst produces much more of the less desirable product methane.^[50] Therefore, iron and cobalt catalysts are the only ones that are considered practically feasible in regards to process commercialization.

The iron and cobalt catalysts display different properties in regards to catalyst performance in FTS. Iron, for instance, has high activity towards the water-gas shift reaction shown below.



The water-gas shift (WGS) reaction plays a significant role in FTS over iron catalysts. In particular, it provides additional hydrogen for the reaction, which is a great advantage if the syngas used is derived from coal – which generally offers a low content of hydrogen in the syngas ($\text{H}_2/\text{CO} < 2$). Another advantage of having a high activity to the WGS reaction is, as the chemical equation illustrates, that it ensures the utilization of the carbon monoxide in the feed. This is imperative, as residue CO is unwanted in the product stream.^[12] In addition, the water-gas shift reaction influences the partial pressure of all the involved species, which may or may not be the desired effect. Cobalt catalysts, on the other hand, is often considered to have a negligible or low activity for the WGS reaction.^[34]

In general, iron catalysts generate more olefins and oxygenates than the cobalt catalyst. This is assumed to be linked to the less hydrogenating abilities of iron, which may be caused by the difference in active phase of the metal. While cobalt is active in its metallic state, iron changes during the reaction, making a complex mixture of iron carbides and oxides which then acts as the active phase.^[51]

Support Materials

The type and structure of the support influence the dispersion and consequently the activity of the FT catalyst system. The most frequently used supports that have been described in the literature are silica, titania, and alumina. These supports have great differences in properties and behave differently when cobalt is deposited, moreover, there are vast differences within each class of support. The differences are manifested as variations in activity and selectivity, and stability towards deactivation, e.g. re-oxidation by water.^{[25][20][49]} Main properties in regards to the support material are strength of interaction between the metal and the support, mechanical properties such as resistance to attrition, thermal stability, and porosity. Diffusion limitation is also a major topic related to the support characteristics. Under FTS reaction conditions, the catalyst pores are filled with liquid and wax products, and the reactants at the external catalyst surface dissolve in and subsequently diffuse through the liquids/waxes to reach the active sites of the catalyst. Due to hydrogen having a lower diffusion coefficient than carbon monoxide, the concentration of hydrogen inside the pores of the catalyst will be higher than that for CO.^[52] This phenomenon increases the H_2/CO ratio at the catalyst surface, accelerating chain termination, and thus negatively affects the chain length of the products. Although this is a concern in general, it has been shown that diffusion limitations are exclusive to

catalysts with pellet sizes larger than about 1 mm.^[53]

The silica support displays characteristics that attribute it to be an attractive candidate for the preparation of FT catalysts. These characteristics include large surface area, high surface-to-mass ratio, and high porosity.^[49] Titania, on the other hand, displays quite different characteristics compared to the silica support. Despite that, it also materializes as an attractive candidate, and titania has also been thoroughly studied for FTS purposes. Titania supports exhibit small surface area, high porosity and pore size, and high chemical and thermal tolerance. It has also been shown that titania interacts strongly with the cobalt particles, which contributes to this class of catalysts being additionally stable.^[54] The most common support for commercial cobalt supported catalysts is, however, alumina.^[55] The alumina support has rather complex crystal morphology and forms several polymorphs upon dehydration, two of which are typical supports under investigation for FTS, namely α -Al₂O₃ and γ -Al₂O₃. The α -Al₂O₃ support is characterized by excellent catalytic performance, however, due to the low surface area with corresponding low dispersion of cobalt on the support, and low tolerance for attrition, the support is considered inappropriate for large-scale FTS.^[56] γ -Al₂O₃, on the other hand, is characterized by excellent surface area owing to the small particle size and narrow pore size distribution, moreover, the material exhibit high thermal and chemical resistance^[57], and is perhaps *the* preferred support material for Fischer-Tropsch synthesis on cobalt catalysts.

Promoters

A typical strategy for enhancing certain desired properties of a supported catalyst is to add a promoter. The promoter may affect reducibility and/or dispersion of the active phase, cause structural alterations on the support material, prevent coke deposition, etc.^[33] In perspective of Fischer-Tropsch synthesis on cobalt supported on γ -alumina, noble metals such as platinum, palladium, ruthenium, and rhenium has been heavily subjected to investigation as it has been found that these metals facilitate increased reducibility of cobalt.^[21]^[58] Increased reducibility of the active phase gives a desired effect on the activity of the catalyst, which mainly is attributed to the increased number of surface cobalt atoms.^[35] The change in reducibility is suggested to be related to more rapid hydrogen activation when noble metals are present, with subsequent H₂ spillover to cobalt oxides and reduction of cobalt. Other effects of promoting the catalyst with noble metals are reduced cobalt particle size – both regarding metallic cobalt and cobalt oxide – and increased cobalt dispersion.^[54]^[59] Of all the aforementioned noble metal promoters, rhenium has shown to offer the proper trade-off between cost and usefulness for Fischer-Tropsch synthesis.

Catalyst Deactivation

Fischer-Tropsch catalysts are subjected to rather rough reaction conditions. The synthesis gas used often contains small amounts of impurities that act as a poison on the catalyst, perturbing its properties.^[34] Conventional Fischer-Tropsch reaction conditions include high pressures and moderate to high temperatures, and the atmosphere is a mixture of

gases and liquids that all necessarily affects the solid catalyst in one way or another. The catalyst is, therefore, a dynamic material that changes continuously during the reaction. Several deactivation mechanisms have been proposed for Fischer-Tropsch synthesis on cobalt-based catalysts, and the main ones from literature are^[42]: poisoning by sulphur and/or nitrogen-containing compounds in the synthesis gas; oxidation of the active cobalt metal to inactive oxides; formation of cobalt-support compounds, e.g. cobalt aluminates; sintering of small cobalt crystallites; surface reconstruction and; carbon formation. An important factor in the deactivation is the water vapor that is formed in the FT reaction. Water vapor may affect all sintering, surface oxidation of cobalt particles, and the formation of FT inactive cobalt-support compounds.^[60] The continuous cycle of oxidation and reduction of the cobalt surface atoms renders re-arrangement of the cobalt atoms (sintering), resulting in a continuous loss of surface area and thereby loss of activity.

2.1.3 Product Distribution

A key parameter for estimating the product distribution of the FTS is the chain-growth probability, α . It is defined as the fraction of the chain-growth rate (rate of propagation) to the overall turnover rate (rate of propagation + rate of termination), as presented in Equation 2.1.

$$\alpha = \frac{r_P}{r_P + r_T} \quad (2.1)$$

where r_P and r_T is the rate of propagation and termination, respectively. Both rates are typically dependent on several physical factors, including chain length and process conditions like pressure, temperature and reactant concentrations. If the dependency on chain length is neglected the Anderson-Schultz-Flory (ASF) distribution equation may be derived^[12]:

$$w_i = i(1 - \alpha)^2 \alpha^{i-1} \quad (2.2)$$

where w_i is the weight fraction of chain length i , i is the number of carbon atoms and α is the chain-growth probability. Figure 2.4 illustrates the ideal product distribution as a function of the chain-growth probability.

The various Fischer-Tropsch catalysts display wide differences in the α -value associated with them. The nickel catalyst has a small α -value and thus predominantly produces methane. The classical iron catalyst typically has an α -value in the range 0.60-0.70, yielding an optimum in the C₅-C₈ range, which corresponds to the gasoline area. The cobalt catalyst, however, displays higher values of α typically in the range 0.75-0.85, producing longer chains of hydrocarbons.^[12] In all instances, the α is dependent on the process conditions, and a common strategy is to modify the conditions to bring α as close to unity as possible and then perform hydrocracking of the long molecules to obtain products with the desired lengths.

The dependency of the Fischer-Tropsch synthesis on the reaction conditions can be exemplified by considering the effects of increased reaction temperature. Elevating the

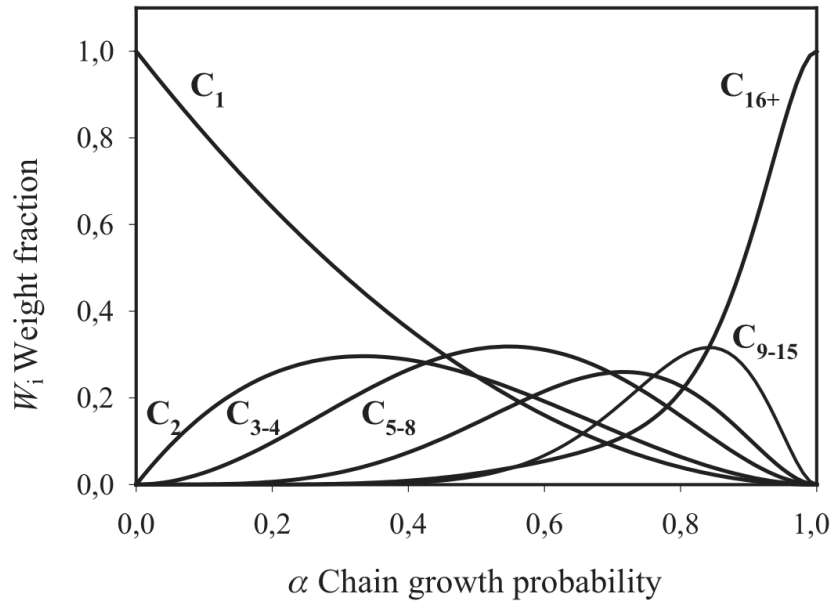


Figure 2.4: Weight fractions of lumps of hydrocarbons as function of α .^[12]

temperature leads to undesired effects such as increased methane formation, reduction in the average chain length of the products and it also favors carbon deposition and other deactivation mechanisms. However, it also results in desired effects such as increased reaction rate and improved quality of the steam produced in the heat removal system associated with the reactor.^[51] In addition, the effects of the various reaction conditions are interrelated, hence, optimization of FT technology involves a great number of compromises.

2.1.4 Reactors

There are four types of Fischer-Tropsch reactors that are in commercial use today.^[51] The different types are:

- Circulating fluidized bed reactor
- Fixed/turbulent fluidized bed reactor
- Slurry phase reactor
- Tubular fixed bed reactor

An important factor regarding the operation of FT synthesis plants is the operating temperature. A common distinction is to distinguish between high-temperature Fischer-Tropsch (HTFT) and low-temperature Fischer-Tropsch (LTFT) processes. Fluidized bed reactors are preferred reactors for operation in the HTFT regime, where the temperature is maintained at a level that prohibits condensation of products, leaving no liquid phase present outside the catalyst particles. If liquids actually were formed in the fluidized bed, particle agglomeration would cause severe problems and loss of fluidization.^[61] On the contrary, the fixed bed and the slurry phase reactor are operated within the LTFT regime, a temperature level that permits the formation of liquid products, i.e. heavy

hydrocarbons in the form of liquid wax. Typical temperature ranges for HTFT and LTFT are 320 °C to 350 °C and 220 °C to 250 °C, respectively. Iron catalysts are candidates for both HTFT and LTFT, but cobalt supported catalysts are limited to LTFT operation.^[62]

The two fluidized bed reactors – which are operated in the HTFT regime – currently in operation are one circulating fluidized bed reactor and one fixed/turbulent fluidized bed reactor, illustrated in Figure 2.5.

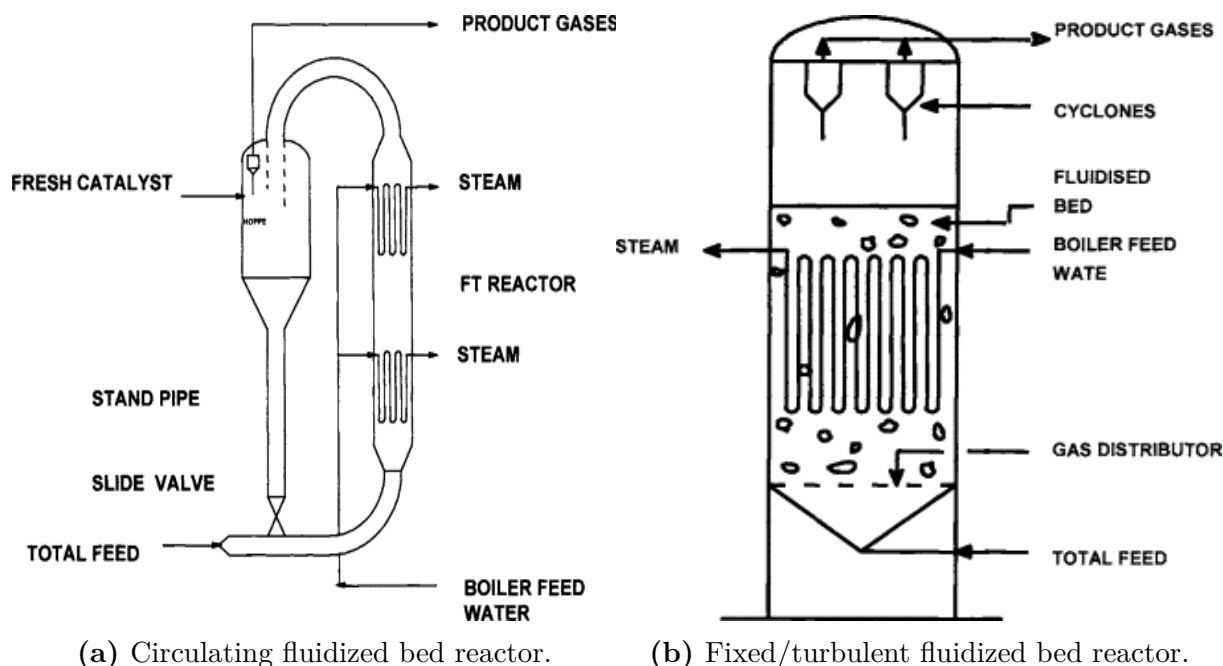


Figure 2.5: Two types of fluidized bed reactors for Fischer-Tropsch synthesis in the HTFT regime.^[51]

Both reactors are examples of two-phase reactors, in which the solid catalyst acts as one phase whilst the gaseous feed and products act as the second phase. Due to the exothermic nature of the reactions taking place in the Fischer-Tropsch synthesis, it is crucial to design reactors that can cope with high degrees of heat exchange. This is one of the advantageous traits with the fluidized bed reactors. In these reactors, there is a high degree of turbulence in the reactor beds, ensuring high levels of heat exchange. This trait contributes to the reactor beds being virtually isothermal.^[51] A disadvantage associated with these reactors is that poisons in the feed will be subjected to the entire catalyst mass and therefore have a larger overall deactivating effect than for instance for the fixed bed reactor – where the feed runs through the bed and only will deactivate the part of the catalyst bed it is first exposed to.

In the slurry phase reactor, illustrated in Figure 2.6a, the catalyst particles are suspended in the liquid products from the FT reaction and the feed gas is sparged through the slurry to evenly distribute the reactants. This reactor type is far more efficient than the fixed-bed reactor, in which it achieves the same activity levels with only one-third of the catalyst mass.^[51] This is explained by the FT reaction rate being pore diffusion-limited, hence the smaller particles used in the slurry phase reactor increases the activity of the reaction. The separation of the catalyst particles and the liquid product is, however, an issue in this case.

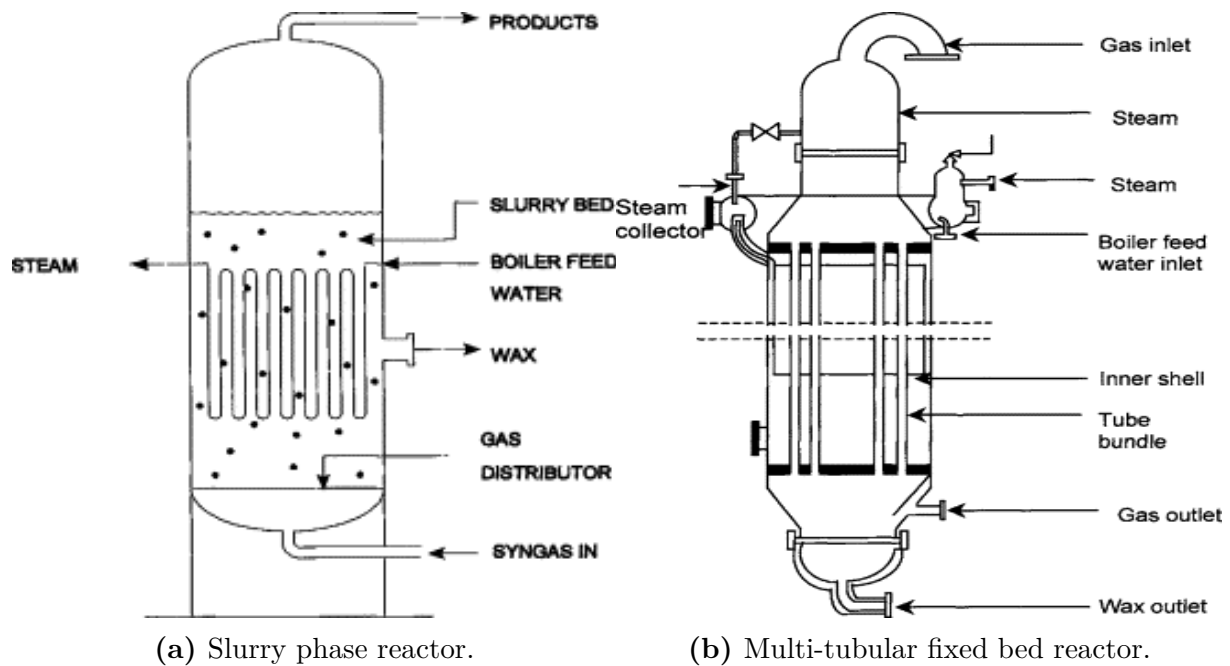


Figure 2.6: Two types of reactors for Fischer-Tropsch synthesis in the LTFT regime.^[51]

The tubular fixed bed reactor operating in the LTFT regime is only a viable choice for large-scale operation if several compromises are brought out. To have sufficient heat transfer in the reactor tubes to ensure isothermal (or as close to isothermal as possible) conditions, the distance from the catalyst particles to the tube walls ought to be short, which means that the tube diameters must be narrow. Similarly, the linear gas velocity should be high to obtain turbulent flow inside the tubes. Also, to achieve high conversion levels the catalyst particles should be small, as more of the surface is exposed to the reactants in this case. The combination of these factors: narrow tubes, high linear gas velocities, and small particles results in high differential pressure over the length of the reactor. Therefore there must be made compromises between the design and the operation of the reactor, even though it inevitably results in axial and radial temperature gradients, i.e. not optimal operation conditions for the reactions.^[51] This is also the reason why tubular fixed bed reactors cannot be utilized in high-temperature operation; high reaction temperature yields large amounts of carbon deposition on the catalyst, which eventually will cause blocking of the narrow tubes. There are however advantages using this type of reactor above the fluidized bed and the slurry phase reactor; the separation of products is simple since the liquid product trickles down the bed and is easily collected in a knock-out pot, and the scaling from pilot to industrial scale is simple and allows accurate predictions of the performance of an industrial-sized reactor based on pilot-scale experiments. The simple design and modeling of such reactors are reasons why this is the preferred reactor type in lab-scale experiments.

2.2 Catalyst Preparation

2.2.1 Incipient Wetness Impregnation

Incipient wetness impregnation (IWI) is a method for depositing metal particles onto a support material. The procedure involves adding an amount of solvent that exactly equilibrates the total pore volume of the support, obtaining incipient wetness of the material. First, the support material is pre-treated by either drying or calcination before IWI to remove residual moisture. Then the incipient wetness point (IWP) of the support is determined by dropwise addition of a solvent with known density, commonly distilled or de-ionized water. At the point when the solvent starts to wet the support, the IWP is obtained, and the overall pore volume can be determined by the amount of solvent added. When the pore volume of the support is determined, the active metal precursor is prepared as an aqueous or organic solution with the wanted loading of the active metal, before it is added to the support material. The adsorption of the active metal precursor into the pores of the support from the aqueous solution is controlled by capillary action.^[33]

When the active precursor is applied by adsorption onto the surface of the support, the loading that can be achieved is small. This is correlated with the low solubility of metal salts in suitable solutions and low pore volumes for the supports.^[63] Small metal loadings are typical for catalysts that consist of precious metals, and since there is no loss of active metal associated with IWI, it is usually the preferred method employed for these types of catalysts.

2.2.2 Drying

After the impregnation, the mixture is dried to remove the solvent and to crystallize the salt on the surface of the pores. The rate of drying highly influences the distribution of salt on the surface, meaning that a too low drying rate will primarily deposit the salt at the bottom of the pores, while a too high rate of drying will primarily deposit the salt around the external surface of the pores.^[64] Hence, to obtain a homogeneous distribution of the salt in the pores, the rate of drying ought to be optimized somewhere in the middle of the two extremes.

2.2.3 Calcination

After synthesis, a heterogeneous catalyst is calcined to redissolve the metal salts and to convert these into metals or metal oxides.^[64] This step includes heat treatment at ambient pressure in a given atmosphere, typically air or nitrogen.

2.3 Catalyst Characterization

2.3.1 X-Ray Diffraction

X-ray diffraction (XRD) is a characterization method used to identify the crystalline phases present in a material and can also be used to indicate the particle size.^[12] Figure 2.7 shows a schematic illustration of the diffraction of X-rays in a crystalline sample. Here, monochromatic X-rays are radiated onto the sample, where they are elastically scattered by atoms in a periodic lattice. This interaction gives rise to constructive interference between the reflected rays and the sample, and by measuring the angle (2θ) of which the rays escape the crystal, the lattice spacing can be obtained by Bragg's law:

$$n\lambda = 2d \sin(\theta) \quad (2.3)$$

where n is an integer and represents the order of reflection, λ is the wavelength of the X-rays, d is the distance between two lattice planes and θ is the angle between the incoming rays and the normal to the reflecting lattice plane.

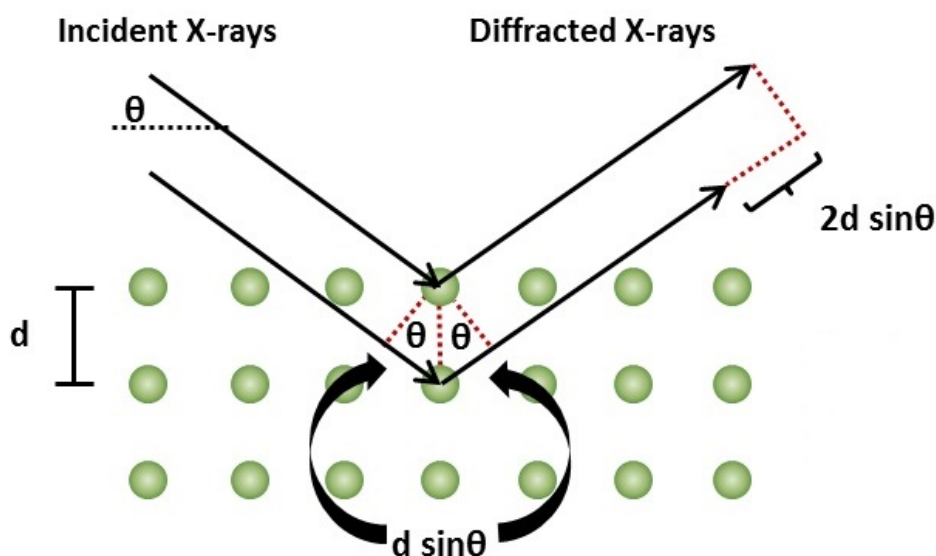


Figure 2.7: Schematic illustration of the Bragg equation, from Anton Paar^[65]. The incident X-rays are diffracted by constructive interference with the atoms in the lattice, and the direction of the diffracted X-rays may be calculated by the Bragg equation.

The X-ray diffraction patterns are measured with a stationary X-ray source and a mobile detector, where the X-rays typically have $\text{CuK}\alpha$ energy. The detector monitors the intensity of the diffracted rays with respect to the 2θ angle between the incident and the diffracted X-rays. Since every crystalline mineral have unique lattice spacings, the given mineral can be identified by collecting and analyzing the diffraction peaks and comparing to standard reference patterns.^[12]

XRD can also be used to estimate the mean crystallite size in a sample, which is performed by line broadening analysis of the XRD pattern. One possible method is by using the

Scherrer equation, which relates the crystallite size to the breadth of the diffraction line as shown in Equation 2.4.

$$L_{hkl} = \frac{k\lambda}{\beta \cos \theta} \quad (2.4)$$

Here L_{hkl} is the thickness of the crystallite, k is a constant, λ is the wavelength of the X-rays employed (for $\text{CuK}\alpha$ radiation the wavelength is 1.5406 \AA), β is the peak width, and θ the angle between the beam and the normal to the reflecting plane. In this equation the crystallite size is inversely proportional to the breadth of the diffraction line, β , which commonly is determined as the *full width at half-maximum intensity* (FWHM) of the peak.^[33] It is, however, important to note that the crystallite size obtained from the Scherrer equation is not always precise and only serves as an approximation.

2.3.2 H_2 Chemisorption

H_2 chemisorption is a method used to determine the dispersion of metal atoms on a catalyst surface. Dispersion is a measure of the number of surface atoms in the metal relative to the total number of metal atoms in the catalyst^[66], and can be calculated by the relation in Equation 2.5.

$$D = \frac{v_{\text{ads}} M_{\text{m}} F}{x_{\text{m}}} \quad (2.5)$$

where v_{ads} is the volume of H_2 that is adsorbed, M_{m} is the atomic mass of the metal, F is the number of surface atoms covered by one adsorbed H_2 molecule, and x_{m} is the weight fraction of metal in the catalyst.

Hydrogen gas generally adsorbs dissociatively onto active sites, i.e. $F = 2$, as illustrated in Equation 2.6.



where M_s represents a surface metal atom.

By measuring the adsorbed amount of H_2 as the H_2 pressure is increased, a Langmuir type isotherm is obtained. Extrapolating the linear part of the adsorption curve back to the origin pressure, as shown in Figure 2.8, the volume adsorbed, V , is found and is further used in the calculation of v_{ads} , from $v_{\text{ads}} = V/V_{\text{m}}$, where V_{m} is the volume of one mole of ideal gas at ambient conditions.

Although the Langmuir isotherm is widely used as a model for the adsorption of gas onto surfaces, it has several inherent limitations. One of the major assumptions made in the derivation of the Langmuir isotherm is that the surface is homogeneous, whereas all real surfaces are heterogeneous.^[12] Nor does the Langmuir model account for any interactions between neighboring atoms adsorbed on the surface.

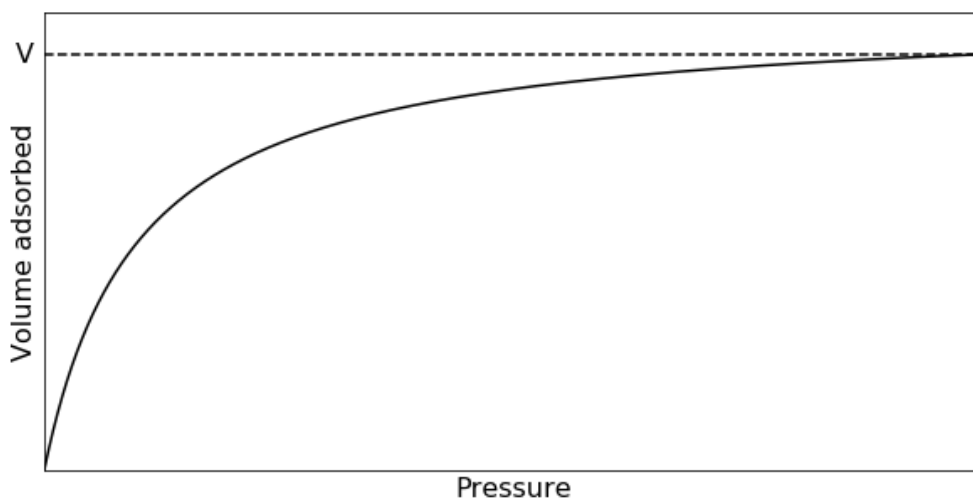


Figure 2.8: Typical shape of a Langmuir type isotherm.

A common challenge regarding chemisorption is that the curve does not turn linear at high pressures, which makes it difficult to extrapolate back to the origin. In this case, the curve is fitted to a Langmuir isotherm to obtain the adsorbed volume. In addition, there is a challenge regarding *total adsorption*, the process in which both chemisorption and physisorption occurs, i.e. not only chemisorption.^[12] This is dealt with by evacuating the sample between two adsorption stages and taking the difference of the two obtained isotherms. The difference between the two isotherms is then a measure of the amount of gas that is strongly interacting with the surface, and thus solely represents chemisorbed species.

2.3.3 N₂ Physisorption

N₂-physisorption experiments are used to determine a range of physical properties of catalysts. Amongst those are average pore size and pore size distribution, pore volume, and the BET surface area. The experiments are performed at 77 K – at the boiling point of liquid nitrogen, and the uptake of nitrogen, i.e. the amount of nitrogen that is physisorbed onto the catalyst, is measured as a function of the nitrogen pressure.^[12]

The Brunauer-Emmet-Teller (BET) isotherm is shown in Equation 2.7, and the isotherm describes the volume of gas adsorbed by the catalyst material.

$$\frac{p}{V(p_0 - p)} = \frac{1}{V_m c} + \frac{c - 1}{V_m c} \frac{p}{p_0} \quad (2.7)$$

p is the gas pressure, p_0 is the saturated vapor pressure of the liquid at the operating temperature, V is the volume of the adsorbed gas, V_m is the volume equivalent to an adsorbed monolayer, and c is a constant.

By plotting $p/[V(p_0 - p)]$ versus p/p_0 a straight line is obtained. The constant, c , and the monolayer coverage, V_m , in Equation 2.7 can then be determined as the intercept and the slope of the line, respectively. The physisorption isotherm is transformed into a BET plot, which allows the derivation of the BET monolayer capacity. Using the additional information that the average area occupied by one adsorbed N_2 molecule is 0.162 nm^2 , the total BET surface area can be calculated from the monolayer coverage. Figure 2.9 illustrates the relationship between the monolayer and the linear region of the adsorption isotherm.

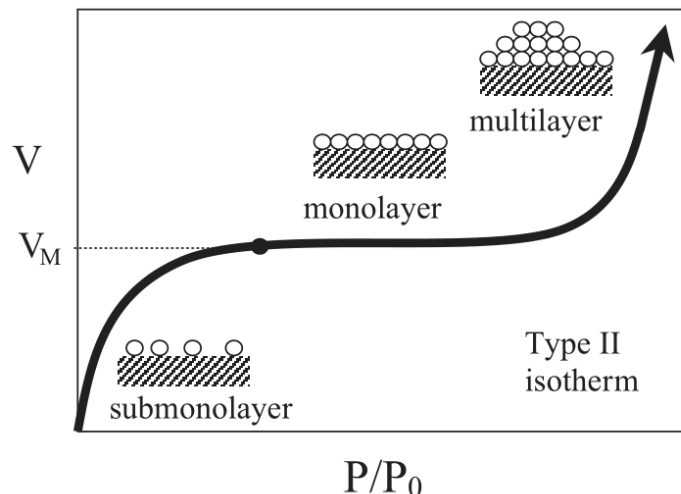


Figure 2.9: Schematic illustration of the relation between the adsorption isotherm and the coverage.^[12]

The BET isotherm is a continuation of the Langmuir isotherm. The Langmuir isotherm only accounts for monolayer coverage on the surface, whilst the BET isotherm gives a model that also accounts for multilayer coverages. Consequently, there are several similarities between the Langmuir isotherm and the BET isotherm, and the following assumptions are made for the latter:^[12]

- Dynamic equilibrium between each layer and the gas phase, i.e. the rate of adsorption and desorption in all layers are equal.
- The molecules adsorb on equivalent sites in the first layer.
- There is a dynamic balance where the already adsorbed molecules constitute the adsorption of the molecules in higher layers.
- The adsorption energy for molecules in the second and the subsequent layers equals the condensation energy.
- Any adsorbate-adsorbate interactions are neglected.
- The conditions for adsorption and desorption are equal for all layers but the first.
- For the first layer, the heat of adsorption is constant.
- The multilayer thickness is infinite at saturation pressure.

When the volume of gas adsorbed is known, the BET surface area may be derived based on the relation in Equation 2.8.

$$S_{\text{BET}} = \frac{n_m N_A \sigma_{\text{N}_2}}{m} \quad (2.8)$$

where n_m is the number of moles of gas in the monolayer, N_A is Avogadro's number, σ_{N_2} is the cross-sectional area of one adsorbed nitrogen molecule and m is the sample mass.

The desorption isotherm is a result of capillary condensation in the pores, and is described by the Kelvin equation:

$$\ln \left(\frac{p}{p_0} \right) = - \frac{2\sigma V_m \cos \theta}{rRT} \quad (2.9)$$

where p is the measured pressure, p_0 is the saturation pressure, σ is the surface tension of liquid nitrogen, θ is the contact angle, V_m is the molar volume of liquid nitrogen, r is the radius of the pore, R is the gas constant and T is the temperature.

A modified version of the Kelvin equation is used in the Barret-Joyner-Halenda (BJH) method for determining the pore size distribution in a sample.^[67] In these experiments, usually applied on mesoporous materials, the relative pressure, p/p^0 , is decreased from a high to a low value while the amount of adsorbate removed from the pores is measured. This is further related to the size of the pores via the modified Kelvin equation.^[68]

2.3.4 Temperature-Programmed Reduction

Temperature-programmed reduction (TPR) is a method based on monitoring a chemical reduction reaction while undergoing a linear increase in temperature.^[12] This method gives valuable information on the reduction temperature for a certain sample, whether the sample is fully reduced in single or multiple steps, effect of promoter, degree of reduction, etc.. The procedure involves flowing diluted hydrogen gas (typically in argon or nitrogen gas) through a reactor containing the sample, while the temperature is linearly increased. The off-gas from the reduction reaction is analyzed by mass spectrometry or using a thermal conductivity detector to quantify the amount of hydrogen that is reacted, i.e. the degree of reduction.

In general, reduction of metal oxides follows the reaction shown in Equation 2.10.^[33]



2.4 Catalyst Performance

The performance of a catalyst is typically discussed in terms of activity, selectivity, and stability (i.e. deactivation). These terms are presented in the following.

2.4.1 Activity

The activity of a catalyst can be reported in a variety of ways. Typical measures in heterogeneous catalysis are site time yield (STY) and turnover frequency (TOF), although there are a number of other measures used, often specific to a certain catalyst or process. The latter measures are typically given as reaction rates or conversion per unit mass of catalyst or similar and are only valid for a specific set of experimental conditions. This adds to inconsistency in reporting and difficulties of reproducing other work.^[69] In this paper, the activity measurements will be presented in terms of site time yield (STY) and CO conversion.

One definition of the site time yield is

“the number of molecules of a specified product made per catalytic site and per unit time.”^[69]

To calculate the site time yield it is necessary to know the number of cobalt atoms that are exposed on the catalytic surface, which may be estimated by, for instance, H₂ chemisorption or XRD. STY is calculated from the relation in Equation 2.11.

Site time yield

$$\text{STY [1/s]} = \frac{r_A M_m}{w_m D} \quad (2.11)$$

M_m is the molecular mass of the active metal, w_m is the weight fraction of the active metal, D is the dispersion of the active metal on the catalyst surface, and r_A is the rate of reaction based on the key component A, which can be calculated using Equation 2.12.

Reaction rate

$$r_A [\text{mL/g}_{\text{cat}}/\text{s}] = \frac{X_A F_{A,0}}{m_{\text{cat.}}} \quad (2.12)$$

$F_{A,0}$ is the flow of component A in the feed, $m_{\text{cat.}}$ is the total mass of catalyst, and X_A is the conversion of key component A, which is determined by Equation 2.13.

Conversion

$$X_A [-] = 1 - \frac{F_A}{F_{A,0}} \quad (2.13)$$

F_A is the flow of key component A in the product stream, and $F_{A,0}$ is the flow of key component A in the feed.

2.4.2 Selectivity

Selectivity is a measure of how selectively a certain compound is formed in a reaction. One definition is that it is the *total amount of the desired product formed per total amount of reactant consumed*.^[70]

Using the definition of selectivity presented above, the selectivity for formation of component B can be calculated using Equation 2.14.

Selectivity

$$S_B = \frac{F_B}{F_{A,0}X_A} \quad (2.14)$$

where F_B is the flow rate of component B in the product stream, $F_{A,0}$ is the flow rate of component A in the feed, and X_A is the conversion of key component A. F_B can be determined by experimental data obtained from gas chromatography or similar.

2.4.3 Stability

During the course of a reaction the catalyst involved suffers from chemical, thermal and mechanical stress of various kinds that affects its overall performance.^[12] The robustness that a catalyst displays towards these circumstances therefore highly determines its life-time. Figure 2.10 illustrates the typical activity trend of a catalytic reaction. As shown, the activity starts off high in the initial stage but decreases rapidly. This is followed by a long-lasting phase of steady descending activity, with a subsequent stage where the activity decreases rapidly.

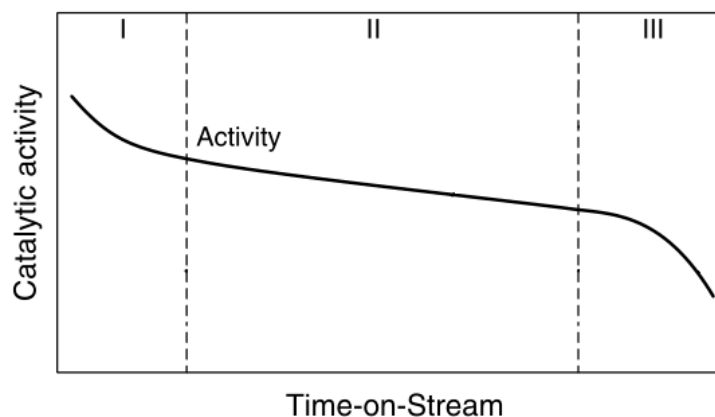


Figure 2.10: Typical activity trend for a catalytic process. Figure adapted from Ertl, G.^[33]

The main explanations for the loss of activity during a catalytic process are related to deactivation mechanisms, such as^[33]

Poisoning

Strong chemisorption of species (typical impurities in the feed) on catalytic sites with subsequent blocking of the sites for the catalytic reaction. The types of deactivating species are usually unique for the various catalysts.

Fouling/Coking

Deposition of carbonaceous material onto the catalytic surface and in catalytic pores.

Sintering

Thermally-induced loss of catalytic surface area, support area, and active phase-support reactions.

Chemical reactions

Chemical reaction of fluid, support, or promoter with catalytic phase to produce inactive phase.

Phase transformations

Reaction of gas with the catalyst phase to produce volatile compounds.

Attrition/Crushing

Loss of catalytic material due to abrasion/loss of internal surface area due to mechanically induced crushing of catalyst.

The deactivation mechanisms are often interdependent, meaning that the effects of one deactivation mechanism may assist other mechanisms. Examples of this include the adsorption of poison onto the metallic active sites that lead to the metallic clusters becoming more mobile, causing sintering, and the effect of by-product water which facilitates re-oxidation and sintering.^[33]

2.5 Gas Chromatography

Gas chromatography is a method that is used to separate compounds in a sample into individual components, with subsequent quantitative analysis of the given sample. The separation of components is carried out using a mobile phase and a stationary phase. The mobile phase is typically inert or unreactive species (helium or nitrogen) that acts as the carrier gas, while the stationary phase, although highly dependent on the nature of the analyte, is typically a packed or capillary column. The carrier gas transports the sample through the column, where the physical properties associated with both the individual components in the sample (volatility and polarity) and the stationary phase itself (temperature and composition) determines at what rate the various components move through the column.^[33] Hence, at the outlet of the column, the components exit in order of their relative volatility and polarity to the stationary phase at the given temperature.

A simplified diagram of a gas chromatograph is shown in Figure 2.11.

A typical setup for detection of light hydrocarbons is to use a packed column as the stationary phase for separation of components before detection with a *thermal conductivity detector* (TCD) and a capillary column to separate components for detection with a *flame ionization detector* (FID).^[72] The most important property of the stationary phase is that it has a similar (ideally identical) polarity as the analyte. This will both enhance the separation of the compounds, as well as require less time to perform the separation. For analyzing mixtures of both organic and inorganic components, both types of detectors are usually used. This is due to their respective sensitivities to the different components;

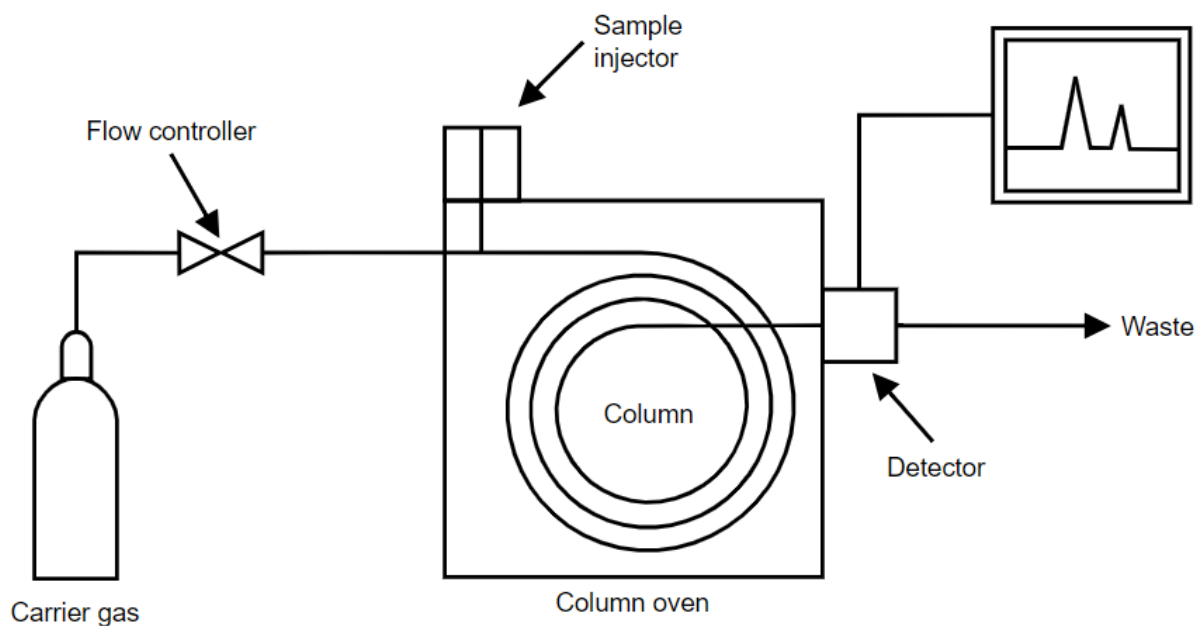


Figure 2.11: Gas chromatograph. The injected sample is carried into the oven heated column by the carrier gas. In the column, the components of the sample are separated such that they enter the detector according to their respective retention times. The detector measures a change in thermal conductivity (TCD) or change in electrode current (FID) and produces a peak in a chromatogram. Figure adapted from Wikipedia.^[71]

a TCD has a high sensitivity to compounds like nitrogen, oxygen, carbon monoxide, sulfuric species, and inorganic gases, but has limited sensitivity to organic species like hydrocarbons, whereas the opposite is true for the FID. Thus, the combination of the two gives a detection system that can detect a wide range of species with high sensitivity and accuracy.

The TCD continuously detects the thermal conductivity of the effluent gas and compares it to that of a reference flow of carrier gas. The reference flow is commonly either helium or hydrogen, which has a much higher thermal conductivity than most other compounds. Hence, when a compound different from the carrier gas is introduced to the detector, a detectable drop in thermal conductivity is induced, producing a signal. The FID is usually fitted directly above the outlet of the capillary column, where the exit gas is led through a combustion chamber powered by a hydrogen flame, which ionizes the column effluent. The charged particles produced from the ionization creates a detectable increase in current between the two electrodes that are associated with the FID. The change in current is translated into a peak in a chromatogram, whereas the area of the peak corresponds to the concentration of the species in the sample.^[72]

Experimental

3.1 Catalyst Preparation

For the synthesis of the 20 %Co0.5 %Re/ γ -Al₂O₃ catalyst, the γ -Al₂O₃ support was first placed in a ventilated heating cabinet at 110 °C for 3 hours. This was followed by the determination of the incipient wetness point (IWP) by adding de-ionized water in a dropwise manner to the support. The pore volume of the support was further calculated as the ratio of the mass of de-ionized water added and the mass of support. The amount of water required to obtain a saturated catalyst mixture was then determined based on the pore volume of the support.

The precursor solution containing cobalt precursor (cobalt nitrate hexahydrate), rhenium precursor (perrhenic acid) and de-ionized water was prepared based on the desired metal and promoter content in the final catalyst, and the solution was mixed thoroughly to ensure homogeneity. The solution was then added drop-by-drop to the support to reach the IWP. The catalyst mixture was placed in a heating cabinet at 110 °C to dry for one hour and fifteen minutes, with stirring every fifteen minutes, to evaporate the liquids.

Furthermore, the catalyst was calcined using a fixed bed quartz reactor at 300 K for 16 hours, with a constant airflow of 0.7 mL/min flowing through it. The temperature ramp was set to 2 °C/min from ambient temperature to 300 K. Lastly, the catalyst was sieved to 53-90 μ m.

The detailed calculations can be found in Appendix A.1.

The commercial type catalyst was a 20 %Co0.5 %Re/ γ -Al₂O₃ procured from Equinor and was used “as is”.

3.2 Catalyst Characterization

3.2.1 X-ray Diffraction

The X-ray diffractograms were obtained using a Bruker D8 DaVinci-1 X-ray Diffractometer with $\text{CuK}\alpha$ radiation. The catalyst sample was placed onto a sample holder before the surface of the sample was smoothed with a glass plate. The sample holder was then placed into a queue rack. The apparatus engineer then inserted the sample into the apparatus for analysis. The analysis was performed over a time frame of 60 minutes, with a 2θ angle range from 15 to 75 degrees and a fixed slit opening of 0.3 degrees. The measurements were executed on oxide catalysts.

The measurements were executed on calcined catalysts, and the average particle size of Co_3O_4 was calculated from the most intense peak in the diffractograms. For estimations of the average particle size, it was assumed spherical particles and the estimates were corrected with a factor of $4/3$ ^[73]. The particle size of the oxides was converted to metallic particle size using the relative molar volumes,^[74] and the conversion factor is shown in Equation 3.1.

$$d_p(\text{Co}^0) = 0.75d_p(\text{Co}_3\text{O}_4) \quad (3.1)$$

The cobalt particle size is related to the dispersion through the formula given below:^[12]

$$D = \frac{f \cdot M_M}{\rho \cdot \sigma \cdot N_A} \times \frac{S}{V} \quad (3.2)$$

where the particle size is included in the ratio between the surface area, S , and the volume, V . Assuming spherical particles gives $S/V = 6/d_p$, where d_p is the particle diameter. f is the fraction of the surface of the active atom which is effectively exposed to the reactants, M_M is the atomic weight, ρ is the specific mass of the active phase, σ is the average surface area occupied by one active atom on the surface, and N_A is Avogadro's number.

Assuming uniform cobalt particles with site density of 14.6 atoms/nm^2 and spherical particles^[75] gives the following simple relation between the particle diameter and dispersion.

$$D = \frac{96}{d_p} \quad (3.3)$$

where D is the dispersion in percent and d_p is the particle diameter in nm.

3.2.2 H_2 Chemisorption

The H_2 chemisorption experiments were performed using a Micrometrics ASAP 2020 instrument. A piece of glass wool was placed inside a U-tube quartz reactor. Approximately 200 mg of the catalyst was poured into the reactor, and the catalyst sample was isolated by adding another piece of glass wool into the reactor. The reactor was then weighed

before mounting onto the instrument. The furnace associated with the instrument was then raised, isolating the reactor. First, the catalyst was reduced *in situ* at a temperature of 350 °C at a ramp rate of 1.0 °C/min, with a constant flow of H₂ continuously flowing through the reactor. These conditions were kept for a total time of 600 minutes. The reactor was then evacuated and the temperature lowered to 40 °C, the temperature in which the chemisorption took place with a constant flow of H₂. When the analysis was finished, the reactor was dismantled and weighed.

3.2.3 N₂ Physisorption

The N₂ physisorption experiments were performed using a Micromeritics II 3021 Surface Area and Porosity Analyzer. An empty sample tube was first weighed on a microscale before the sample was placed inside it (approximately 120 mg). The tube was then placed in the cooling slot of a VacPrep 061 degassing station for one hour under vacuum, before being moved to the heating slot heated to 200 °C for at least 12 hours. After degassing, the tube was weighed once more to obtain the total sample mass of the degassed sample, and a filling rod and an isothermal jacket were attached to the tube before it was mounted to the apparatus. The cryogenic storage dewar for containing the liquid nitrogen was filled to the mark and placed on the elevator beneath the mounted sample tubes, and then the analysis was started. When finished, the sample tube was dismantled from the apparatus and weighed one final time.

The physisorption isotherm was used to calculate the BET surface area, and the BJH method based on the desorption isotherm was used to determine the pore-size distribution and pore volume.

3.2.4 Temperature-Programmed Reduction

The temperature-programmed reduction was performed using a Altamira BenchCat Hydrid apparatus. A small piece of quartz wool was placed into a quartz U-tube reactor. Approximately 150 mg of the catalyst was then poured into the tube, before isolating the catalyst sample with another small piece of quartz wool. The reactor was then mounted to the Altamira apparatus and the TPR was performed. The reduction was performed at ambient pressure, with a temperature range from ambient to 900 °C and using a blend gas containing 7 % H₂ in Ar.

3.3 Fischer-Tropsch Synthesis

3.3.1 Apparatus

The Fischer-Tropsch synthesis experiments were executed in a stainless steel fixed-bed reactor with ID 10 mm. A movable thermocouple was inserted into the bed for temperature measurements, and the reactor was enclosed in both an aluminum jacket and an insulation compartment to improve isothermal conditions. An electrical furnace was used

as a heating source. A simplified Piping and Instrumentation Diagram (P&ID) of the rig is attached at the end of this chapter.

The source of syngas was a 50 L gas cylinder with 3% N₂ and 48.5% CO in H₂. The syngas was diluted in H₂ from an external 50 L gas cylinder containing pure H₂ to give the desired H₂/CO ratios. All gas cylinders that was used in these experiments was procured from AGA.

The flow rate of all the gases and the liquid water was controlled using Bronckhorst flow controllers; mass flow controllers (MFC) for the gases and liquid flow controllers (LFC) for the liquid water. The flow of liquid water was led through an evaporator at 350 °C before it was mixed with syngas just prior to the reactor inlet. A sample calculation of the conversion from wanted gas pressure of water to liquid flow rate is shown in Appendix A.2.

The gaseous products were analyzed online by an Agilent 6890N gas chromatograph, containing both a thermal conductivity detector (TCD) and a flame ionization detector (FID). The samples was analyzed with fixed intervals and was analyzed for H₂, N₂, CO, CO₂ and C₁-C₄ hydrocarbons.

3.3.2 Procedure

The catalyst was diluted in inert SiC with particle size in the range 53 μm to 90 μm to give a total mass of the catalyst bed of 20 g. This was done to minimize temperature gradients along the catalyst bed. A hollow stainless steel rod was placed at the bottom of the reactor and pieces of quartz-wool were placed both above and below the bed to keep the catalyst bed in place.

The catalyst reduction was performed *in-situ* using a constant flow of 250 mL/min hydrogen gas at ambient pressure. The temperature was first increased from ambient to 350 °C with a ramp rate of 1.0 °C/min, where it was held constant for 10 h, followed by a decrease to 170 °C. A Eurotherm was used to program the temperature profile for the reduction. After reduction, the reactor system was purged with helium and simultaneously pressurized to 20 bar, using a constant flow of 250 mL/min. When the desired pressure was reached, the helium flow was replaced with a syngas flow of equal magnitude, and the temperature in the reactor was increased to the appropriate temperatures. For reaching the various temperature levels the temperature programs were:

Reaching 210 °C

- 20 °C/h from 170 °C to 190 °C
- 5 °C/h from 190 °C to 209 °C
- Manual adjustment to 210 °C

Reaching 220 °C

- 30 °C/h from 170 °C to 200 °C
- 5 °C/h from 200 °C to 219 °C

- Manual adjustment to 220 °C

Reaching 230 °C

- 40 °C/h from 170 °C to 210 °C
- 5 °C/h from 210 °C to 229 °C
- Manual adjustment to 230 °C

The slow increase in temperature was done to prevent any run-away reactions.

All the experiments followed the experimental series of steps shown below:

1. Initial conditions: 250 mL/min syngas.
2. Reduce the flow rate of syngas to obtain 50 % conversion.
3. Reduce the flow rate of syngas to obtain 70 % conversion.
4. Adjust back to initial conditions.
5. Keep the initial conditions, increase the total pressure in the reactor to 22 bar and add to that a flow of water corresponding to 2 bar.
6. Adjust flow rate of syngas to obtain 50 % conversion, and water correspondingly to keep 2 bar water in the feed.
7. Adjust back to initial conditions, decrease the total pressure to 20 bar and stop the water supply.

The flow rates of syngas necessary to obtain the wanted conversions of 50 % and 70 % were determined using the relation shown in Equation 3.4.

$$F_{\text{old}}X_{\text{old}} = F_{\text{new}}X_{\text{new}} \quad (3.4)$$

where F_{old} is the current flow rate, X_{old} is the steady-state conversion obtained at the current flow rate, X_{new} is the desired conversion and F_{new} is the necessary flow rate to obtain the desired conversion.

Catalyst regeneration was performed after two of the experiments using two different regeneration procedures:

Low pressure regeneration (LPR)

- The syngas flow was replaced by a flow of helium of approximately 400 mL/min.
- The pressure was decreased from operating pressure to atmospheric.
- Temperature was decreased to 170 °C
- After 24 h of purging catalyst reduction was initiated, following the same procedure as described above.

Operating conditions regeneration (OCR)

- The syngas flow was replaced by a flow of helium of approximately 250 mL/min.
- Purging with helium at operating conditions (20 bar and 210 °C/230 °C).
- After 24 h of purging catalyst reduction was initiated, following the same procedure as described above.

The various reaction conditions are listed in Table 3.1.

Table 3.1: Reaction conditions for the various experiments. (*) represents the experiments after catalyst regeneration.

Exp.	Catalyst	m _{cat.} [g]	T [°C]	P _{tot} ^a [bar]	P _{syngas} ^b [bar]	P _{water} ^c [bar]	H ₂ /CO(feed)
1	Standard	1.0	210	20 (22)	20	2	2.12
1	Commercial type	0.5	220	20 (22)	20	2	2.12
2	Commercial type	1.0	210	20 (22)	20	2	2.13, 1.75, 1.44
2	Commercial type	0.3	230	20 (22)	20	2	2.13, 1.75, 1.44
3	Commercial type	4.0	210	20 (22)	20	2	1.12
3	Commercial type	1.5	230	20 (22)	20	2	1.12
4	Commercial type	1.5	210	20 (22)	20	2	1.72
4	Commercial type	0.6	230	20 (22)	20	2	1.72
5	Commercial type	1.85	210	20 (22)	20	2	1.41
5	Commercial type	0.5	230	20 (22)	20	2	1.41
5* ^d	Commercial type	1.85	210	20	20	-	1.41
5* ^d	Commercial type	0.5	230	20	20	-	1.41
6	Commercial type	0.9	210	20 (22)	20	2	2.55
6	Commercial type	0.35	230	20 (22)	20	2	2.55
6* ^d	Commercial type	0.9	210	20	20	-	2.55
6* ^d	Commercial type	0.35	230	20	20	-	2.55

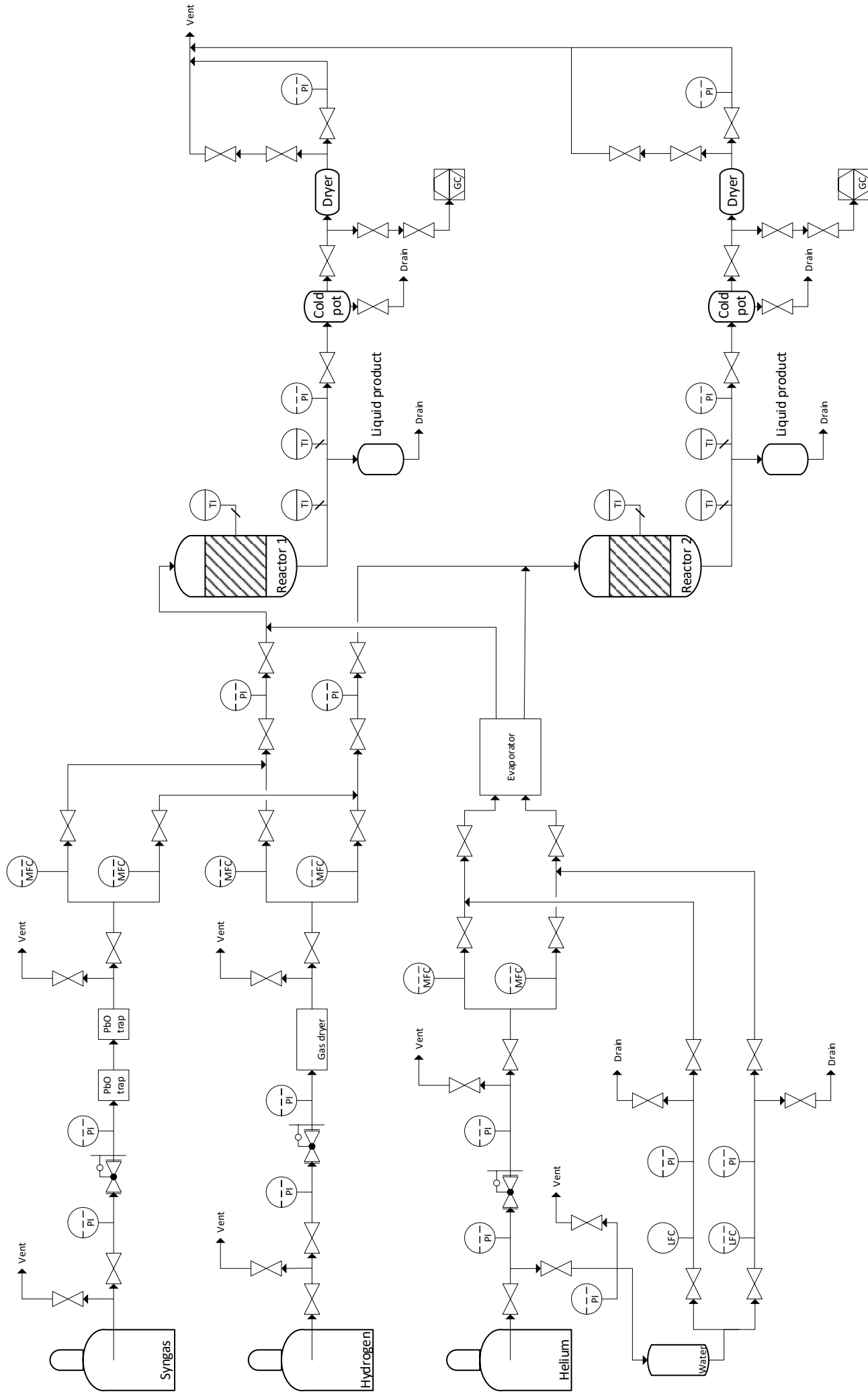
^a Total pressure in the reactor at dry conditions with total pressure during wet conditions in parentheses.

^b Pressure of syngas at wet conditions.

^c Pressure of external water added at wet conditions.

^d After regeneration. Only steps 1 and 2 of the experimental procedure were executed in these experiments.

Simplified P&ID of SINTEF Fischer-Tropsch rig 1.5



Results and Discussion

4.1 Catalyst Characterization

4.1.1 X-ray Diffraction & H₂ Chemisorption

The X-ray diffractograms obtained for the standard and the commercial type catalyst are shown in Figure 4.1. The location of the peaks confirms that the only crystalline phase of cobalt present was Co₃O₄. γ -alumina was also identified as the only alumina phase present. Rhenium was however not detected, probably due to the low metal loading. The XRD patterns also indicate that there are no major differences in the crystalline phases between the two catalysts.

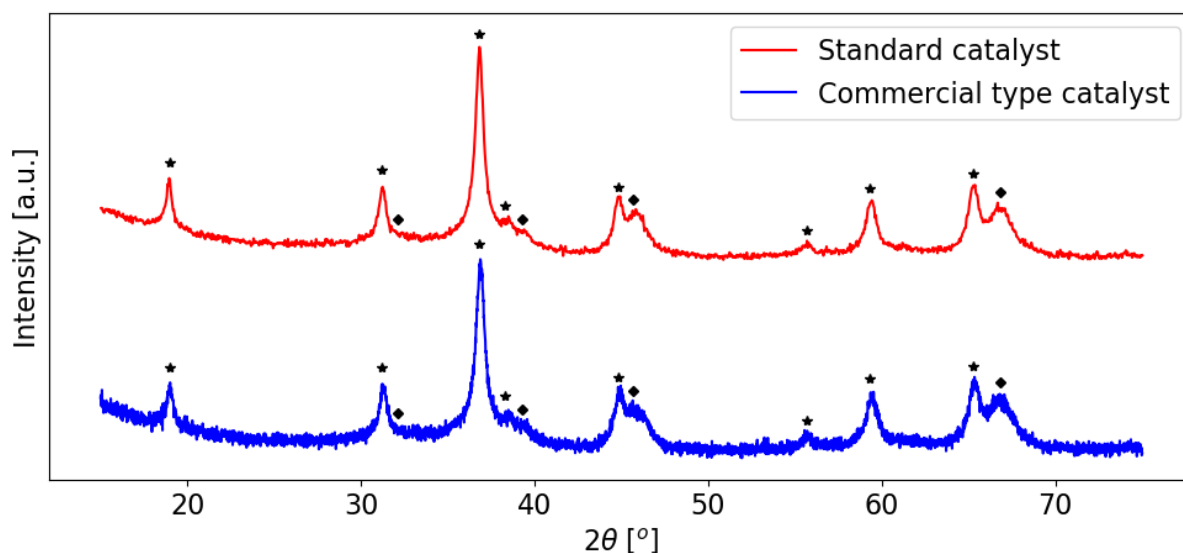


Figure 4.1: X-ray diffractogram of the commercial type and the standard catalyst. Present phases are denoted (★) Co₃O₄ and (◆) Al₂O₃. The XRD experiments were conducted during the fall of 2018.

For the estimation of Co particle size and dispersion from XRD, the width at half maximum of the peaks at 2-theta values of 59.4° were chosen. The shape of the peaks is linked to the particle size, whereas narrow peaks correspond to large particles and wide peaks correspond to small particles^[54]. Hence, the peak at 59.4° was chosen both due to the absence of interaction with other species in that region and that the shape of the peak seems to represent the average quite well. The average Co_3O_4 particle sizes were calculated using the Scherrer equation (Equation 2.4) and the average Co^0 particle sizes were estimated using Equation 3.1. Both the Co dispersion estimates from XRD analysis and the average Co^0 particle size estimates from H_2 chemisorption was determined using Equation 3.3. The dispersions and particle sizes obtained by both the two different methods are given in Table 4.1.

Table 4.1: Characterization results. Dispersion and particle size estimated from both H_2 chemisorption and X-ray diffraction. Both the XRD and the H_2 chemisorption experiments were conducted during the fall of 2018.

Catalyst	Dispersion ^a (H_2 ads.) [%]	Particle size ^b (H_2 ads.) [nm]	Dispersion ^c (XRD) [%]	Particle size ^d (XRD) [nm]
Standard	6.9	13.9	7.5	12.7
Commercial type	7.3	13.2	8.1	11.8

^a Cobalt metal dispersion from H_2 chemisorption.

^b Cobalt metal particle size from H_2 chemisorption using $d_p(\text{Co}) = 96/D$.

^c Cobalt metal dispersion from XRD using $D = 96/d_p(\text{Co})$.

^d Cobalt metal particle size from XRD using $d_p(\text{Co}) = 0.755d_p(\text{Co}_3\text{O}_4)$.

The chemisorption results are given in Table 4.1 and have been calculated based on the assumption that the adsorption stoichiometry is $\text{H}:\text{Co} = 1$ and that rhenium does not influence the amount of hydrogen chemisorbed. Evidently, the commercial type catalyst has slightly higher dispersion and slightly lower particle size, although these results are virtually identical.

Comparing the particle sizes and dispersions obtained using the two methods shows that the results are in good agreement. The slight discrepancy is probably due to the cobalt being in its reduced state during H_2 chemisorption, while XRD experiments are performed on the oxidized state, hence perfect agreement was not expected. In addition, XRD analysis is not able to detect particles smaller than 5 nm, and neither does it detect amorphous phases that may be present.^[76]

4.1.2 N₂ Physisorption

The results obtained from the N₂ physisorption experiments were the surface areas based on the BET method, and average pore sizes, pore size distributions and pore volumes based on the BJH method. The adsorption/desorption curves for the experiments are found in Appendix C.1, while the pore size distributions are shown in Figure 4.2. BET surface areas, average pore diameter and pore volumes are rendered in Table 4.2.

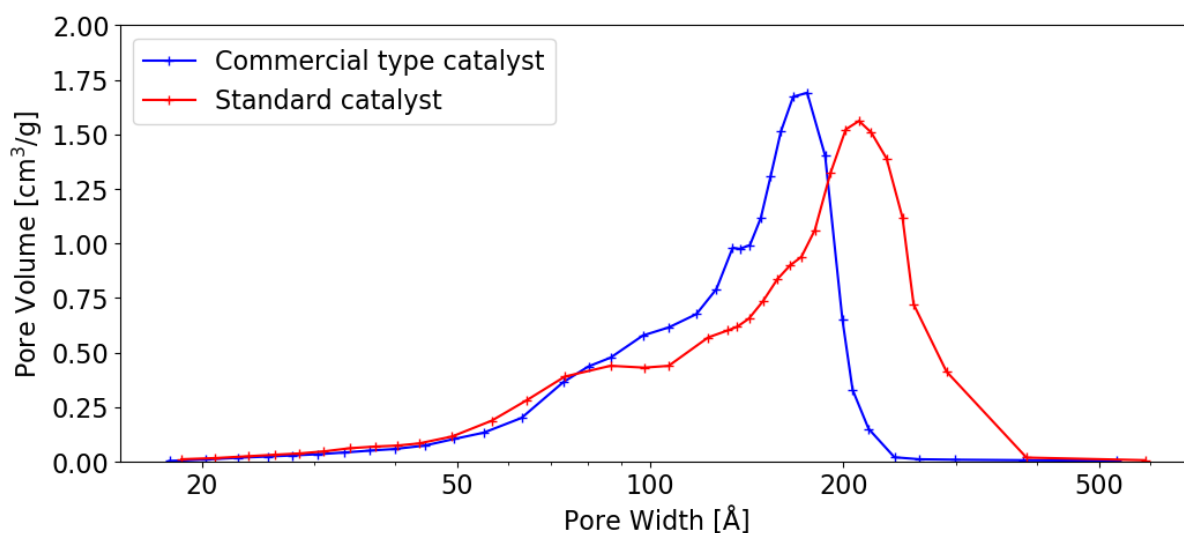


Figure 4.2: Pore size distribution of the commercial type and the standard catalyst.

The pore size distributions show that there are no major differences between the two catalysts. Both catalysts have a shoulder towards smaller pores, which is typical for γ -alumina supported catalysts.^[25] The standard catalyst displays a slightly broader distribution than that for the commercial type catalyst, and with the peak shifted slightly towards larger pores compared to the commercial type catalyst.

The BET surface area, average pore diameter, and sizes in Table 4.2 are in good agreement with the literature.^[54]

Table 4.2: Characterization results. Surface area, average pore diameter and pore volume estimated from N₂ physisorption experiments.

Catalyst	Surface area ^a [m ² /g]	Average pore diameter ^b [nm]	Pore volume ^b [cm ³ /g]
Standard	136	13.2	0.54
Commercial type	131	12.1	0.47

^a BET surface area.

^b BJH desorption.

4.1.3 Temperature-Programmed Reduction

The TPR profiles of both the standard catalyst and the commercial type catalyst are shown in Figure 4.3. The first peak visible on the TPR profile of the standard catalyst represents the reduction of residual nitrates from the catalyst synthesis.^[54] Since this peak is not visible for the commercial type catalyst, it is probable that this catalyst was treated differently, either before calcination or during calcination. The following peaks represents the reduction of Co_3O_4 to CoO and of CoO to Co^0 . The results shown here coincides well with what has been found in the literature.^[77]

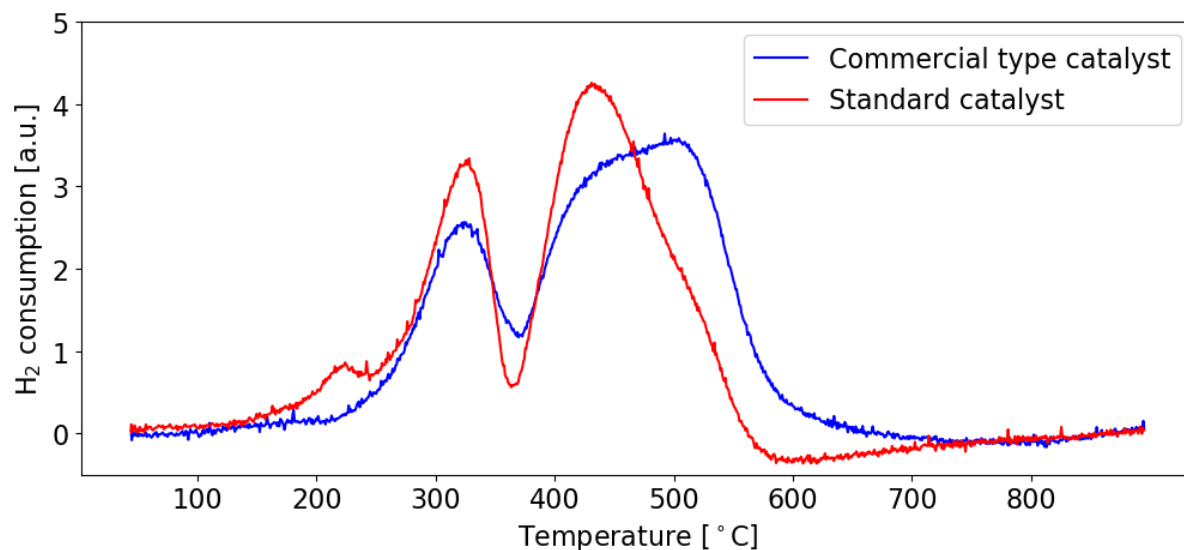


Figure 4.3: TPR profiles of the calcined catalysts. The experiments were conducted during the fall of 2018.

4.2 Fischer–Tropsch Synthesis

4.2.1 Comparison of Catalysts

One experiment were executed at equal conditions on each of the two catalysts. The conditions were $p_{\text{total}} = 20$ bar (22 bar when adding 2 bar water in the feed), $T = 210$ °C, $m_{\text{cat.}} = 1.0$ g, and $H_2/CO = 2.12$. The last five data points collected at steady-state conditions at each of the steps in the experimental procedure were averaged and used to represent the results at the given conditions. The results are presented in Figures 4.4, 4.5, and Table 4.3.

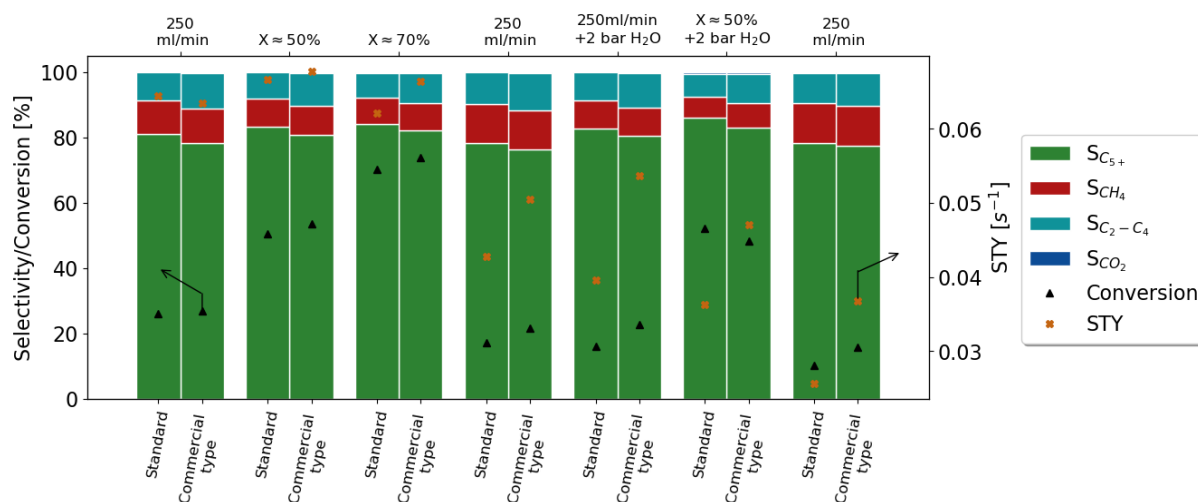


Figure 4.4: Activity and selectivity data of key components for both catalysts. The data presented are averages of the last five data points at steady-state operation for every step in the experimental procedure, which is indicated above the plot. Conditions in both instances: $p_{\text{total}} = 20$ bar with $p_{\text{total}} = 22$ bar when adding water in the feed, $T = 210$ °C, $m_{\text{cat.}} = 1.0$ g, $H_2/CO = 2.12$. CO_2 is included in the C_{5+} fraction.

As shown in Figure 4.4 the activity of the two catalysts in the initial stages are fairly similar. However, when returning to the initial flow rate in step 4, the STY for the standard catalyst dropped by 33 % compared to that of step 1, while the loss of activity associated with the commercial type catalyst was 19 % over the same time frame. The overall loss of activity during the experiments were 59 % for the standard catalyst and 41 % for the commercial type catalyst. This indicates that the commercial type catalyst is more robust to deactivation than the standard catalyst. A possible explanation may be that the two catalysts were synthesized differently. One important factor that is closely linked to the robustness of the catalyst, via both pore size and mechanical strength, is the calcination temperature. Increased calcination temperature yields larger pores and weakens the attrition robustness^[55], and since differences in the pore size distributions are observed in the pore size distributions in Figure 4.2, it is tempting to suggest a difference in calcination temperature as an explanation. However, since no information was given on how the commercial type catalyst was prepared, it is difficult to draw any conclusions.

In step five, when adding water in the feed while maintaining the initial flow rate of syngas, two opposite responses were observed. While the standard catalyst displays a

Table 4.3: Activity and selectivities of key components for both the standard catalyst (Std.) and the commercial type catalyst (Com.). The data presented are averages of the last five data points at steady-state operation at each stage of the experimental procedure. Conditions in both cases: $p_{\text{total}} = 20$ bar with $p_{\text{total}} = 22$ bar when adding water in the feed, $T = 210$ °C, $m_{\text{cat.}} = 1.0$ g, $H_2/CO = 2.12$. Experimental procedure: 1) 250 mL/min syngas, 2) adjust to 50 % conversion, 3) adjust to 70 % conversion, 4) 250 mL/min syngas, 5) 250 mL/min syngas plus 10 % water, 6) adjust to 50 % conversion with 10 % water, 7) 250 mL/min syngas.

Step #	Flow rate [mL/min]		Conversion [%]		STY [$10^2 \times 1/s$]		S(CO ₂) [%]		S(CH ₄) [%]		S(C ₅₊) ^a [%]	
	Std. ^b	Com. ^c	Std.	Com.	Std.	Com.	Std.	Com.	Std.	Com.	Std.	Com.
1	250.0	250.0	25.9	27.0	6.4	6.3	>0.01	0.16	10.1	10.4	81.2	78.6
2	133.0	134.0	50.4	53.7	6.7	6.8	0.07	0.17	8.7	9.0	83.4	80.9
3	84.2	95.6	70.2	73.9	6.2	6.6	0.14	0.26	8.0	8.3	84.4	82.4
4	250.0	250.0	17.2	21.5	4.3	5.1	>0.01	0.21	11.7	11.9	78.5	76.6
5 ^d	250.0	250.0	16.0	22.8	4.0	5.4	0.07	0.26	8.5	8.7	82.9	80.8
6 ^d	70.0	103.6	52.1	48.3	3.6	4.7	0.43	0.47	6.2	7.4	86.7	83.5
7	250.0	250.0	10.3	15.7	2.6	3.7	0.17	0.29	12.3	12.1	78.6	77.7

^a Reported as CO₂-free, i.e. $S(C_{5+}) = 100\% - \sum S_{\text{hydrocarbons}}$.

^b Standard catalyst.

^c Commercial type catalyst.

^d Added two bar of water vapor (10% of the syngas flow rate).

negative kinetic effect of adding water in the feed, the opposite is true for the commercial type catalyst. The variable kinetic effect of adding water in the feed observed here has also been reported by others.^{[23][24]} This has been proposed to be linked to the pore characteristics of the catalyst,^[25] whereas catalysts with broad pore size distributions have been observed to suffer strong negative kinetic effects, whilst catalysts with well-adapted pore sizes displayed positive kinetic effects. Figure 4.2 shows that the pore size distribution of the standard catalyst is quite broader than that for the commercial type catalyst, which may be a contributing factor to the observed effect. The results obtained here are, however, contradictory with that found by Borg *et al.*^[24], who observed positive kinetic effects of added water on wide-pore catalysts, while negative effects were observed on narrow-pore catalysts. This phenomenon is quite complicated and there is no consensus onto exactly which properties dictate the kinetic effect of water. The two catalysts studied here were characterized to be quite similar, however, during the experiments they were confronted with differences in conversion levels with following differences in compositions in the reaction atmosphere. In addition, the catalysts displayed differences in robustness to deactivation, which can alter both the particle and pore size of the catalysts. All of these factors may influence in what manner external water affects the kinetics, hence a conclusion is yet to be drawn.

Evidently the standard catalyst displays a higher selectivity to the C₅₊ fraction throughout the entire experiment, despite the conversion level for the commercial type catalyst being slightly higher in the majority of the stages – a factor that is well documented to have a positive impact on the C₅₊ selectivity and is discussed in Chapter 4.2.7. The higher C₅₊ selectivity of the standard catalyst may be attributed to larger pores and larger cobalt particles. It has been reported that for comparable γ -aluminas, the selectivity to

C_{5+} increases with pore diameter, pore volume, and cobalt particle size.^[57]

The selectivity to methane was observed to be slightly lower for the standard catalyst than for the commercial type catalyst, as Table 4.3 indicates. Although this deviation is within the experimental uncertainty, it is tempting to suggest that the hydrogenation capabilities of the commercial type catalyst ever so slightly exceeds that of the standard catalyst. Increased rate of hydrogenation would support heightened formation of paraffins compared to olefins, such that this suggestion may be justified by considering the olefin-to-paraffin ratios for the light products. Figure 4.5 shows these olefin-to-paraffin ratios. As shown, the olefin-to-paraffin ratio is larger for the standard catalyst throughout the entire experiment, which supports the claim that the commercial type catalyst facilitates hydrogenation better than the standard catalyst.

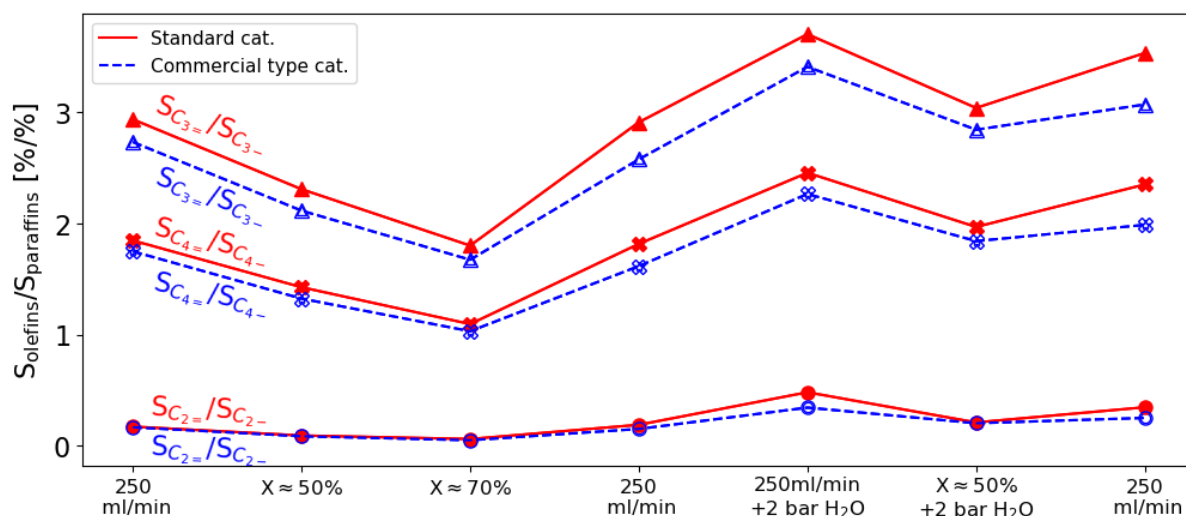


Figure 4.5: Olefin-to-paraffin ratios for both catalysts. The data presented are averages of the last five data points at steady-state operation for each step in the experimental procedure, which is indicated below the plot. Conditions in both instances: $p_{\text{total}} = 20$ bar with $p_{\text{total}} = 22$ bar when adding water in the feed, $T = 210$ °C, $m_{\text{cat.}} = 1.0$ g, $H_2/CO(\text{feed}) = 2.12$. C_{2-} = ethane; $C_{2=}$ = ethene; C_{3-} = propane; $C_{3=}$ = propene; C_{4-} = i-butane and n-butane; $C_{4=}$ = 1-butene, i-butene, cis-2-butene, and trans-2-butene.

Figure 4.6 shows the activity of both catalysts as a function of time on stream for the three stages in the experiment that were run with equal flow rates. The plots include trend lines, which actually suggest that a linear deactivation function would be sufficient to describe the activity loss during the ≈ 160 hours of experiments. Although this is an interesting result, it is highly anticipated that long-term FTS operation would give different kinds of deactivation trends, e.g. a negative exponential function. In addition, the catalysts in these experiments are subjected to quite extreme conditions, meaning that less severe deactivation is expected in conventional FTS operation.

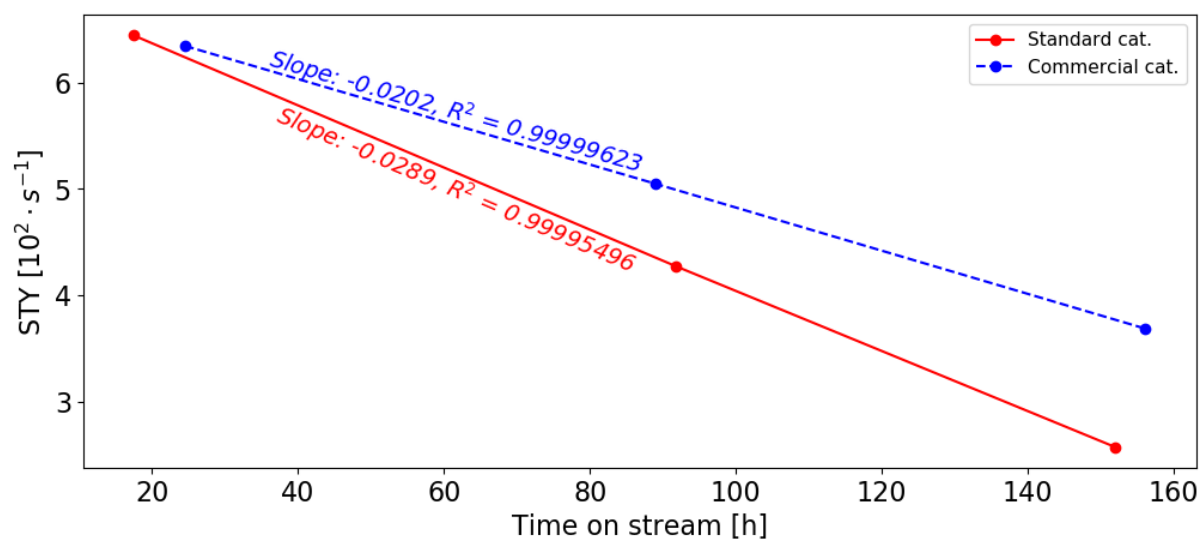


Figure 4.6: Site time yield of both catalysts at three stages of the experiments; initial, middle, and end. Syngas flow rate was 250 mL/min in all instances.

4.2.2 Effect of Temperature¹

Three experiments were conducted at equal conditions only differing in temperature, at temperature levels 210 °C, 220 °C, and 230 °C. In order to obtain comparable conversion levels, the catalyst loading corresponding to the respective temperature levels were 1.0 g, 0.5 g, and 0.3 g. In the previous chapter, it was presented that deactivation followed a linear trend in both experiments at 210 °C. This is also observed at 220 °C and 230 °C, although the trend line fit is not as good. Nonetheless, using the trend line slopes as a measure of deactivation rate, it is evident that deactivation is much more severe at the elevated temperatures. Interestingly, extracting the slopes and plotting those as a function of temperature also yields an almost linear relationship, as shown in the right-hand plot in Figure 4.7. This result suggests that all the involved deactivation mechanisms are strong functions of temperature, which is harmonious with the theory behind the proposed main deactivation mechanisms – sintering, re-oxidation, and coking – of relevance here.^[33]

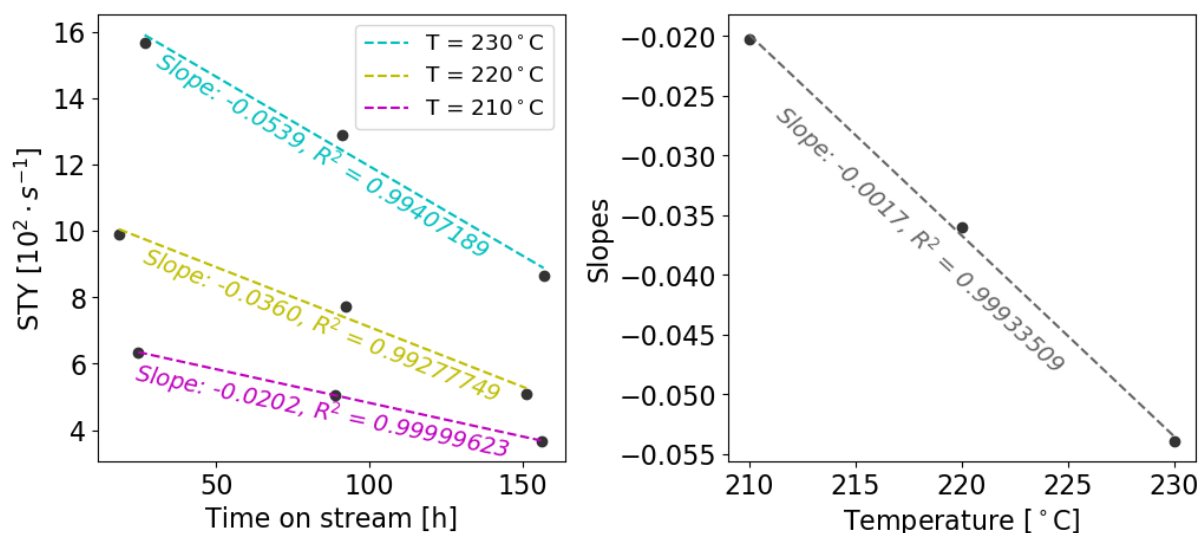


Figure 4.7: Site time yield evolution during the course of the three experiments (left) and the slopes of the trend lines as function of temperature (right). Conditions: $p_{\text{total}} = 20$ bar, $T = 210$ °C, 220 °C, and 230 °C with corresponding catalyst loading $m_{\text{cat.}} = 1.0$ g, 0.5 g, and 0.3 g, $\text{H}_2/\text{CO}(\text{feed}) = 2.12$. Syngas flow rate was 250 mL/min in all instances.

The effect of temperature on the selectivities are illustrated in Figure 4.8, where the selectivities are given at a conversion level of approximately 50 %. Clearly, the selectivities to C_{5+} and methane are highly dependent on the temperature. This is presumably due to the rate of the hydrogenation reaction of $-\text{CH}_2$ monomers (to methane), increasing faster with temperature than its competing reactions, thus lowering the surface concentration of monomers^[32], with subsequent favorable methane formation contrary to heavier products.

As Figure 4.8 shows, the selectivity to the $\text{C}_2\text{--C}_4$ fraction is virtually identical for all the temperature levels, indicating no clear correlation. This result is surprising given that the formation of light products is thermodynamically favorable at higher temperatures,^[29] and

¹The commercial type catalyst is the only catalyst undergoing further investigation. Therefore, it is implicit which catalyst is the subject in the following.

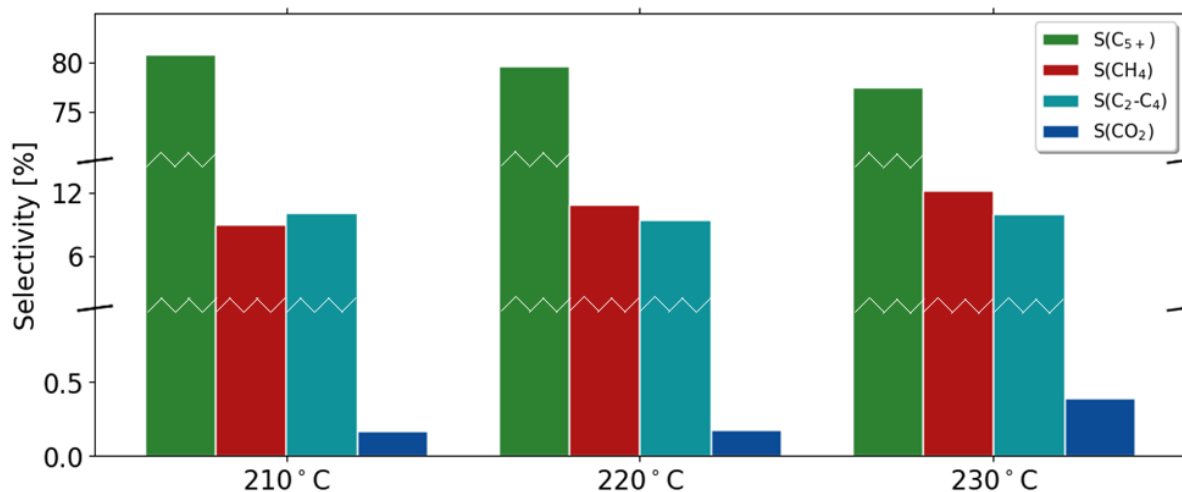


Figure 4.8: Selectivity data of key components at approximately 50% conversion at each of the three temperature levels. Conditions: $p_{\text{total}} = 20$ bar, $T = 210$ °C, 220 °C, and 230 °C with corresponding catalyst loading $m_{\text{cat.}} = 1.0$ g, 0.5 g, and 0.3 g, $\text{H}_2/\text{CO}(\text{feed}) = 2.12$.

suggests that increasing temperature mainly shifts the formation of heavier hydrocarbons towards methane instead of $\text{C}_2\text{-C}_4$ products.

Looking at the olefin-to-paraffin ratios within the topical fraction, as displayed in Figure 4.9, it is evident that there is a strong correlation in which low temperature favors high olefin-to-paraffin ratios. As discussed, the rate of hydrogenation increases disproportionately to its competing reactions with temperature, favoring the formation of more saturated products.

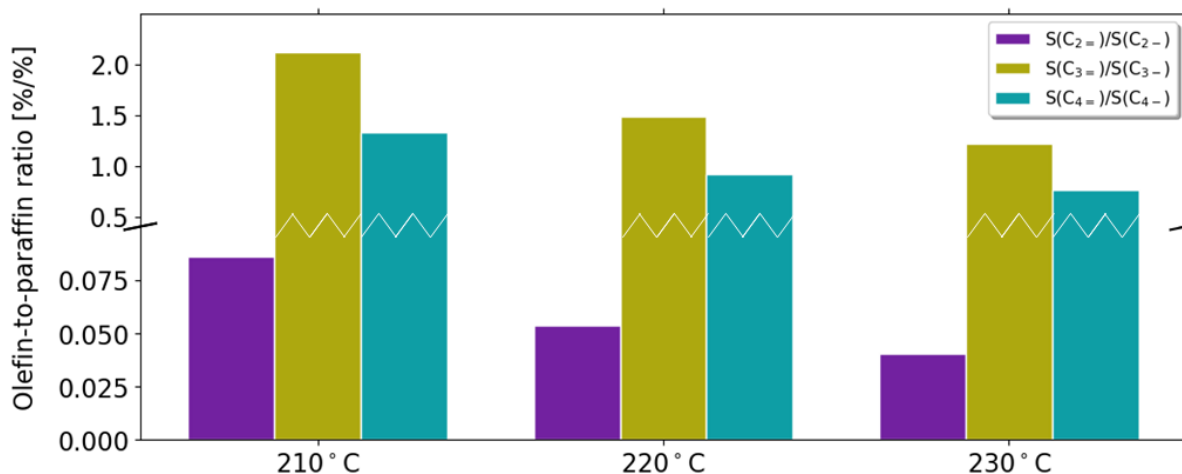


Figure 4.9: Olefin-to-paraffin ratios at approximately 50% conversion at each of the three temperature levels. Conditions: $p_{\text{total}} = 20$ bar, $T = 210$ °C, 220 °C, and 230 °C with corresponding catalyst loading $m_{\text{cat.}} = 1.0$ g, 0.5 g, and 0.3 g, $\text{H}_2/\text{CO}(\text{feed}) = 2.12$.

Based on the activity data at the different temperature levels, the activation energy for Fischer-Tropsch synthesis was determined using an Arrhenius plot. The calculations were made at three separate stages in the experiment, at two different conversion levels at dry conditions and once when adding water in the feed. The Arrhenius plot is shown in Figure 4.10 and the activation energy was determined to be in the range 90–95 kJ/mol. This result is in agreement with other reports in the literature on comparable catalysts.^{[31][78][79]} The results also indicate that adding water in the feed does not affect the activation energy of FT reactions notably.

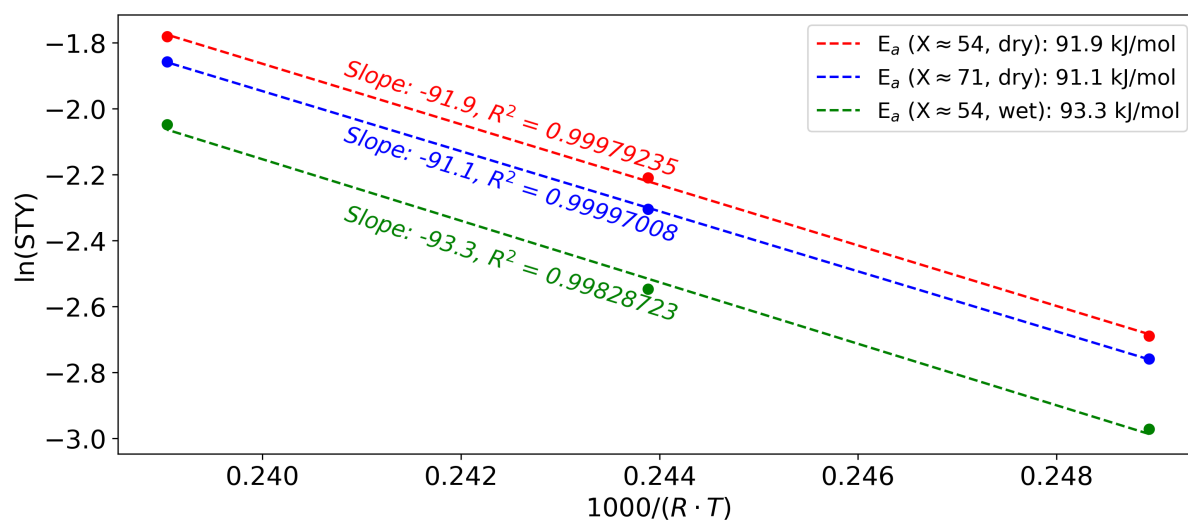


Figure 4.10: Arrhenius plot of three different data sets at each of the three temperatures, 210 °C, 220 °C, and 230 °C. The conversion levels (X) are indicated in the plot and were quite similar at each temperature and for each data set, only deviating within $\pm 0.5\%$.

4.2.3 Effect of Reaction Time

Two separate experiments were executed on respective catalyst batches at a variation of feed gas compositions, with a total duration of 500 hours. No changes to the catalysts were made during this time frame. The mutual conditions for the experiments were: $p = 20$ bar (increased to 22 bar when adding water to the feed) and $H_2/CO = 2.13, 1.75, 1.44,$ and 2.16 . The difference between the two experiments were the temperatures, $T = 210^\circ\text{C}$ and 230°C , and the amount of catalyst used, $m_{\text{cat.}} = 1.0$ g and $m_{\text{cat.}} = 0.3$ g. For illustration, the course of the entire experiment performed at 210°C is shown in Figure 4.11, and displays the variation in conversion level with corresponding variation in selectivities to methane and the C_{5+} fraction. The experiment at 230°C was performed in a similar fashion as the one depicted, and the plots for that experiment can be found in Appendix B.1.

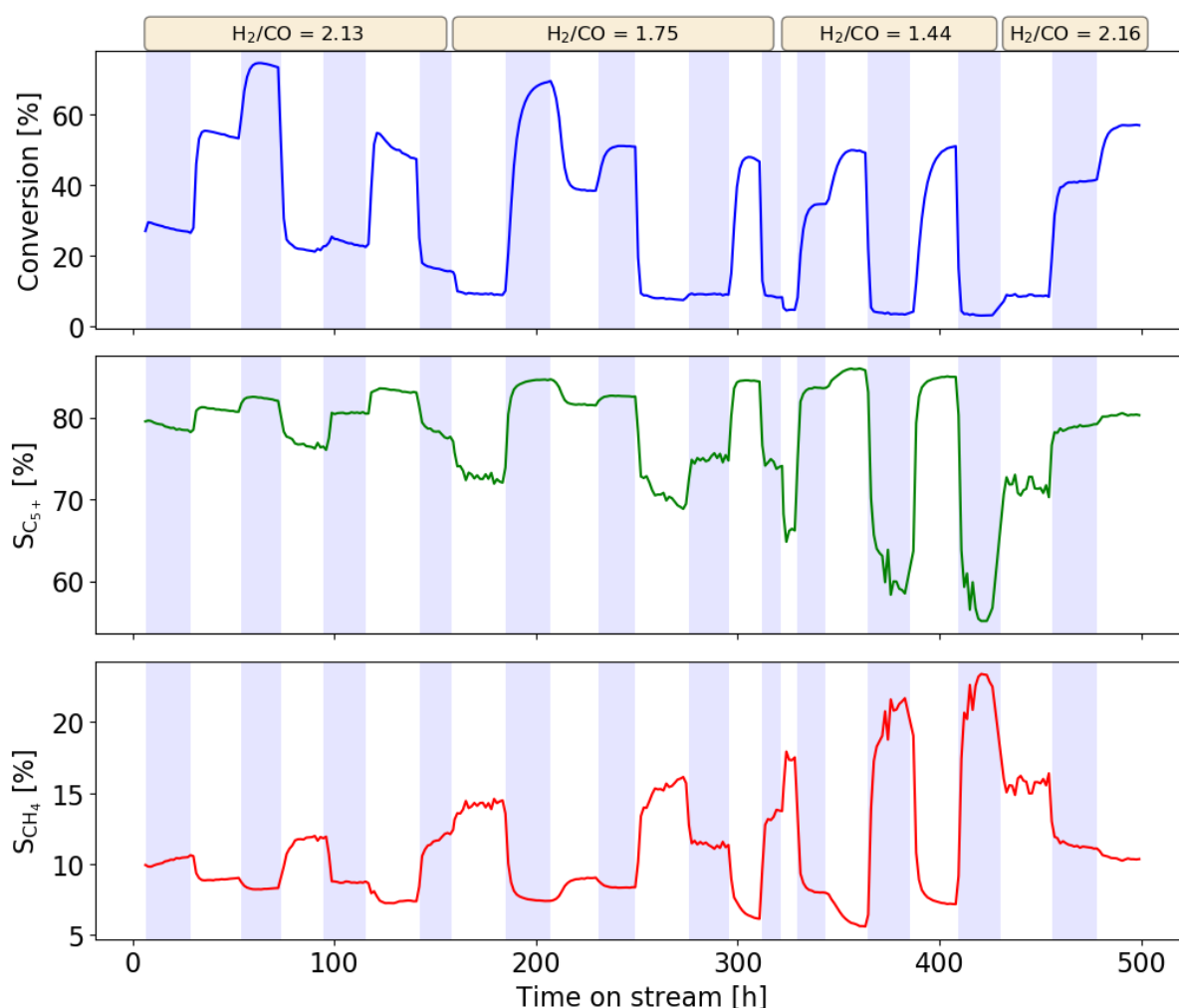


Figure 4.11: Activity and selectivity data of key components. Conditions: $p_{\text{total}} = 20$ bar with $p_{\text{total}} = 22$ bar when adding water in the feed, $T = 210^\circ\text{C}$, $m_{\text{cat.}} = 1.0$ g, $H_2/CO = 2.13, 1.75, 1.44, 2.16$. CO_2 is included in the C_{5+} fraction. The background shading represents changes in the flow rate. Outliers have been omitted.

Evidently, there are some discrepancies from the experimental procedure, e.g. the data points for 50% conversion at $H_2/CO = 1.75$ were collected at a later stage than that

for the 70% setting. In addition, at $H_2/CO = 1.44$ there was one discrepancy from the experimental procedure due to a malfunctioning liquid flow controller, and one when the conversion level was supposed to be increased to 70%. Reaching 70% conversion was not possible for this feed gas composition due to H_2 deficiency lowering the theoretical limit for CO conversion. Therefore, no data points were obtained for step 3 (70% conversion) and 5 (250 mL/min + water) for this feed gas composition. The experiment was finished with a re-run of the initial two steps in the experimental procedure, at equal feed gas composition as the first hours of experiment.²

As indicated in Figure 4.11, the entire span of the experiment is divided into the following subperiods:

1. $H_2/CO = 2.13$: Hours 0 to 160
2. $H_2/CO = 1.75$: Hours 160 to 320
3. $H_2/CO = 1.44$: Hours 320 to 430
4. $H_2/CO = 2.16$: Hours 430 to 500

In this chapter, the intention is to discuss the deactivation effects throughout the two experiments. Therefore, only hours 0 to 55 and 450 to 500 of the experiments will be treated here. Comparing the data obtained at each phase gives valuable information on the extent of catalyst deactivation and how the deactivation affects the overall performance.

Figure 4.12 contains the STY for all stages of both experiments operated at the same flow rate of syngas and at $H_2/CO = 2.13/2.16$. As the figure indicates, the catalysts have suffered heavy deactivation over the course of the experiments. The change in STY over the time frame of roughly 400 hours was about 56% for the experiment at 210 °C and 65% for the experiment at 230 °C. As presented in Chapter 4.2.1, a linear deactivation model seemed suitable to describe the activity loss during those experiments. However, it was mentioned that long-term operation would yield a different deactivation trend. The deactivation in the early hours of experiment had a certain linear trend also here, but in the late stages, the activity loss was less severe. For illustration, the deactivated catalyst phases are also represented with linear deactivation, however, only considering the two last data points. The slope change in the end phases is only about a four-fold of that for the early phase, substantiating that the rate of deactivation is much less in the later stages of operation. The observed two-stage deactivation has been suggested due to sintering in the initial stage and a combination of coking and re-oxidation as the main long-term deactivation mechanisms.^[40] As discussed previously, the long-term deactivation would likely correspond to a negative exponential function. Such models ($a(t) = c \cdot \exp(-k_{\text{deact.}} \cdot t)$) were fitted to the data sets, and is also indicated in the figure. Although the deactivation models do not catch the data points perfectly, the long-term trend certainly fits better than a simple linear function.

Using the slopes of the linear representations of the change in activity (Figure 4.12) as

²Note that the feed gas composition was 2.13 in the initial hours while it was 2.16 in the last hours of the experiment. This is due to a syngas bottle change during the experiment and a small deviation in the composition of the two. The deviation is, however, so small that it is within the experimental uncertainty, and should not affect the numbers notably.

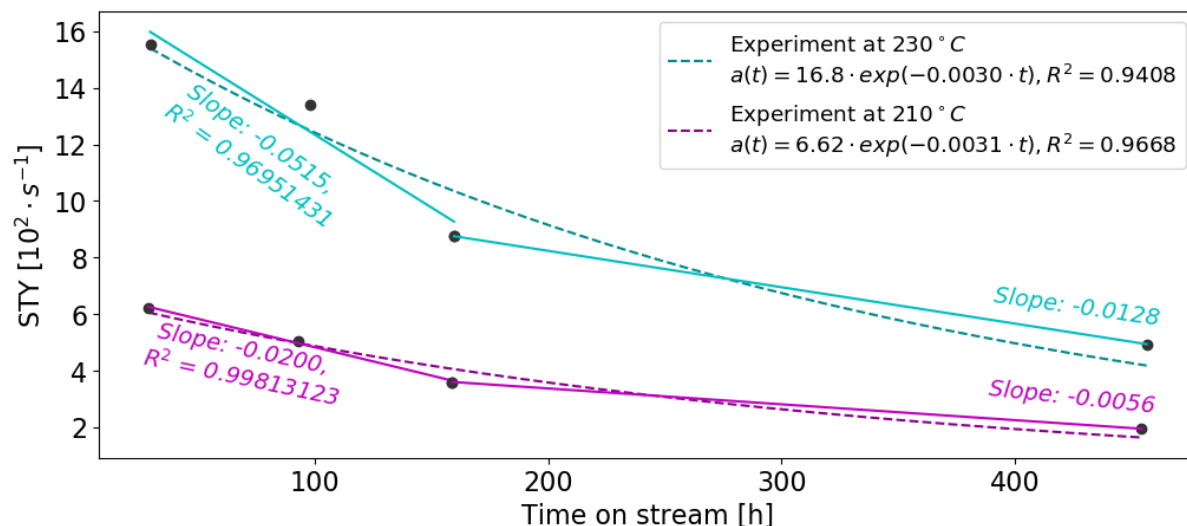


Figure 4.12: Catalyst activities as function of time on stream. Conditions: $p_{\text{total}} = 20$ bar, $T = 210$ °C and 230 °C, $m_{\text{cat.}} = 1.0$ g and 0.3 g $\text{H}_2/\text{CO}(\text{feed}) = 2.13$ (three first data points) and 2.16 (last data point). Syngas flow rate was 250 mL/min in all instances.

references, it is evident that the experiment at the elevated temperature suffers a far sharper deactivation, where the rate of deactivation is roughly twice as fast at 230 °C than 210 °C. This result is in agreement with what has been found by others^[40]. As discussed previously, all the main deactivation mechanisms – sintering, re-oxidation, and coking – are strong functions of temperature, such that the observed effect of stronger deactivation at elevated temperature was as expected. It is, however, necessary to keep in mind the differences in conversion levels throughout the experiments leading to differences in partial pressures of all the associated species, especially water, and that this also affects the rate of deactivation.

Comparison of the selectivities to CO_2 , CH_4 and C_{5+} for the experiment at 210 °C in Table 4.4 shows that deactivation also affects the selectivities.

Table 4.4: Activity and selectivities for the fresh catalyst phase and the deactivated catalyst phase for both experiments, all at approximately 53% conversion. Conditions: $p_{\text{total}} = 20$ bar, $T = 210$ °C and 230 °C with corresponding $m_{\text{cat.}} = 1.0$ g and 0.3 g, $\text{H}_2/\text{CO} = 2.13/2.16$.

Phase	TOS [h]		Flow rate [mL/min]		STY [$10^2 \times 1/\text{s}$]		S(CO_2) [%]		S(CH_4) [%]		S(C_{5+}) ^a [%]	
	210 °C	230 °C	210 °C	230 °C	210 °C	230 °C	210 °C	230 °C	210 °C	230 °C	210 °C	230 °C
Fresh ^b	53	53	134.0	100.0	6.70	16.5	0.18	0.40	9.0	12.3	80.8	77.7
Deact. ^c	482	487	60.0	35.0	2.95	5.75	0.31	0.71	10.6	13.0	80.4	78.3

^a Reported as CO_2 -free, i.e. $S(\text{C}_{5+}) = 100\% - \sum S_{\text{hydrocarbons}}$.

^b Fresh catalyst phase: hours 0 to 55 ($\text{H}_2/\text{CO} = 2.13$).

^c Deactivated catalyst phase: hours 450 to 500 ($\text{H}_2/\text{CO} = 2.16$).

CO_2 formation was just shy of doubled and the selectivity to methane increased by about 15%, while the selectivity to C_{5+} was as good as unchanged, only displaying a slight decrease. Hence, it appears that the rate of hydrogenation increases and the water-gas shift reaction has a greater impact on the deactivated catalyst, while the chain-growth

probability is more or less preserved. The olefin-to-paraffin ratios for all C₂-C₄ species are listed in Table 4.5 for both the fresh catalyst phase and the deactivated catalyst phase of the experiment. Clearly, the olefin-to-paraffin ratio decreased in all instances during the course of the experiment.

Table 4.5: Olefin-to-paraffin ratios for fresh catalyst phase and the deactivated catalyst phase for both experiments, all at approximately 53 % conversion. Conditions: $p_{\text{total}} = 20$ bar, T = 210 °C and 230 °C with corresponding $m_{\text{cat.}} = 1.0$ g and 0.3 g, $H_2/CO = 2.13/2.16$.

Phase	TOS		Flow rate		S(C ₂₌)/S(C ₂₋)		S(C ₃₌)/S(C ₃₋)		S(C ₄₌)/S(C ₄₋)	
	[h]		[mL/min]		[%/%]		[%/%]		[%/%]	
	210 °C	230 °C	210 °C	230 °C	210 °C	230 °C	210 °C	230 °C	210 °C	230 °C
Fresh ^a	53	53	134	100	0.16	0.04	2.11	1.22	1.32	0.76
Deact. ^b	482	487	60	35	0.08	0.04	1.86	1.26	1.15	0.84

^a Fresh catalyst phase: hours 0 to 55 ($H_2/CO = 2.13$).

^b Deactivated catalyst phase: hours 450 to 500 ($H_2/CO = 2.16$).

Interestingly, the same comparisons made for the 230 °C experiment shows deviating trends, as shown in Table 4.4. Here, the selectivity to methane increased only by about 5 %, which is much less than the 15 % observed for the 210 °C experiment. The two experiments also displayed different trends in the selectivity to C₅₊, whereas a slight decrease was observed during the 210 °C experiment, the 230 °C experiment shows an increase in C₅₊ selectivity. One effect that could cause the observed differences in selectivity is increased average particle size as a result of sintering. As mentioned, sintering is a strong function of temperature, leading to more larger cobalt particles at higher temperatures. And with the positive correlation between cobalt particle size and selectivity to heavy hydrocarbons being well-established^{[26] [57]}, it is expected that this plays a significant role in the observed differences in product selectivity.

Similarly, by comparing the olefin-to-paraffin ratios given in Table 4.5, the trends are opposite for the 230 °C experiment from what was observed for the 210 °C experiment. One contributing factor to this is likely the differences in flow rates of the feed gas. The flow rate necessary to obtain 53 % conversion in the 230 °C experiment was just above half of that for the 210 °C experiment. Hence, the residence time was much longer, facilitating re-adsorption of olefins on the catalytic surface with succeeding hydrogenation of the adsorbed olefins to form paraffins.^[21]

4.2.4 Effect of Feed Gas Composition

Five experiments were conducted using different feed gas compositions, all at two different temperatures. The feed gas compositions were $H_2/CO = 1.12, 1.41, 1.72, 2.13$ and 2.55 , with corresponding catalyst loading $m_{cat.} = 4.0\text{ g}/1.5\text{ g}, 1.85\text{ g}/0.5\text{ g}, 1.5\text{ g}/0.6\text{ g}, 1.0\text{ g}/0.3$, and $0.9\text{ g}/0.35\text{ g}$ for temperatures $210\text{ }^\circ\text{C}/230\text{ }^\circ\text{C}$.

Figure 4.13 shows the kinetic activity evolution in the all experiments at $210\text{ }^\circ\text{C}$. The syngas flow rate was $250\text{ mL}/\text{min}$ in all instances, and the data points are fitted to trend lines, which are represented with their corresponding slopes.

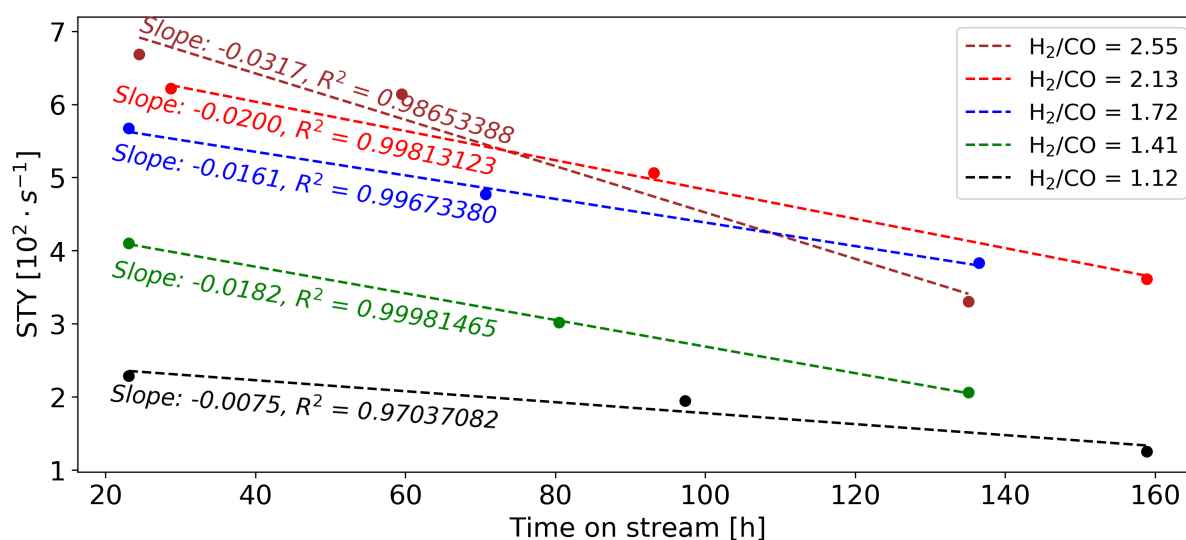


Figure 4.13: Catalyst deactivation at different feed gas compositions. Conditions: $T = 210\text{ }^\circ\text{C}$, $p = 20\text{ bar}$, $H_2/CO = 1.12, 1.41, 1.72, 2.13$ and 2.55 with corresponding $m_{cat.} = 4.0\text{ g}, 1.85\text{ g}, 1.5\text{ g}, 1.0\text{ g}$ and 0.9 g . Syngas flow rate was $250\text{ mL}/\text{min}$ in all instances.

Although not entirely consistent, given that the deactivation is more severe at $H_2/CO = 1.41$ than that for $H_2/CO = 1.72$, comparison of the slopes at the various feed gas ratios clearly shows a trend where the catalyst suffers less deactivation as the H_2/CO ratio is decreased. Considering that sintering is only a function of temperature^[33] and that coking is more critical at low H_2/CO ratios^[34], it is probable that the third of the topical main deactivation mechanisms, oxidation, is crucially dependent on the feed gas composition. This statement is in good agreement with the literature, whereas Sadeqzadeh *et al.*^[40] found the same trends in their experiments. They studied deactivation on a $CoPt/\gamma-Al_2O_3$ catalyst at H_2/CO ratios of 1, 2 and 4 and used semi-mechanistic models to fit the observed deactivation. They found that at $H_2/CO = 1$, a deactivation model only regarding water-assisted sintering offered a satisfactory fit to the experimental data. At H_2/CO ratios of 2 and 4, it did however not. It was thus suggested that at higher H_2/CO ratios other deactivation mechanisms, mainly surface oxidation, becomes prominent. Zhou *et al.*^[80] investigated the deactivation effects on a silica-supported cobalt catalyst at different H_2/CO ratios and characterized both the fresh and spent catalyst with TPR and X-ray photoelectron spectroscopy (XPS). They found that for the spent catalyst cobalt silicates and/or hydrosilicates had been formed and that the amounts formed increased with increased synthesis gas composition. In addition, the amount of silicates formed

highly correlated with the observed rate of deactivation, hence it was concluded that silicates formation was the main reason for deactivation. Considering that similar surface interactions with the support have also been reported on alumina supported catalysts^[81], whereas cobalt aluminates-like species were formed, the observation that higher H_2/CO ratios lead to higher rates of deactivation due to cobalt silicate formation may also be relevant for alumina supported catalysts. Therefore it is probable that a combination of increased aluminate formation and increased surface oxidation is the main explanation for the observations made here.

A similar plot has been prepared for the experiment at 230 °C and is shown in Figure 4.14. These results are also somewhat conflicting, although the trend of an increased rate of deactivation with increasing H_2/CO ratio is evident, at least when comparing the extremes.

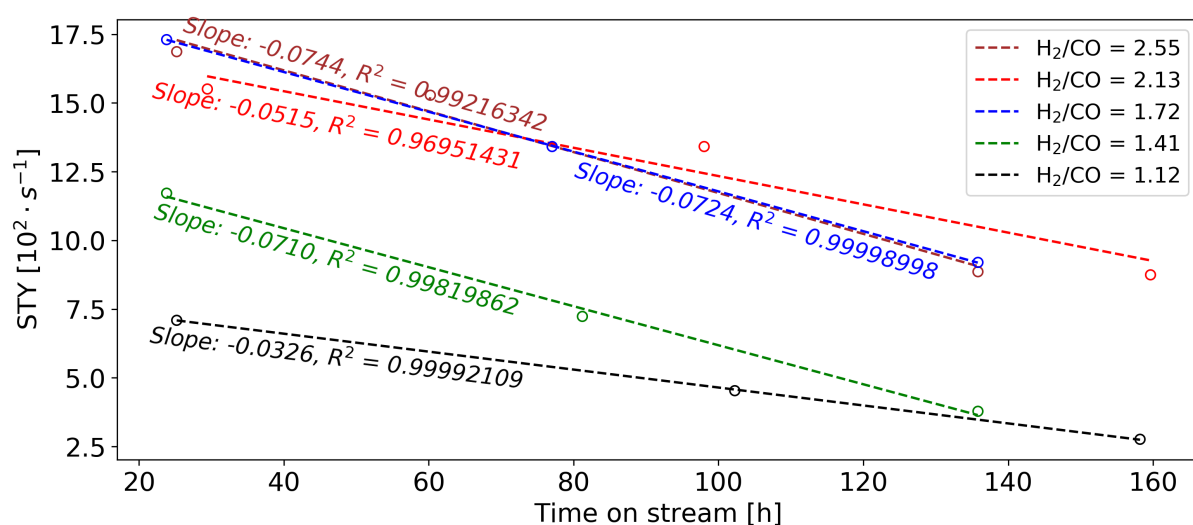


Figure 4.14: Catalyst deactivation at different feed gas compositions. Conditions: $T = 230\text{ °C}$, $p = 20\text{ bar}$, $H_2/CO = 1.12, 1.41, 1.72, 2.13$ and 2.55 with corresponding $m_{\text{cat.}} = 1.5\text{ g}, 0.5\text{ g}, 0.6\text{ g}, 0.3\text{ g}$ and 0.35 g . Syngas flow rate was 250 mL/min in all instances.

Similarly to the rate of change in the activity being observed to be different for all the various H_2/CO ratios, the effect that water has on the activity is also different. This is shown in Figure 4.15, where the STY is normalized with respect to the activity just prior to adding water to the feed and the relative change in activity is illustrated. Evidently, in the majority of the experiments addition of water yields an immediate positive response in activity followed by a steady decline. Although not entirely consistent, the response to water seems to be somewhat correlated to both temperature and feed gas composition, in that the effect of adding water is more forceful at the higher temperature and high H_2/CO ratios. The neutral/negative responses were observed for the two experiments at 210 °C with the lowest H_2/CO ratio, which incidentally also were the ones that had the lowest activity to begin with.

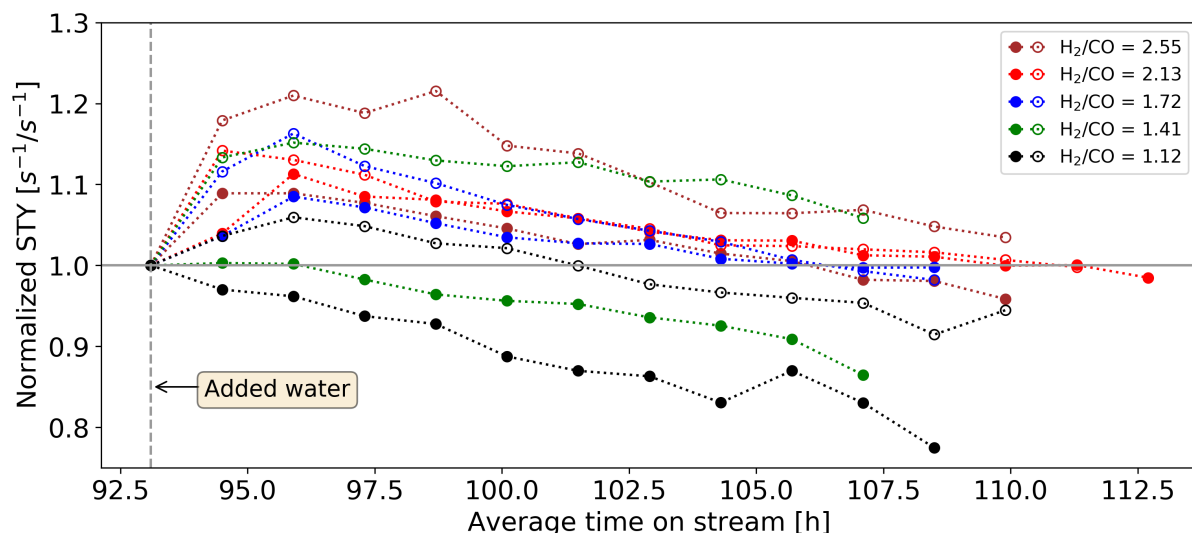


Figure 4.15: Effect of adding water at different feed gas compositions and temperatures. The pressure was increased from 20 bar in the first data point to 22 bar in the consecutive data points, where 2 bar of water was added. $H_2/CO = 1.12, 1.41, 1.72, 2.13$ and 2.55 with corresponding $m_{cat.} = 4.0\text{ g}/1.5\text{ g}, 1.85\text{ g}/0.5\text{ g}, 1.5\text{ g}/0.6\text{ g}, 1.0\text{ g}/0.3\text{ g}$ and $0.9\text{ g}/0.35\text{ g}$ at $T = 210\text{ }^\circ\text{C}$ (filled symbols)/ $230\text{ }^\circ\text{C}$ (open symbols). Syngas flow rate was $250\text{ mL}/\text{min}$ in all instances. The STY is normalized with respect to the individual STY just prior to adding water.

Table 4.6 contains the difference in activity and selectivity as a result of adding water to the feed.

Table 4.6: Changes in activity and selectivity before and after adding water to the feed, for all the various feed gas compositions. The data are given as the difference between the last data point obtained at steady-state while feeding water and the last data point obtained at steady-state before adding water. Conditions: $p_{total} = 20\text{ bar}$ with $p_{total} = 22\text{ bar}$ when adding 2 bar water in the feed, $H_2/CO = 1.12, 1.41, 1.72, 2.13$ and 2.55 with corresponding $m_{cat.} = 4.0\text{ g}/1.5\text{ g}, 1.85\text{ g}/0.5\text{ g}, 1.5\text{ g}/0.6\text{ g}, 1.0\text{ g}/0.3\text{ g}$ and $0.9\text{ g}/0.35\text{ g}$ at $T = 210\text{ }^\circ\text{C}/230\text{ }^\circ\text{C}$. Syngas flow rate was $250\text{ mL}/\text{min}$ in all instances.

H_2/CO	ΔSTY [$10^2 \times 1/s$]		$\Delta S(CO_2)$ [%]		$\Delta S(CH_4)$ [%]		$\Delta S(C_{5+})^a$ [%]		$\Delta o/p^b$ [%/%]	
	210 °C	230 °C	210 °C	230 °C	210 °C	230 °C	210 °C	230 °C	210 °C	230 °C
1.12	-0.30	0.03	0.78	0.28	-0.45	-1.50	-2.83	3.06	0.54	0.54
1.41	-0.31	1.06	0.36	0.05	-1.29	-3.73	0.49	6.83	0.59	0.48
1.72	-0.01	-0.24	0.03	0.15	-2.23	-2.69	2.76	4.90	0.40	0.50
2.13	0.21	-0.03	0.04	0.20	-3.14	-2.77	4.17	4.42	0.41	0.52
2.55	-0.25	1.04	0.16	0.13	-3.17	-4.00	4.66	6.54	0.32	0.38

^a Reported as CO_2 -free, i.e. $S(C_{5+}) = 100\% - \sum S_{hydrocarbons}$.

^b Total olefin-to-paraffin ratio for C_2 - C_4 species.

The difference is taken at steady-state conditions before adding water and while feeding water, with between 15 and 23 hours of water addition. All positive, negative and neutral effects of water on the activity was observed, with no obvious trend onto what dictates the effect. This is an interesting result given the hypothesis that pore characteristics

determine the effect of water on the kinetics.^{[24][25]} Since all experiments were performed on the same catalyst it is expected that the pore structure variation is negligible between the batches. Hence, the various feed gas compositions must either influence the pore structure differently during the reaction, or the kinetic effect of water must be more complex than solely a pore characteristics phenomenon.

The water effect on selectivities is, however, more clear-cut. Except for the experiment with $H_2/CO = 1.12$ at $210\text{ }^\circ\text{C}$, the C_{5+} selectivity is elevated when feeding water, moreover, CO_2 and olefin-to-paraffin selectivity increased, while methane formation was constrained. The effect of water does seem to have some dependency on the H_2/CO ratios, whereas a more forceful effect of water is observed on methane, C_{5+} and olefin-to-paraffin ratios for C_3 - C_4 when increasing the H_2/CO ratio. The grounds for comparison is, however, rather poor due to differences in conversion levels, such that it is difficult to conclude.

Comparison of the selectivities at the various feed gas compositions was done at approximately 50 % conversion, with the results rendered in Table 4.7. Increasing the H_2/CO ratio leads to increased methane formation and decreased CO_2 , C_{5+} and olefin-to-paraffin formation. Intuitively this is an expected result, as a higher H_2/CO ratio increases the number of adsorbed hydrogen atoms on the cobalt surface and simultaneously decreases the $-CH_2$ monomer concentration. This leads to higher hydrogenation activity, resulting in enhanced formation of methane and saturated hydrocarbons, and a reduction in C_{5+} formation.

Table 4.7: Activity and selectivity of key components at similar CO conversion level. Conditions: $p_{\text{total}} = 20$ bar, $H_2/CO = 1.12, 1.41, 1.72, 2.13$ and 2.55 with corresponding $m_{\text{cat.}} = 4.0\text{ g}/1.5\text{ g}, 1.85\text{ g}/0.5\text{ g}, 1.5\text{ g}/0.6\text{ g}, 1.0\text{ g}/0.3\text{ g}$ and $0.9\text{ g}/0.35\text{ g}$ at $T = 210\text{ }^\circ\text{C}/230\text{ }^\circ\text{C}$.

H_2/CO	Flow rate [mL/min]		Conversion [%]		S(CO_2) [%]		S(CH_4) [%]		S(C_{5+}) ^a [%]		o/p ^b [%/%]	
	210 °C	230 °C	210 °C	230 °C	210 °C	230 °C	210 °C	230 °C	210 °C	230 °C	210 °C	230 °C
1.12	32.7	37.5	46.6	46.0	12.0	12.9	3.9	5.5	87.0	85.8	2.8	2.1
1.41	120	90	48.4	48.1	0.6	1.1	6.0	7.7	86.6	85.3	2.1	1.5
1.72	150	190	46.7	49.9	0.3	0.5	8.0	10.1	84.0	81.2	1.4	1.0
2.13	134	100	46.0	51.5	0.2	0.4	9.4	11.8	81.0	79.2	1.3	0.8
2.55	140	135	49.5	48.0	0.2	0.4	10.9	14.1	79.4	76.2	1.1	0.7

^a Reported as CO_2 -free, i.e. $S(C_{5+}) = 100\% - \sum S_{\text{hydrocarbons}}$.

^b Total olefin-to-paraffin ratio for C_2 - C_4 species.

Note the high selectivity to CO_2 measured in the experiments with a H_2/CO ratio of 1.12. This phenomenon is discussed in depth in Chapter 4.2.6.

4.2.5 Catalyst Regeneration

After the experiments performed with a H_2/CO ratio of 1.41 with approximately 135 h time on stream, the catalysts were regenerated according to the low pressure regeneration (LPR) procedure described in Chapter 3.3.2. The conversion and selectivity measurements for both the experiment performed at 210 °C and the one at 230 °C are shown in Figure 4.16 and includes the first and the last hours of experiment, as well as the first hours after regeneration. The conditions were identical in all instances, with 20 bar pressure and syngas flow rate of 250 mL/min.

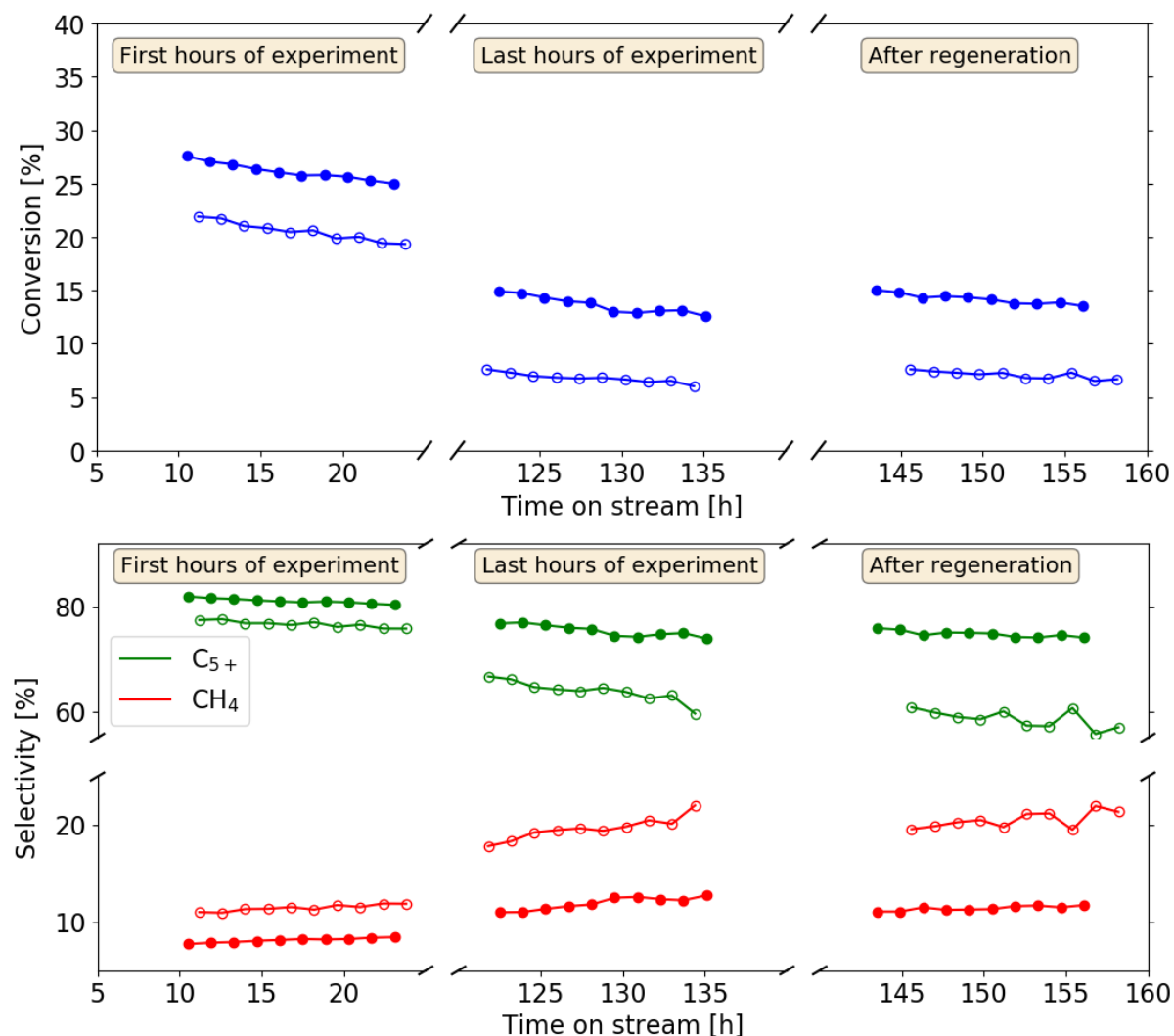


Figure 4.16: Regeneration effects using the LPR procedure. Conversion (top) and selectivity (bottom) measurements of the experiment at 210 °C (filled symbols) and at 230 °C (open symbols). All three stages were performed at 20 bar pressure, with syngas flow rate of 250 mL/min, and at a H_2/CO ratio of 1.41.

As shown in Figure 4.16 the regeneration restores some of the activity, however, the effect appears to be marginal. Comparing the conversion in the last hours of experiment with that after regeneration, only about 5 % of the activity is regained. Neither did the regeneration seem to affect the selectivities notably, whereas the selectivity to C_{5+} and

methane was observed to remain more or less unchanged in the 210 °C experiment. A change was, however, observed in the selectivity to C₅₊ in the 230 °C experiment in which it decreased by about 8 %, although it should be mentioned that the conversion level, in this case, was rather low and that it has been observed that the selectivity measurements tend to fluctuate at low conversions in other experiments performed in this thesis, such that the data could be difficult to interpret. Nonetheless, only small changes were observed as a result of the regeneration. The most clear-cut result was perhaps the strictly decrease in olefin-to-paraffin ratios for all C₂-C₄ species, as shown in Table 4.8, although the effect is so small that it probably is linked to the differences in conversion levels rather than a direct effect of regeneration.

Table 4.8: Olefin-to-paraffin ratios at the first and last hours of experiment, and after regeneration. The selectivity to CO₂ is also included. The numerical values given are averages of ten data points obtained at steady-state. Conditions: $p_{\text{total}} = 20$ bar, T = 210 °C and 230 °C, $m_{\text{cat.}} = 1.85$ g and 0.5 g, H₂/CO(feed) = 1.41. Syngas flow rate was 250 mL/min in all instances.

Stage	TOS [h]		Conversion [%]		STY [10 ² × 1/s]		S(CO ₂) [%]		S(C ₂₌ /C ₂₋) [%/%]		S(C ₃₌ /C ₃₋) [%/%]		S(C ₄₌ /C ₄₋) [%/%]	
	210 °C	230 °C	210 °C	230 °C	210 °C	230 °C	210 °C	230 °C	210 °C	230 °C	210 °C	230 °C	210 °C	230 °C
First hours	16.8	17.5	26.1	20.5	4.3	12.4	0.33	0.54	0.27	0.15	3.61	3.13	2.48	2.12
Last hours	128.8	128.1	13.6	6.8	2.2	4.1	0.46	0.91	0.36	0.29	3.81	4.08	2.60	2.80
After regen.	149.8	151.9	14.2	7.1	2.3	4.3	0.50	0.95	0.27	0.22	3.55	3.90	2.44	2.67

Considering the hypothesis that water-induced deactivation by re-oxidation of the active cobalt metal along with sintering are the two main deactivation mechanisms at play in the time frame investigated here, and that CO₂ formation is expected to transpire on the oxidized cobalt sites (CoO)^[82], it would be anticipated that the formation of CO₂ is proportional to the degree of deactivation by re-oxidation. Hence, the observation that the selectivity to CO₂ does not decrease after regeneration (Table 4.8) is surprising. In fact, a slight increase in selectivity to CO₂ was observed, although this is expected to be linked to the slightly higher conversion level with a consequently slightly higher partial pressure of water in the system. Hence, the results indicate that the regeneration procedure used here mainly changed the surface concentration of various species, e.g. hydrogenating and removing hydrocarbons deposited on the surface and that no notable reduction of CoO occurred.

Due to the small effects of regeneration using the LPR, another regeneration procedure was attempted, namely the operating conditions regeneration (OCR) procedure, as described in Chapter 3.3.2. The regeneration was initiated after the H₂/CO = 2.55 experiment, and the only difference between the two regeneration procedures was the conditions at which the reactor purging was carried out. As shown in Figure 4.17, the effect of regenerating the catalyst using OCR was greater than that for LPR, whereas the site time yield increased by 15 % and 8 % for the 210 °C and 230 °C experiments, respectively.

Due to the differences in conversion levels, the grounds for comparison of selectivities before and after regeneration are poor. It was therefore decided to operate one more day, increasing the conversion to a comparable level as in the early stages of the experiment such that the selectivities could be compared. The comparison is shown in Table 4.9, and the comparison is made at approximately 50 % conversion for both temperature levels.

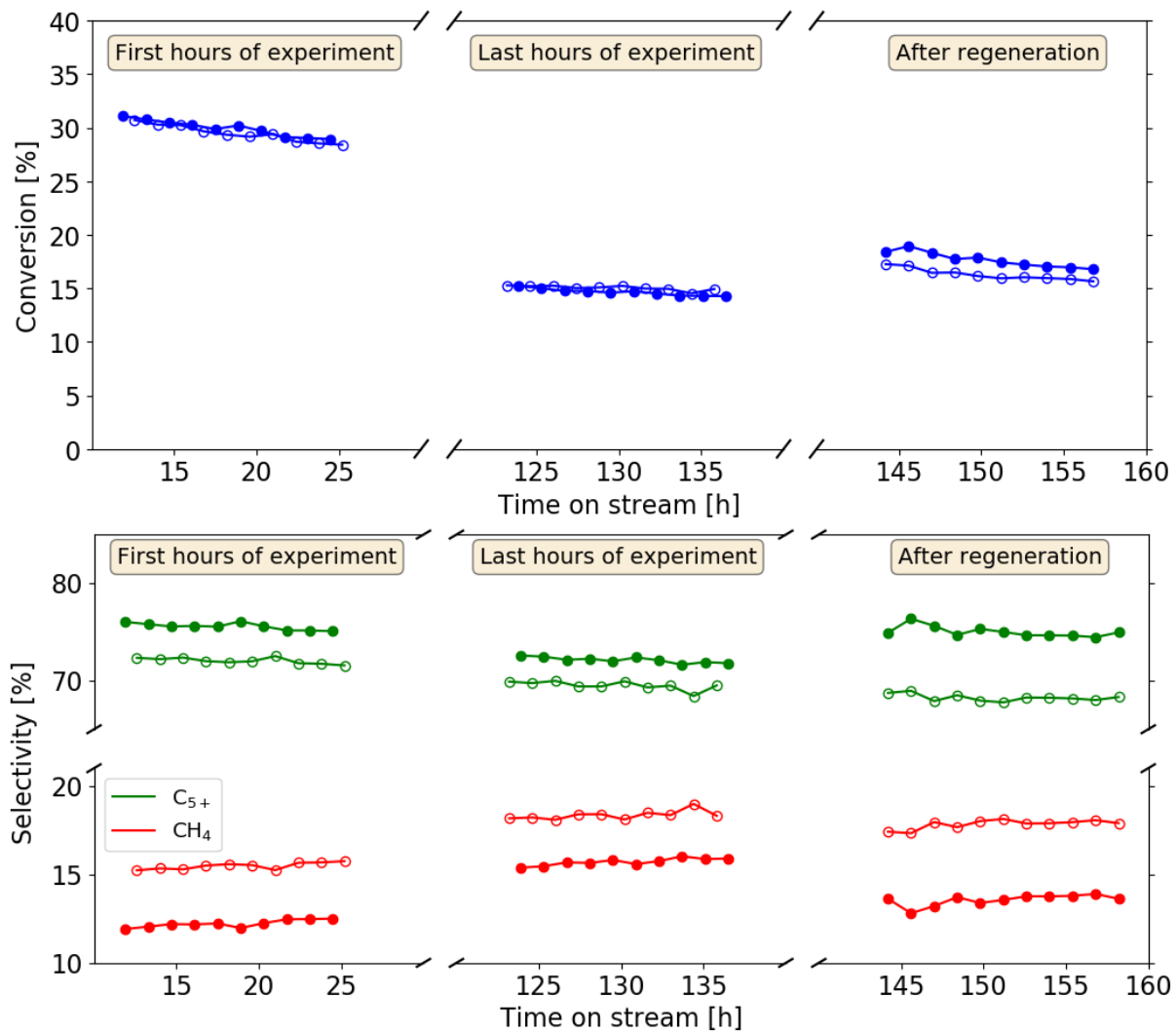


Figure 4.17: Regeneration effects using the OCR procedure. Conversion (top) and selectivity (bottom) measurements of the experiment at 210 °C (filled symbols) and at 230 °C (open symbols). All three stages were performed at 20 bar pressure, with syngas flow rate of 250 mL/min, and at a H_2/CO ratio of 2.55.

Table 4.9: Selectivities of key components at approximately 50% CO conversion before and after regeneration. Conditions: $p_{\text{total}} = 20$ bar, $H_2/CO = 2.55$, $T = 210$ °C and 230 °C with corresponding $m_{\text{cat.}} = 0.9$ g and 0.35 g.

Stage	TOS [h]		STY $[[10^2 \times 1/s]$		$S(CO_2)$ [%]		$S(CH_4)$ [%]		$S(C_{5+})^a$ [%]		o/p^b [%/%]	
	210 °C	230 °C	210 °C	230 °C	210 °C	230 °C	210 °C	230 °C	210 °C	230 °C	210 °C	230 °C
Before regen.	25	26	6.4	15.4	0.22	0.37	10.9	14.1	79.4	76.2	1.08	0.68
After regen.	168 (23) ^c	169 (24) ^c	4.7	10.4	0.20	0.33	10.7	14.7	80.4	75.1	1.21	0.68

^a Reported as CO_2 -free, i.e. $S(C_{5+}) = 100\% - \sum S_{\text{hydrocarbons}}$.

^b Total olefin-to-paraffin ratio for C_2 - C_4 species.

^c Time on stream including experimental time with time on stream after regeneration in parenthesis.

As the selectivity data in Table 4.9 indicate, the regeneration provided different results in the two experiments. In the experiment at 210 °C an increase in olefin-to-paraffin ratio and selectivity to C₅₊ is observed, along with a decrease in selectivity to methane. This is in contrast to the increase in methane selectivity and decrease in C₅₊ selectivity for the experiment at 230 °C. Bearing in mind the inferior effect of regeneration on the kinetic activity at the higher temperature and the correlation between temperature and rate of deactivation, as discussed in Chapter 4.2.4, it is likely that the deactivation mechanisms favored at elevated temperatures are more difficult to reverse. Obvious candidates are coke deposition, re-oxidation, and sintering, all being strong functions of temperature. Although carbon depositions are found to be present on catalysts in both atomic and polymeric form, with the latter being resistant to hydrogen treatment above the FT synthesis temperature^[41], and therefore would not be reversed using either of the two regeneration procedures, it is a slow process and is not expected to be significant during the time frame of these experiments anyway. Hence, it is probable that sintering and re-oxidation are the main causes of deactivation, and that these are slightly reversed here. The decrease in selectivity to CO₂ observed (albeit very weak) indicates that some of the oxidized sites were reduced in the regeneration. In total, it is evident that the regeneration procedures attempted here did not result in a mentionable rejuvenation of the catalyst activity. Regeneration procedures found in the literature are usually conducted by pre-treatment of the catalyst before the reduction is attempted.^{[42][83]} This is done using an inert solvent to remove wax deposits from the catalyst pores followed by calcination at high temperatures to oxidize the cobalt metal. Using this procedure, successful regeneration was achieved, and the pre-treatment steps were identified as key both for re-dispersing the cobalt and to remove deposited carbon. Considering that sintering is the main cause for deactivation during the time frames studied here, it is likely that this can not be reversed to a large extent without oxidizing the catalyst prior to reduction.

4.2.6 Water-Gas Shift Activity

Cobalt-based catalysts are often claimed to display negligible or low activity towards the WGS reaction [34][82][83]. However, given appropriate reaction conditions, the WGS reaction may come into action. Marion *et al.* [82] performed experiments at high conversions to induce WGS activity. They reported that cobalt catalysts develop WGS activity that can become significant at the expense of the FT reactions given a specific criterion based on the $\text{H}_2\text{O}/\text{H}_2$ molar ratio in the reactor, namely if the ratio exceeds unity. They also observed that the process was both reversible and that the reversibility was close to instantaneous, and hence favored a hypothesis for the modification in selectivity (WGS versus FTS) based on the competition between H_2 and H_2O to react with CO. This hypothesis was favoured at the expense of water-induced re-oxidation of cobalt metal to form WGS active cobalt oxides, mostly due to kinetic considerations regarding the reversibility of the process.

The WGS reaction was also observed to become significant in the experiments performed using low H_2/CO ratios in this work. The most extensive effect was observed in the two experiments performed with a H_2/CO ratio of 1.12, with the effect diminishing as the H_2/CO ratio was increased. The experiment at 210°C and $\text{H}_2/\text{CO} = 1.12$ is used as an illustration here, whereas the selectivity to CO_2 reached a maximum of about 12%. This phenomenon took place at the highest conversion level obtained for the given feed gas composition, 46.6%, which is about 87% of the theoretical maximum at the given conditions. The right-hand plot in Figure 4.18 contains the calculated molar ratio of H_2O and H_2 plotted as function of CO conversion.

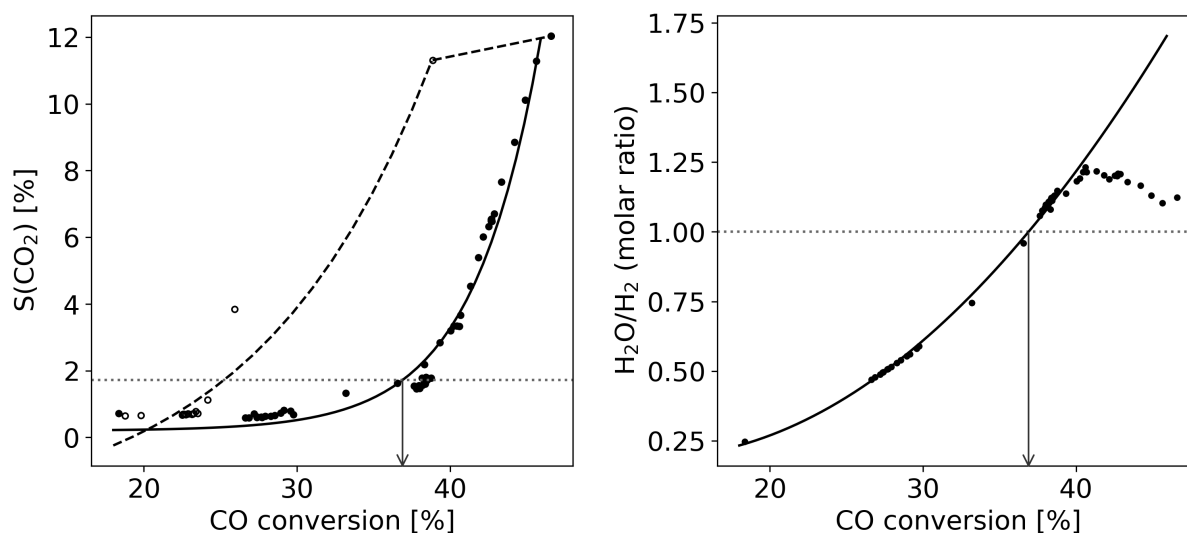


Figure 4.18: Relationships between the CO_2 selectivity, CO conversion, and molar ratio of H_2O and H_2 . Filled symbols represents data points collected when increasing the conversion, while hollow symbols denotes the return to low conversions. Conditions: $\text{H}_2/\text{CO} = 1.12$, $m_{\text{cat.}} = 4.0$ g, $T = 210^\circ\text{C}$, $p = 20$ bar.

Evidently, the $\text{H}_2\text{O}/\text{H}_2$ molar ratio exceeds unity at the high conversions. Translating the molar ratio into the plot of the selectivity to CO_2 as a function of CO conversion, as shown in the left-hand plot, clearly demonstrates that surpassing unity for the molar ratio

accelerates the WGS activity intensively. The figure also shows the reversibility of the phenomenon, where a rapid decline in WGS activity is observed and the selectivity to CO_2 is fully reversed shortly after lowering the conversion level. Water-induced re-oxidation of cobalt metal to WGS active cobalt oxides has been postulated to be the main cause of the elevated CO_2 formation previously in this thesis, however, another pathway for CO_2 formation may also be of relevance here. The Boudouard reaction is a disproportionation reaction of carbon monoxide into CO_2 and elemental carbon, $2 \text{CO} \rightleftharpoons \text{CO}_2 + \text{C}$, and although it is favored at higher temperatures than those under investigation here^[50], it is possible that this pathway may be relevant under these extreme hydrogen depleted conditions. Considering that the elemental carbon formed in the Boudouard reaction would deposit onto the surface of the catalyst and cause fouling, a notable drop in kinetic activity would be observed if this reaction was significant. This was, however, not observed given that the topical experiment displayed the lowest degree of deactivation of all experiments, as was presented in Chapter 4.2.4. Hence, it is probable that the Boudouard reaction does not play a significant role in the formation of CO_2 in this instance, such that cobalt re-oxidation arises as the preferred hypothesis to explain the phenomenon.

The effect is, however, not as substantial in the instance when water was added to the feed, as indicated in Figure 4.19.

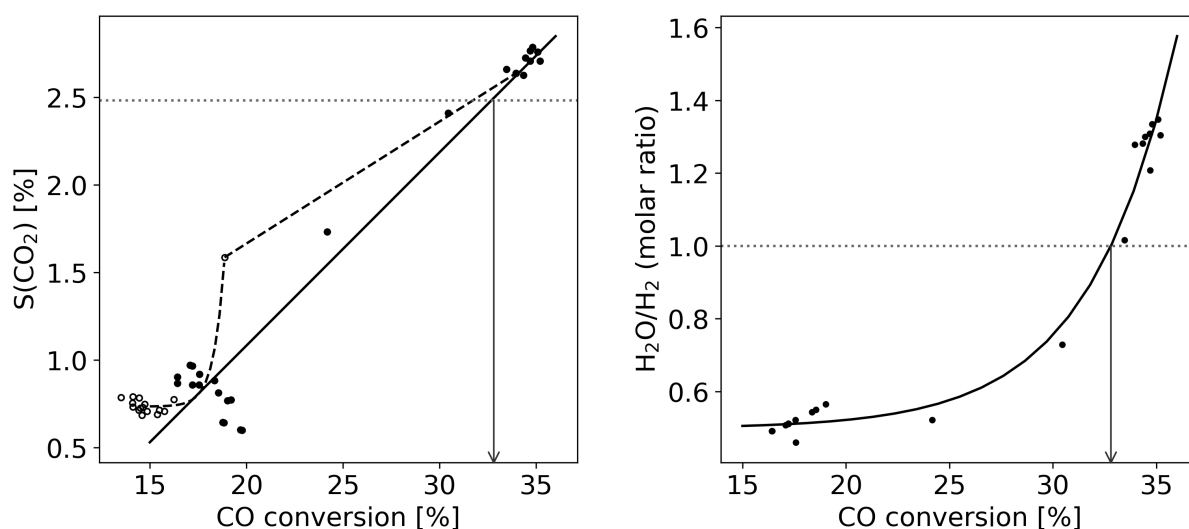


Figure 4.19: Relationships between the CO_2 selectivity, CO conversion, and molar ratio of H_2O and H_2 when adding water to the feed. Filled symbols represents data points collected when increasing the conversion, while open symbols denotes the return to low conversions. Conditions: $\text{H}_2/\text{CO} = 1.12$, $m_{\text{cat.}} = 4.0 \text{ g}$, $T = 210^\circ\text{C}$. The pressure was 22 bar (20 bar syngas and 2 bar water) in instances with filled symbols, and 20 bar for the hollow symbols.

In this case, it was not possible to reach the same conversion level as was reached at “dry” conditions without causing the pressure to drop in the reactor, hence the maximum obtained conversion was about 35 % (approximately 65 % of the calculated limit). Still, the added water resembles higher conversion given the modification of the partial pressure of water in the reactor. The sum of the amount of water that was fed and the water produced in the reaction at the measured conversion level yields a simulated conversion level of 49 %. This corresponds to 91 % of the calculated limit. Considering this, it would be expected

that the response in activity for the WGS reaction would approximate that observed during the “dry” conditions, but the trends are quite different. Although the instance of water added to the feed is not exactly analogous to that of increased conversion level given both the different water pressure gradient throughout the reactor and the differences in the amounts of H_2 and CO present, this result is rather surprising. Concerning the hypothesis that re-oxidized cobalt is the main cause of the formation of CO_2 , this result implies that either does externally added water act differently than indigenous water or that the higher quantity of CO and H_2 present while adding water constrains the potential for re-oxidizing. Since both CO and H_2 are reducing agents and that the externally added water alters the coverage of water, both hypotheses are plausible, hence, a third option is that both these factors govern the effect.

4.2.7 Observations Relevant for All Experiments

Selectivity variation with conversion

The selectivities in the Fischer-Tropsch synthesis is well-documented to be highly dependent on the conversion level.^{[21][84]} Shown in Figure 4.20 are the data obtained from the first three steps in the experimental procedure; (1) constant syngas rate, (2) reduce the syngas flow rate to reach approximately 50 % conversion, (3) reduce syngas flow rate further to reach approximately 70 % conversion. The effects presented here were observed in all experiments, but four of the experiments with different H_2/CO ratios at 210 °C are used for illustration. The effect is clear: increasing conversion leads to increased selectivity to C_{5+} , CO_2 and paraffins, and decreased selectivity to methane.

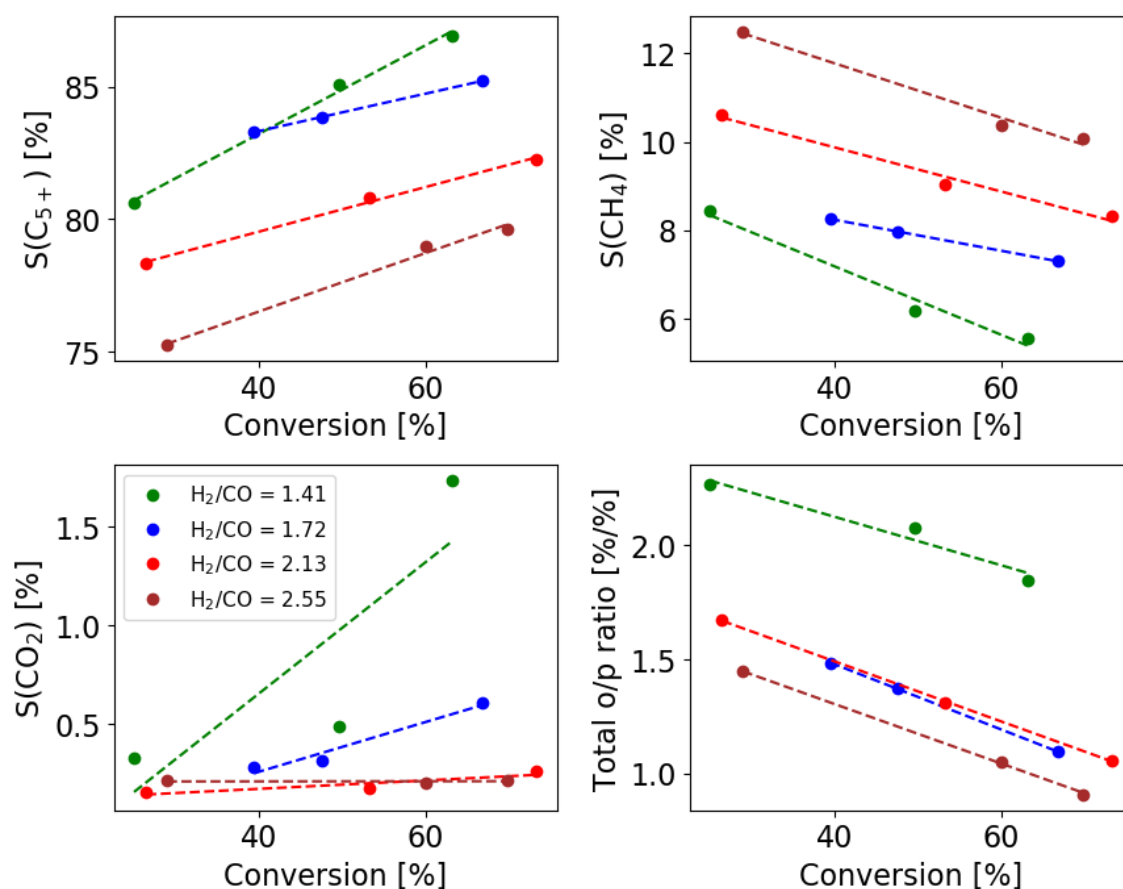


Figure 4.20: Selectivity variation with conversion. Conditions: $p = 20$ bar, $H_2/CO = 1.41, 1.72, 2.13, 2.55$ with corresponding $m_{cat.} = 1.85$ g, 1.5 g, 1.0 g and 0.9 g and $T = 210$ °C. The total o/p ratio includes all C_2 - C_4 species.

In these experiments, the syngas flow rate was decreased in order to increase the conversion level, and the resulting higher residence time in the reactor has to be accounted for. Longer residence times gives a higher probability of secondary reactions taking place, which results in higher chain-growth probability and also enhanced degree of re-adsorption and hydrogenation of α -olefins.^[85] The increased formation of CO_2 is likely due to the increased partial pressure of H_2O at higher conversions, leading to a higher potential of re-oxidation of cobalt metal, with following increasing rate of the WGS reaction.

Selectivity variation with simulated high conversions

The effect of simulating high conversions by adding water to the feed is shown in Figure 4.21. The same trends were observed in all experiments, but for illustration the experiment at 210 °C and $H_2/CO = 2.13$ is chosen. The data in the right-hand side plots are consecutive to that of the left-hand plot, however, for visualization of the two effects, the plots are separated.

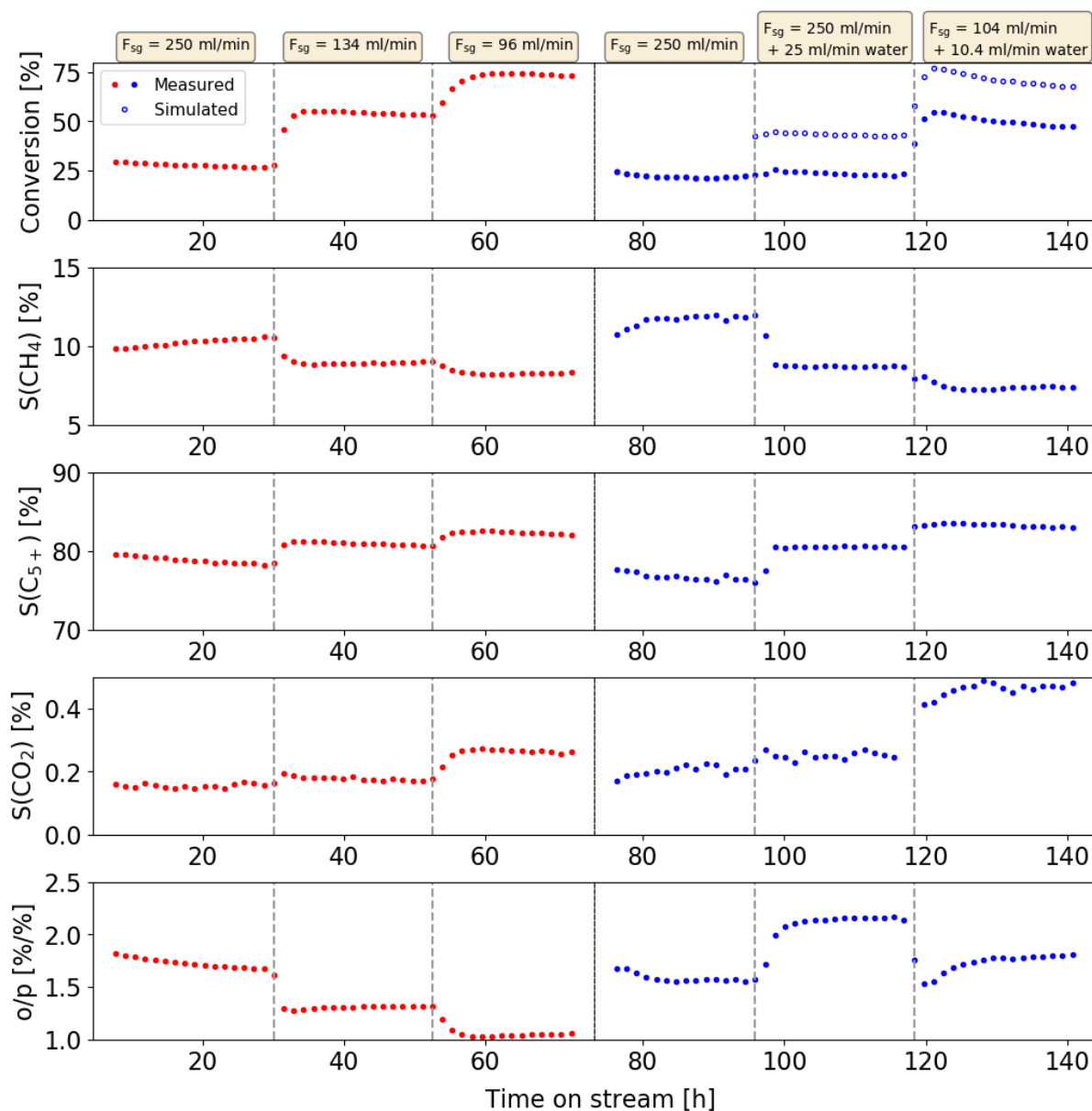


Figure 4.21: The selectivities to key components when ramping the conversion levels by reducing the syngas flow rate (left) and by adding water to the feed (right). The top right plots includes the simulated conversion levels equivalent to the partial pressure of water in the reactor when adding water. Conditions: $H_2/CO = 2.13$, $m_{cat.} = 1.0$ g, $T = 210$ °C. Flow rates of syngas, F_{sg} and water are added above the plot. Outliers have been omitted.

Included in the conversion plot are the simulated conversion levels. These are determined by calculating the conversion level required to produce a partial pressure equivalent to

the sum of partial pressures of added water and indigenous water. Evidently, there are hardly any differences in the selectivity trends for CH_4 , C_{5+} and CO_2 , when comparing the simulated high conversions and the high conversions obtained by lowering the feed flow rate. There is, however, a clear difference in selectivity towards olefins versus paraffins. The same trend is observed for all C_2 - C_4 species, but the sum of these is chosen as representation. As was discussed previously, the probability of secondary reactions taking place, including re-adsorption and hydrogenation of olefins to form paraffins, are highly dependant on the residence time. This is also seen in the olefin-to-paraffin plot in the left-hand side of Figure 4.21. However, when “increasing” the conversion by adding external water to the feed, the residence time is as good as unchanged, and in this case, the olefin-to-paraffin ratio increased. When lowering the feed flow rate whilst feeding water, it is observed that the olefin-to-paraffin decreases. This suggests that the effects of residence time and water addition are two conflicting phenomena, whereas water has an inhibiting effect on secondary hydrogenation of olefins, while the opposite is true for residence time. This is a result of the combined contributions of a lower rate of chain termination via hydrogen addition and a lower rate of secondary hydrogenation reactions.^[85]

It is, however, important to emphasize that the two scenarios are not directly comparable, as the concentration profile of water throughout the reactor is more uniform in the case where external water is fed, whilst in the case where no water is added the concentration of water will be high only near the exit of the reactor. In addition, given the difference in measured conversion, there is also a difference in the composition of reactants in the reactor in the two instances. Nonetheless, it is interesting to compare the two instances, and the activity and selectivities at similar conversion levels (measured versus simulated) are shown in Table 4.10.

Table 4.10: Comparison of catalyst performance at high conversion, measured versus simulated. Conditions: $p_{\text{total}} = 20$ bar in the instance of measured high conversion, and $p_{\text{total}} = 22$ bar (20 bar syngas + 2 bar water) at simulated high conversion, $\text{H}_2/\text{CO} = 2.13$, $T = 210$ °C, $m_{\text{cat.}} = 1.0$ g. The average partial pressure of water in the reactor is 3.65 bar in both instances.

Instance	TOS [h]	Flow rate [mL/min]	Conversion [%]	STY [[$10^2 \times 1/\text{s}$]]	S(CO_2) [%]	S(CH_4) [%]	S(C_{5+}) ^a [%]	o/p ^b [%/%]
Measured	56.7	95.6	70.5	6.3	0.27	8.3	82.6	1.05
Simulated	132.3	103.6 ^c	70.8 (49.9) ^d	4.9	0.45	7.4	83.7	1.77

^a Reported as CO_2 -free, i.e. $S(\text{C}_{5+}) = 100\% - \sum S_{\text{hydrocarbons}}$.

^b Total olefin-to-paraffin ratio for C_2 - C_4 .

^c Plus 10.36 mL/min water.

^d Simulated conversion with measured conversion in parenthesis.

As indicated in the table, the syngas flow rate is quite similar, giving comparable residence times. There are only small differences in selectivities to methane and C_{5+} in the two instances. The difference in selectivity to CO_2 is probably due to a combination of the larger extent of deactivation given the longer time on stream, and that the entire catalyst bed is exposed to the high partial pressure of water (with following higher potential of re-oxidation) in the case of simulated conversion. These two factors may also explain the observed differences (albeit weak) in selectivity to methane and C_{5+} .

Conclusion and Further Work

This research work focused on investigating the effects of reaction conditions on the performance of cobalt-based Fischer-Tropsch catalysts. A 20%Co0.5%Re/ γ -Al₂O₃ catalyst was synthesized by incipient wetness impregnation and both the catalytic properties and the performance was compared to that of a commercial type catalyst with identical formulation procured from Equinor. The characterization results showed only small differences between the two, indicating that the catalysts should exhibit similar performance for Fischer-Tropsch synthesis. However, the experimental results showed both differences in selectivities and robustness towards deactivation. In addition, opposite kinetic responses to the addition of external water were observed, whereas the standard catalyst displayed a negative kinetic effect whilst a positive effect was observed for the commercial type catalyst. The observed differences in performance were suggested due to differences in the synthesis procedure of the two catalysts.

The commercial catalyst was chosen for further investigation and was tested at a variety of reaction conditions, including different temperature levels, a range of feed gas compositions, water addition to the feed, variation in the conversion level, and reaction time. The effects of increased temperature on the selectivities were observed to be strikingly similar to that of the effects of increasing the H₂/CO ratio. This was suggested to be due to the disproportional increase in rate of hydrogenation compared to its competing reactions when the temperature was increased and that the same effect was achieved at conditions with excess hydrogen present. The magnitude of the kinetic response to external water added to the feed was observed to be linked to both the temperature and H₂/CO ratio, hence it was proposed that this is not solely a pore characteristics phenomenon. The rate of deactivation was observed to have a linear dependency on the temperature given the three temperature levels tested here. Although not as consistent, a similar trend was observed for the rate of deactivation versus the H₂/CO ratio. On the other hand, long-term deactivation was observed to follow a negative exponential function. This difference in short-term and long-term deactivation was proposed to be due to the rapid sintering in the early stages of operation, which slows down during the experiments, and that a combination of re-oxidation and coking succeeds sintering at a certain point, causing the long-term deactivation.

Due to the unsatisfactory results of catalyst regeneration, a different procedure which included an oxidation step prior to reduction was proposed.

Based on the observations made during all the experiments in this thesis, a summary of all the reaction conditions and how they influence the FTS are given in Table 5.1.

Table 5.1: Summary of the observed effects of the various conditions.

Parameter	Chain growth	Olefin selectivity	CO ₂ selectivity	CH ₄ selectivity	Rate of deactivation	STY
Temperature	↓	↓	↑	↑	↑	↑
H ₂ /CO ratio	↓	↓	↓	↑	↑	↑
Water addition	↑	↑	↑	↓	↑	*
Conversion	↑	↓	↑	↓	*	*
Reaction time	*	*	↑	↑	↓	↓

^a [↑] Increasing with increasing parameter.

^b [↓] Decreasing with increasing parameter.

^c [*] Inconclusive/minimal effect.

Especially of interest for further work would be to investigate the characteristics of the two catalysts deeper. Given the similar characterization results obtained for the two catalysts and the differences in performance, especially regarding the different kinetic response to the addition of water to the feed, it would be interesting to perform additional characterizations to possibly reveal what caused the differences. Although the average particle size was determined to be similar, it is possible that one of the catalysts had a greater number of small cobalt particles that could cause the effect. Hence, it would be interesting to determine the particle size distribution of the two catalysts by performing scanning electron microscopy (SEM) experiments or similar.

In the instance of significant CO₂ formation, it was proposed that the effect could be due to water-induced re-oxidation of cobalt metal or that the Boudouard reaction becoming important. Hence, it would also be interesting to perform, for instance, *in-situ* X-ray diffraction or *in-situ* magnetic measurements, to reveal whether a significant portion of cobalt oxides are formed and hence is the cause of the phenomenon.

Bibliography

- [1] M. Roser, “Our world in data: Future population growth.” <https://ourworldindata.org/future-population-growth>. [Online accessed; 2019-04-03].
- [2] L. Doman, “EIA projects 28% increase in world energy use by 2040.” <https://www.eia.gov/todayinenergy/detail.php?id=32912>, 2017. [Online; accessed 2019-04-01].
- [3] International Energy Agency, “CO₂ Emissions from Fuel Combustion 2017 - Highlights.” <http://www.indiaenvironmentportal.org.in/files/file/CO2EmissionsfromFuelCombustionHighlights2017.pdf>, 2017. [Online; accessed 2019-04-01].
- [4] E. Rosenberg, K. A. Espegren, E. Holden, O. Wicken, M. Ryghaug, and K. H. Sørensen, “CenSES Energy demand projections towards 2050 - Reference path. A Position Paper prepared by FME CenSES.” https://www.ntnu.no/documents/7414984/1265644753/Position-paper_Energy-Projections_utenbleed.pdf/b39bc144-cff6-46c3-82d9-37b1f8b2e04f. [Online accessed; 2019-04-03].
- [5] G. W. Huber, S. Iborra, and A. Corma, “Synthesis of Transportation Fuels from Biomass: Chemistry, Catalysts, and Engineering,” *Chemical Reviews*, vol. 106, pp. 4044–4098, 2006.
- [6] J. A. Moulijn, M. Makkee, and A. E. van Diepen, *Chemical Process Technology*. John Wiley & Sons, 2. ed., 2013.
- [7] R. C. Baliban, J. A. Elia, and C. A. Floudas, “Biomass to liquid transportation fuels (BTL) systems: process synthesis and global optimization framework,” *Energy Environ. Sci.*, vol. 6, pp. 267–287, 2013.
- [8] H. Bitter, “Chemicals from biobased feedstocks: integration on multiple length scales.” https://www.wur.nl/upload_mm/o/g/f/74af53af-1180-4052-9160-f8d7e740a59e_Oratieboekje_Bitter_final.pdf, 2014. [Online accessed; 2019-04-03].

- [9] R. Edwards, J.-F. Larive, and J.-C. Beziat, "Well-to-wheels Analysis of Future Automotive Fuels and Powertrains in the European Context." <https://publications.europa.eu/en/publication-detail/-/publication/708b39fd-4cc9-4456-9b63-6d1536240202/language-en>, 2011. [Online accessed; 2019-04-03].
- [10] S. S. Ail and S. Dasappa, "Biomass to liquid transportation fuel via Fischer-Tropsch synthesis - Technology review and current scenario," *Renewable and Sustainable Energy Reviews*, vol. 58, pp. 267 – 286, 2016.
- [11] V. S. Sikarwar, Z. Ming, P. S. Fennell, N. Shah, and E. J. Anthonye, "Progress in biofuel production from gasification," *Progress in Energy and Combustion Science*, vol. 61, pp. 189–248, 07. 2017.
- [12] I. Chorkendorff and J. W. Niemantsverdriet, *Concepts of Modern Catalysis and Kinetics*. Wiley-VCH, 2003.
- [13] W. Ma, G. Jacobs, J. Kang, D. E. Sparks, M. K. Gnanamani, V. Pendyala, W. D. Shafer, R. Keogh, U. Graham, G. A. Thomas, B. H. Davis, "Fischer-Tropsch synthesis. Effect of alkali, bicarbonate and chloride addition on activity and selectivity," *Catalysis Today*, vol. 215, March 2013.
- [14] L. Gavrilović, J. Brandin, A. Holmen, H. J. Venvik, R. Myrstad, E. A. Blekkan, "Fischer-Tropsch synthesis - Investigation of the deactivation of a Co catalyst by exposure to aerosol particles of potassium salt," *Applied Catalysis B: Environmental*, vol. 230, pp. 203 – 209, 2018.
- [15] D. E. Sparks, G. Jacobs, M. K. Gnanamani, V. R. R. Pendyala, W. Ma, J. Kang, W. D. Shafer, R. A. Keogh, U. M. Graham, P. Gao, and B. H. Davis, "Poisoning of cobalt catalyst used for Fischer-Tropsch synthesis," *Catalysis Today*, vol. 215, pp. 67–72, oct 2013.
- [16] A. N. Stranges, "A History of the Fischer-Tropsch Synthesis in Germany 1926-45," *Studies in Surface Science and Catalysis*, vol. 163, pp. 1–27, January 2007.
- [17] R. Guettel, U. Kunz, and T. Turek, "Reactors for Fischer-Tropsch Synthesis," *Chemical Engineering & Technology*, vol. 31, pp. 746–754, May 2008.
- [18] E. Rytter and A. Holmen, "Perspectives on the Effect of Water in Cobalt Fischer-Tropsch Synthesis," *ACS Catalysis*, vol. 7, no. 8, pp. 5321–5328, 2017.
- [19] M. Claeys and E. van Steen, "On the effect of water during Fischer-Tropsch synthesis with a ruthenium catalyst," *Catalysis Today*, vol. 71, no. 3, pp. 419 – 427, 2002.
- [20] S. Storsæter, Ø. Borg, E. A. Blekkan, B. Tøtdal, and A. Holmen, "Fischer-Tropsch synthesis over Re-promoted Co supported on Al₂O₃, SiO₂ and TiO₂: Effect of water," *Catalysis Today*, vol. 100, no. 3, pp. 343 – 347, 2005. Catalysis for a Sustainable Future, 11th Nordic Symposium on Catalysis.

-
- [21] S. Storsæter, Ø. Borg, E. A. Blekkan, and A. Holmen, "Study of the effect of water on Fischer-Tropsch synthesis over supported cobalt catalysts," *Journal of Catalysis*, vol. 231, no. 2, pp. 405–419, 2005.
- [22] A.-M. Hilmen, O. A. Lindvåg, E. Bergene, D. Schanke, S. Eri, and A. Holmen, "Selectivity and activity changes upon water addition during Fischer-Tropsch synthesis," in *Studies in Surface Science and Catalysis*, vol. 136, pp. 295–300, Elsevier, 2001.
- [23] E. A. Blekkan, Ø. Borg, V. Frøseth, and A. Holmen, "Fischer-Tropsch synthesis on cobalt catalysts: the effect of water," in *Catalysis: Volume 20*, pp. 13–32, The Royal Society of Chemistry, 2007.
- [24] Ø. Borg, S. Storsæter, S. Eri, H. Wigum, E. Rytter, and A. Holmen, "The Effect of Water on the Activity and Selectivity for γ -Alumina Supported Cobalt Fischer-Tropsch Catalysts with Different Pore Sizes," *Catalysis Letters*, vol. 107, pp. 95–102, feb 2006.
- [25] E. Rytter, Ø. Borg, N. E. Tsakoumis, and A. Holmen, "Water as key to activity and selectivity in Co Fischer-Tropsch synthesis: γ -alumina based structure-performance relationships," *Journal of Catalysis*, vol. 365, pp. 334–343, Sep 2018.
- [26] Ø. Borg, N. Hammer, S. Eri, O. A. Lindvåg, R. Myrstad, E. A. Blekkan, M. Rønning, and A. Holmen, "Fischer-Tropsch synthesis over un-promoted and Re-promoted γ -Al₂O₃ supported cobalt catalysts with different pore sizes," *Catalysis Today*, vol. 142, pp. 70–77, apr 2009.
- [27] G. P. van der Laan and A. A. C. M. Beenackers, "Kinetics and Selectivity of the Fischer-Tropsch Synthesis: A Literature Review," *Catalysis Reviews*, vol. 41, pp. 255–318, jan 1999.
- [28] A. Lillebø, E. Rytter, E. A. Blekkan, and A. Holmen, "Fischer-Tropsch Synthesis at High Conversions on Al₂O₃-Supported Co Catalysts with Different H₂/CO Levels," *Industrial & Engineering Chemistry Research*, vol. 56, no. 45, pp. 13281–13286, 2017.
- [29] E. Rytter, N. E. Tsakoumis, and A. Holmen, "On the selectivity to higher hydrocarbons in Co-based Fischer-Tropsch synthesis," *Catalysis Today*, vol. 261, pp. 3–16, mar 2016.
- [30] A. H. Lillebø, *Conversion of biomass derived synthesis gas into liquid fuels via the Fischer - Tropsch synthesis process: Effect of alkali and alkaline earth metal impurities and CO conversion levels on cobalt based catalysts*. PhD thesis, NTNU, 2014.
- [31] V. R. R. Pendyala, W. D. Shafer, G. Jacobs, and B. H. Davis, "Fischer-Tropsch Synthesis: Effect of Reaction Temperature for Aqueous-Phase Synthesis Over a Platinum Promoted Co/Alumina Catalyst," *Catalysis Letters*, vol. 144, pp. 1088–1095, jun 2014.
-

- [32] M. E. Dry, "Practical and theoretical aspects of the catalytic Fischer-Tropsch process," *Applied Catalysis A: General*, vol. 138, pp. 319–344, may 1996.
- [33] G. Ertl, *Handbook of Heterogeneous Catalysis*. Weinheim; Chichester: Wiley-VHC, 2. ed., 2008.
- [34] N. E. Tsakoumis, M. Rønning, Ø. Borg, E. Rytter, and A. Holmen, "Deactivation of cobalt based Fischer-Tropsch catalysts: A review," *Catalysis Today*, vol. 154, no. 3, pp. 162 – 182, 2010. Eleventh International Symposium on Catalyst Deactivation , Delft(The Netherlands,) October 25-28, 2009.
- [35] D. Schanke, A. M. Hilmen, E. Bergene, K. Kinnari, E. Rytter, E. Ådnanes, and A. Holmen, "Reoxidation and Deactivation of Supported Cobalt Fischer-Tropsch Catalysts," *Energy & Fuels*, vol. 10 (4), 1996.
- [36] E. van Steen, M. Claeys, M. E. Dry, J. van de Loosdrecht, E. L. Viljoen, and J. L. Visagie, "Stability of Nanocrystals: Thermodynamic Analysis of Oxidation and Re-reduction of Cobalt in Water/Hydrogen Mixtures," *The Journal of Physical Chemistry B*, vol. 109(8), 2005.
- [37] B. Davis and M. Occelli, *Advances in Fischer-Tropsch Synthesis, Catalysts, and Catalysis*. Chemical Industries, CRC Press, 2009.
- [38] E. Iglesia, "Design, synthesis, and use of cobalt-based Fischer-Tropsch synthesis catalysts," *Applied Catalysis A: General*, vol. 161, pp. 59–78, nov 1997.
- [39] M. Claeys, M. E. Dry, E. van Steen, P. J. van Berge, S. Booyens, R. Crous, P. van Helden, J. Labuschagne, D. J. Moodley, and A. M. Saib, "Impact of Process Conditions on the Sintering Behavior of an Alumina-Supported Cobalt Fischer-Tropsch Catalyst Studied with an in Situ Magnetometer," *ACS Catalysis*, vol. 5, pp. 841–852, feb 2015.
- [40] M. Sadeqzadeh, S. Chambrey, J. Hong, P. Fongarland, F. Luck, D. Curulla-Ferré, D. Schweich, J. Bousquet, and A. Y. Khodakov, "Effect of Different Reaction Conditions on the Deactivation of Alumina-Supported Cobalt Fischer-Tropsch Catalysts in a Milli-Fixed-Bed Reactor: Experiments and Modeling," *Industrial & Engineering Chemistry Research*, vol. 53, no. 17, pp. 6913–6922, 2014.
- [41] D. Moodley, J. van de Loosdrecht, A. Saib, M. Overett, A. Datye, and J. Niemantsverdriet, "Carbon deposition as a deactivation mechanism of cobalt-based Fischer-Tropsch synthesis catalysts under realistic conditions," *Applied Catalysis A: General*, vol. 354, pp. 102–110, feb 2009.
- [42] A. Saib, D. Moodley, I. Ciobica, M. Hauman, B. Sigwebela, C. Weststrate, J. Niemantsverdriet, and J. van de Loosdrecht, "Fundamental understanding of deactivation and regeneration of cobalt Fischer-Tropsch synthesis catalysts," *Catalysis Today*, vol. 154, pp. 271–282, sep 2010.
- [43] C. K. Rofer-DePoorter, "A comprehensive mechanism for the Fischer-Tropsch synthesis," *Chemical Reviews*, vol. 81, pp. 447–474, Oct 1981.

- [44] J. T. Kummer, T. W. DeWitt, and P. H. Emmett, "Some Mechanism Studies on the Fischer-Tropsch Synthesis Using C^{14} ," *Journal of the American Chemical Society*, vol. 70, pp. 3632–3643, nov 1948.
- [45] B. H. Davis, "Fischer-Tropsch synthesis: current mechanism and futuristic needs," *Fuel Processing Technology*, vol. 71, pp. 157–166, jun 2001.
- [46] L.-M. Tau, H. A. Dabbagh, J. Halasz, and B. H. Davis, "Fischer-Tropsch synthesis: Incorporation of ^{14}C -labeled normal and isoalcohols," *Journal of Molecular Catalysis*, vol. 71, pp. 37–55, Jan 1992.
- [47] H. Pichler and H. Schulz, "Neuere Erkenntnisse auf dem Gebiet der Synthese von Kohlenwasserstoffen aus CO und H_2 ," *Chemie Ingenieur Technik - CIT*, vol. 42, pp. 1162–1174, Sep 1970.
- [48] S. Storsæter, D. Chen, and A. Holmen, "Microkinetic modelling of the formation of C_1 and C_2 products in the Fischer-Tropsch synthesis over cobalt catalysts," *Surface Science*, vol. 600, pp. 2051–2063, May 2006.
- [49] H. Mahmoudi, M. Mahmoudi, O. Doustdar, H. Jahangiri, A. Tsolakis, S. Gu, and M. Lech Wyszynski, "A review of Fischer-Tropsch synthesis process, mechanism, surface chemistry and catalyst formulation," *Biofuels Engineering*, vol. 2, no. 1, pp. 11 – 31, 2017.
- [50] M. Dry, "FT catalysts," *Studies in Surface Science and Catalysis*, vol. 152, pp. 533–600, Jan 2004.
- [51] A. Steynberg, "Introduction to Fischer-Tropsch Technology," *Studies in Surface Science and Catalysis*, vol. 152, pp. 1–63, Jan 2004.
- [52] M. F. M. Post, A. C. Van'T Hoog, J. K. Minderhoud, and S. T. Sie, "Diffusion limitations in Fischer-Tropsch catalysts," *AIChE Journal*, vol. 35, no. 7, pp. 1107–1114, 1989.
- [53] Y.-N. Wang, Y.-Y. Xu, H.-W. Xiang, Y.-W. Li, and B.-J. Zhang, "Modeling of catalyst pellets for Fischer-Tropsch synthesis," *Industrial and Engineering Chemistry Research*, vol. 40, no. 20, pp. 4324–4335, 2001.
- [54] S. Storsæter, B. Tøtdal, J. C. Walmsley, B. S. Tanem, and A. Holmen, "Characterization of alumina-, silica-, and titania-supported cobalt Fischer-Tropsch catalysts," *Journal of Catalysis*, vol. 236, pp. 139–152, Nov 2005.
- [55] E. Rytter and A. Holmen, "On the support in cobalt Fischer-Tropsch synthesis – Emphasis on alumina and aluminates," *Catalysis Today*, vol. 275, pp. 11–19, Oct 2016.
- [56] E. Rytter, Ø. Borg, B. C. Enger, and A. Holmen, " α -alumina as catalyst support in Co Fischer-Tropsch synthesis and the effect of added water; encompassing transient effects," *Journal of Catalysis*, vol. 373, pp. 13–24, May 2019.

- [57] Ø. Borg, S. Eri, E. A. Blekkan, S. Storsæter, H. Wigum, E. Rytter, and A. Holmen, “Fischer-Tropsch synthesis over γ -alumina-supported cobalt catalysts: Effect of support variables,” *Journal of Catalysis*, vol. 248, pp. 89–100, may 2007.
- [58] T. K. Das, G. Jacobs, P. M. Patterson, W. A. Conner, J. Li, and B. H. Davis, “Fischer-Tropsch synthesis: characterization and catalytic properties of rhenium promoted cobalt alumina catalysts,” *Fuel*, vol. 82, pp. 805–815, may 2003.
- [59] F. Diehl and A. Y. Khodakov, “Promotion of Cobalt Fischer-Tropsch Catalysts with Noble Metals: a Review,” *Oil & Gas Science and Technology - Revue de l'IFP*, vol. 64, pp. 11–24, jan 2009.
- [60] A. Steynberg and M. Dry, *Fischer-Tropsch Technology*. Studies in Surface Science and Catalysis, Elsevier Science, 2004.
- [61] M. Ostadi, *New and Innovative Conceptual Designs of Gas-to-Liquid Processes*. PhD thesis, NTNU, 2017.
- [62] B. Jager, “Developments in Fischer-Tropsch technology,” *Studies in Surface Science and Catalysis*, vol. 107, pp. 219–224, Jan 1997.
- [63] J. Regalbuto, *Catalyst Preparation: Science and Engineering*. CRC Press, 1. ed., 2016.
- [64] J. Richardson, *Principles of Catalyst Development*. Fundamental and Applied Catalysis, Springer US, 1. ed., 1989.
- [65] Anton Paar, “X-Ray diffraction (XRD).” <https://wiki.anton-paar.com/en/x-ray-diffraction-xrd/>, 2013. [Online; accessed December 5, 2018].
- [66] M. Vannice, *Kinetics of Catalytic Reactions*. Springer US, 1 ed., 2006.
- [67] P. Somasundaran, *Encyclopedia of Surface and Colloid Science*. Encyclopedia of Surface and Colloid Science, CRC Press, 3. ed., 2015.
- [68] E. P. Barrett, L. G. Joyner, and P. P. Halenda, “The Determination of Pore Volume and Area Distributions in Porous Substances. I. Computations from Nitrogen Isotherms,” *Journal of the American Chemical Society*, vol. 73, pp. 373–380, Jan 1951.
- [69] M. Boudart, “Turnover Rates in Heterogeneous Catalysis,” *Chemical Reviews*, vol. 95, pp. 661–666, May 1995.
- [70] H. S. Fogler, *Elements of Chemical Reaction Engineering*. Pearson, 4. ed., 2014.
- [71] Wikipedia.com, “Gas chromatography.” https://en.wikipedia.org/wiki/Gas_chromatography. [Online accessed; 2019-04-01].
- [72] A. Littlewood, *Gas Chromatography: Principles, Techniques, and Applications*. Elsevier Science, 2. ed., 2013.

-
- [73] J. L. Lemaitre, P. G. Menon, and F. Delannay, *Characterization of Heterogeneous Catalysts*, vol. 15 of *Chemical Industries*, p. 299. New York: M. Dekker, 1984.
- [74] A. Hilmen, D. Schanke, K. Hanssen, and A. Holmen, "Study of the effect of water on alumina supported cobalt Fischer-Tropsch catalysts," *Applied Catalysis A: General*, vol. 186, pp. 169–188, oct 1999.
- [75] D. Schanke, A. M. Hilmen, E. Bergene, K. Kinnari, E. Rytter, E. Ådnes, and A. Holmen, "Study of the deactivation mechanism of Al₂O₃-supported cobalt Fischer-Tropsch catalysts," *Catalysis Letters*, vol. 34, no. 3-4, pp. 269–284, 1995.
- [76] J. Niemantsverdriet, *Spectroscopy in Catalysis: An Introduction*. Wiley, 2000.
- [77] A. M. Hilmen, D. Schanke, and A. Holmen, "TPR study of the mechanism of rhenium promotion of alumina-supported cobalt Fischer-Tropsch catalysts," *Catalysis Letters*, vol. 38, pp. 143–147, Sep 1996.
- [78] I. C. Yates and C. N. Satterfield, "Intrinsic kinetics of the Fischer-Tropsch synthesis on a cobalt catalyst," *Energy & Fuels*, vol. 5, pp. 168–173, jan 1991.
- [79] W. Chu, P. A. Chernavskii, L. Gengembre, G. A. Pankina, P. Fongarland, and A. Y. Khodakov, "Cobalt species in promoted cobalt alumina-supported Fischer-Tropsch catalysts," *Journal of Catalysis*, vol. 252, pp. 215–230, dec 2007.
- [80] W. Zhou, J.-G. Chen, K.-G. Fang, and Y.-H. Sun, "The deactivation of Co/SiO₂ catalyst for Fischer-Tropsch synthesis at different ratios of H₂ to CO," *Fuel Processing Technology*, vol. 87, pp. 609–616, jul 2006.
- [81] G. Jacobs, P. M. Patterson, T. K. Das, M. Luo, and B. H. Davis, "Fischer-Tropsch synthesis: effect of water on Co/Al₂O₃ catalysts and XAFS characterization of reoxidation phenomena," *Applied Catalysis A: General*, vol. 270, pp. 65–76, aug 2004.
- [82] M.-C. Marion and F. Hugues, "Modification of cobalt catalyst selectivity according to Fischer-Tropsch process conditions," *Studies in Surface Science and Catalysis*, vol. 167, pp. 91–96, jan 2007.
- [83] E. Rytter, A. Holmen, E. Rytter, and A. Holmen, "Deactivation and Regeneration of Commercial Type Fischer-Tropsch Co-Catalysts—A Mini-Review," *Catalysts*, vol. 5, pp. 478–499, mar 2015.
- [84] W. Ma, G. Jacobs, Y. Ji, T. Bhatelia, D. B. Bukur, S. Khalid, and B. H. Davis, "Fischer-Tropsch Synthesis: Influence of CO Conversion on Selectivities, H₂/CO Usage Ratios, and Catalyst Stability for a Ru Promoted Co/Al₂O₃ Catalyst Using a Slurry Phase Reactor," *Topics in Catalysis*, vol. 54, pp. 757–767, sep 2011.
- [85] S. Krishnamoorthy, M. Tu, M. P. Ojeda, D. Pinna, and E. Iglesia, "An Investigation of the Effects of Water on Rate and Selectivity for the Fischer-Tropsch Synthesis on Cobalt-Based Catalysts," *Journal of Catalysis*, vol. 211, pp. 422–433, oct 2002.
-

Appendices

Sample Calculations

A.1 Catalyst Synthesis Calculations

The following calculations are based on a catalyst sample containing 25 g support.

The data obtained from the incipient wetness point procedure of the support are shown in Table A.1.

Table A.1: Pore volume of the support.

Support	Mass support [g]	Water [g]	Pore volume [g _{dw} /g _{support}]
γ -Al ₂ O ₃	10.0300	13.1550	1.3116

Mass of cobalt

$$m_{\text{Co}} = \frac{20\%}{80\%} m_{\gamma\text{-Al}_2\text{O}_3} = 6.25\text{g} \quad (\text{A.1})$$

Mass of cobalt nitrate hexahydrate

$$m_{\text{Co}(\text{NO}_3)_2 \cdot 6\text{H}_2\text{O}} = \frac{M_{\text{Co}(\text{NO}_3)_2 \cdot 6\text{H}_2\text{O}}}{M_{\text{Co}}} m_{\text{Co}} = 30.85\text{g} \quad (\text{A.2})$$

Mass of rhenium

$$m_{\text{Re}} = \frac{0.5\%}{80\%} m_{\gamma\text{-Al}_2\text{O}_3} = 0.16\text{g} \quad (\text{A.3})$$

Mass of perrhenic acid ¹

$$m_{\text{HReO}_4} = \frac{M_{\text{HReO}_4}}{M_{\text{Re}}} \frac{100\%}{70\%} m_{\text{Re}} = 0.3\text{g} \quad (\text{A.4})$$

Mass of deionized water

$$m_{\text{dw}} = \text{pore volume} \times m_{\gamma\text{-Al}_2\text{O}_3} = 32.5\text{g} \quad (\text{A.5})$$

¹The mass of rhenium is adjusted with the ratio (100/70) to compensate for the weight percentage of Re in the HReO₄ solution (70 %)

A.2 Calculation of Liquid Flow Rate of Water

The flow rate of syngas:

$$F_{\text{syngas}} = \frac{p_{\text{syngas}}}{p_{\text{total}}} F_{\text{total}} \quad (\text{A.6})$$

where

$$F_{\text{total}} = F_{\text{water(g)}} + F_{\text{syngas}} \quad (\text{A.7})$$

Combining Equations A.6 and A.7:

$$F_{\text{water(g)}} = F_{\text{syngas}} \left(\frac{p_{\text{total}}}{p_{\text{syngas}}} - 1 \right) \quad (\text{A.8})$$

which can be related to the molar flow rate of water via the ideal gas law, shown in Equation A.9.

$$n_{\text{water}} = \frac{F_{\text{water(g)}} p_{\text{ref}}}{R \cdot T_{\text{ref}}} \quad (\text{A.9})$$

The liquid flow rate of water is then calculated:

$$F_{\text{water(l)}} = n_{\text{water}} M_{\text{water}} \quad (\text{A.10})$$

Calculating liquid flow rate of water:

When adding water the first time in the experimental series of steps, the syngas flow rate is $F_{\text{syngas}} = 250\text{mL}/\text{min}$, the wanted total pressure is $p_{\text{total}} = 22\text{bar}$ and the wanted pressure of syngas is $p_{\text{syngas}} = 20\text{bar}$, giving:

$$F_{\text{water(g)}} = 250 \cdot \left(\frac{22}{20} - 1 \right) = 25\text{mL}/\text{min} \quad (\text{A.11})$$

$$\Rightarrow n_{\text{water}} = \frac{25 \cdot 10^{-6} \cdot 1.0 \cdot 10^5}{8.3145 \cdot 298} = 0.001\text{mol}/\text{min} \quad (\text{A.12})$$

$$\Rightarrow F_{\text{water(l)}} = 0.001 \cdot 18.016 = 0.018\text{g}/\text{min} \approx 0.018\text{mL}/\text{min} \quad (\text{A.13})$$

A.3 Calculations of Activity and Selectivities

A.3.1 Experimental Data

Based on the chromatogram shown in Figure A.1, the component selectivities were calculated. The area beneath the curve corresponding to each component was integrated using an Agilent Offline Chemstation, and the results are rendered in Tables A.2 and A.3.

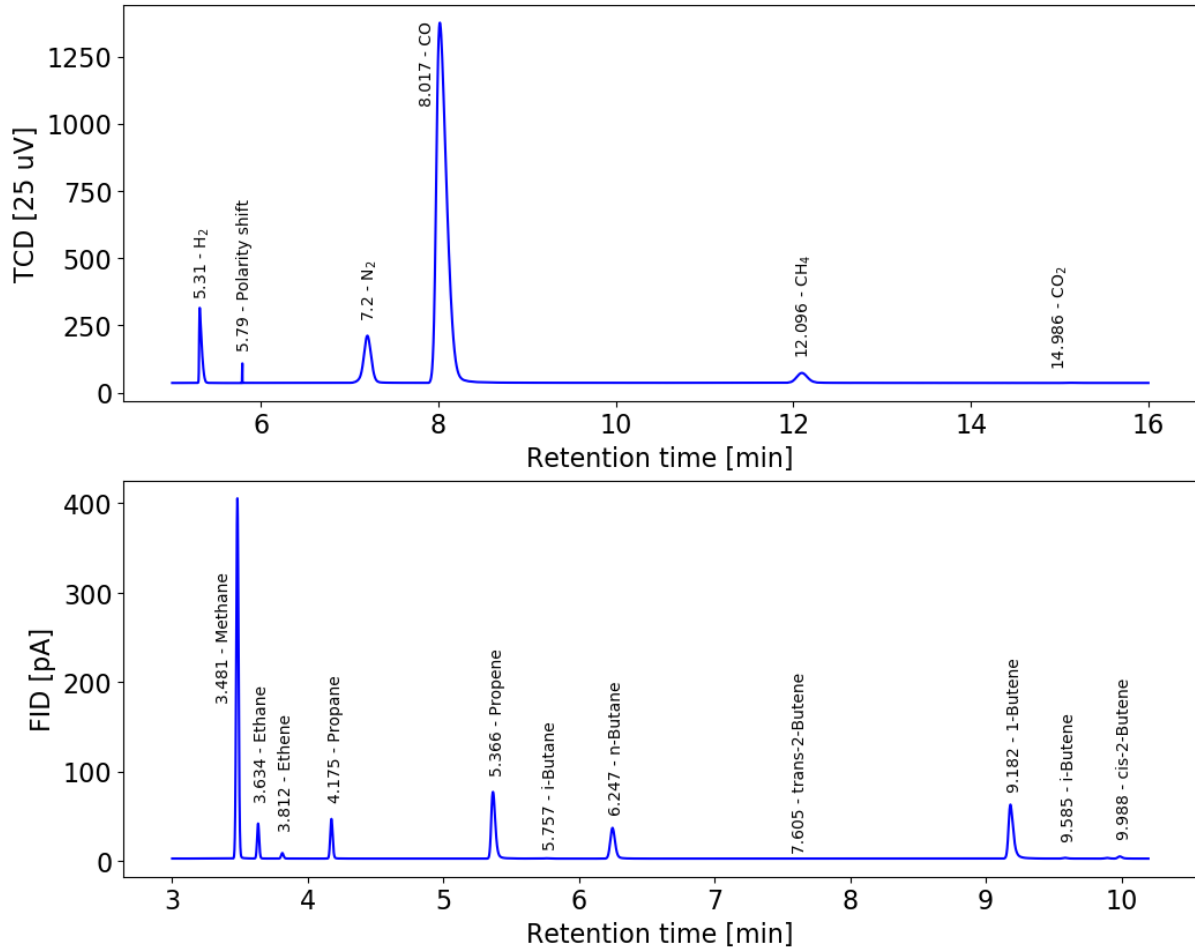


Figure A.1: Chromatogram for the sample calculation.

Table A.2: Experimental TCD data for sample calculations of the activity and selectivities.

Parameter	Value	Unit	Explanation
$A_{H_2}^{TCD}$	704.2	25 uV s	Area of peak of H_2 measured in the sample
$A_{N_2}^{TCD}$	1371.5	25 uV s	Area of peak of N_2 measured in the sample
$A_{CH_4}^{TCD}$	421.0	25 uV s	Area of peak of CH_4 measured in the sample
A_{CO}^{TCD}	14020.7	25 uV s	Area of peak of CO measured in the sample
$A_{CO_2}^{TCD}$	7.65	25 uV s	Area of peak of CO_2 measured in the sample

Table A.3: Experimental FID data for sample calculations of the activity and selectivities.

Parameter	Value	Unit	Explanation
$A_{\text{CH}_4}^{\text{FID}}$	491.9	pA s	Area of peak of methane measured in the sample
$A_{\text{C}_2-}^{\text{FID}}$	43.2	pA s	Area of peak of ethane measured in the sample
$A_{\text{C}_2=}^{\text{FID}}$	7.7	pA s	Area of peak of ethene measured in the sample
$A_{\text{C}_3-}^{\text{FID}}$	57.9	pA s	Area of peak of propane measured in the sample
$A_{\text{C}_3=}^{\text{FID}}$	162.4	pA s	Area of peak of propene measured in the sample
$A_{i-\text{C}_4-}^{\text{FID}}$	0.7	pA s	Area of peak of i-butane measured in the sample
$A_{n-\text{C}_4-}^{\text{FID}}$	87.9	pA s	Area of peak of n-butane measured in the sample
$A_{t-2-\text{C}_4=}^{\text{FID}}$	0.1	pA s	Area of peak of trans-2-butene measured in the sample
$A_{1-\text{C}_4=}^{\text{FID}}$	156.7	pA s	Area of peak of 1-butene measured in the sample
$A_{i-\text{C}_4=}^{\text{FID}}$	2.2	pA s	Area of peak of i-butene measured in the sample
$A_{c-2-\text{C}_4=}^{\text{FID}}$	1.8	pA s	Area of peak of cis-2-butene measured in the sample

Table A.4: Data from the feed gas analysis and the calibration for sample calculations of the activity and selectivities.

Parameter	Value	Unit	Explanation
$A_{\text{N}_2}^{\text{FGA}}$	1017.4	25 uV s	Area of the N_2 peak from feed gas analysis
$A_{\text{CO}}^{\text{FGA}}$	14517.5	25 uV s	Area of the CO peak from feed gas analysis
$A_{\text{N}_2}^{\text{cali}}$	1662.2	25 uV s	Area of the N_2 peak from GC calibration
$A_{\text{CH}_4}^{\text{cali}}$	368.1	25 uV s	Area of the CH_4 peak from GC calibration
$A_{\text{CO}}^{\text{cali}}$	14665.4	25 uV s	Area of the CO peak from GC calibration
$A_{\text{CO}_2}^{\text{cali}}$	452.1	25 uV s	Area of the CO_2 peak from GC calibration
$Y_{\text{N}_2}^{\text{cali}}$	3.0	%	Volume percentage of N_2 in the calibration bottle
$Y_{\text{CH}_4}^{\text{cali}}$	1.0	%	Volume percentage of CH_4 in the calibration bottle
$Y_{\text{CO}}^{\text{cali}}$	30.0	%	Volume percentage of CO in the calibration bottle
$Y_{\text{CO}_2}^{\text{cali}}$	1.0	%	Volume percentage of CO_2 in the calibration bottle

Table A.5: Experimental data for sample calculations of the activity and selectivity.

Parameter	Value	Unit	Explanation
F_{syngas}	250	mL/min	Total flow of syngas in the feed in the example
$m_{\text{cat.}}$	1.0	g	Mass of catalyst
V_{id}	22414	mL/mol	Ideal gas volume
$Y_{\text{N}_2}^{\text{feed}}$	3	%	Percentage of N_2 in the feed (from the bottle)
w_{m}	0.20	-	Weight fraction of Co in the catalyst
D	0.073	-	Dispersion, as measured by H_2 chemisorption

A.3.2 Selectivity Calculations

Response factors:

From the calibration of the GC, relative response factors (relative to N_2) for N_2 , CH_4 , CO and CO_2 were determined from Equation A.14.

$$RRF_{N_2/CH_4/CO/CO_2} = \frac{A_{N_2/CH_4/CO/CO_2}^{cali}/Y_{N_2/CH_4/CO/CO_2}^{cali}}{A_{N_2}^{cali}/Y_{N_2}^{cali}} \quad (A.14)$$

which gives

$$RRF_{N_2} = \frac{1662.2/3.0}{1662.2/3.0} = 1.00 \quad (A.15)$$

$$RRF_{CH_4} = \frac{1662.2/3.0}{368.1/1.0} = 1.50 \quad (A.16)$$

$$RRF_{CO} = \frac{1662.2/3.0}{14665.4/30.0} = 1.13 \quad (A.17)$$

$$RRF_{CO_2} = \frac{1662.2/3.0}{452.1/1.0} = 1.23 \quad (A.18)$$

The relative response factors for C_2 to C_4 species were assumed to correspond to the relative carbon number between the given species and methane, such that

$$RRF_{C_2} = 2 \quad (A.19)$$

$$RRF_{C_3} = 3 \quad (A.20)$$

$$RRF_{C_4} = 4 \quad (A.21)$$

Feed ratio:

From the feed gas analysis by TCD measurements, $A_{N_2}^{FGA}$ and A_{CO}^{FGA} were obtained. The ratio $(A_{CO}/A_{N_2})_{feed}$ was then calculated:

$$(A_{CO}/A_{N_2})_{feed} = \frac{A_{CO}^{FGA}}{A_{N_2}^{FGA}} = \frac{14517.5}{1017.4} = 14.3 \quad (A.22)$$

Composition of the feed gas:

$$Y_{CO}^{feed} = (A_{CO}/A_{N_2})_{feed} RRF_{CO} Y_{N_2}^{feed} = 14.3 \cdot 1.13 \cdot 3\% = 48.5\% \quad (A.23)$$

$$Y_{H_2}^{feed} = 100\% - Y_{N_2}^{feed} - Y_{CO}^{feed} = 100\% - 48.5\% - 3\% = 48.5\% \quad (A.24)$$

Feed flows:

To obtain the desired H_2/CO ratio of 2.13, the syngas was diluted in hydrogen from an external bottle, $F_{H_2,e}$. The component feed flows are shown below.

$$F_{H_2, o} = \frac{F_{\text{syngas}} Y_{H_2}^{\text{feed}}}{100\%} + F_{H_2,e} \quad (\text{A.25})$$

$$= \frac{161.3 \text{ mL/min} \cdot 48.5\%}{100\%} + 88.7 \text{ mL/min} = 166.9 \text{ mL/min}$$

$$F_{CO, o} = \frac{F_{\text{syngas}} Y_{CO}^{\text{feed}}}{100\%} = \frac{161.3 \text{ mL/min} \cdot 48.5\%}{100\%} = 78.2 \text{ mL/min} \quad (\text{A.26})$$

$$F_{N_2, o} = \frac{F_{\text{syngas}} Y_{N_2}^{\text{feed}}}{100\%} = \frac{161.3 \text{ mL/min} \cdot 3\%}{100\%} = 4.9 \text{ mL/min} \quad (\text{A.27})$$

Product flows based on relative responses to N_2 , TCD:

The outlet flow rate of N_2 – which is equal to the inlet flow rate – is converted to the correct units, and the outlet flow rates of CO , CH_4 and CO_2 are calculated based on that.

$$F_{N_2}^{\text{TCD}} = \frac{F_{N_2, o}}{m_{\text{cat}} \cdot V_{\text{id}}} = \frac{4.9 \text{ mL/min} \cdot 60 \text{ min/h}}{1.0 \text{ g} \cdot 22\,414 \text{ mL/mol}} \quad (\text{A.28})$$

$$= 1.3 \cdot 10^{-2} \text{ mol/(g h)}$$

$$F_{CO}^{\text{TCD}} = \frac{F_{N_2}^{\text{TCD}} RRF_{CO} A_{CO}^{\text{TCD}}}{A_{N_2}^{\text{TCD}}} = \frac{0.013 \text{ mol/(g h)} \cdot 1.13 \cdot 14\,020.7}{1371.5} \quad (\text{A.29})$$

$$= 1.5 \cdot 10^{-1} \text{ mol/(g h)}$$

$$F_{CH_4}^{\text{TCD}} = \frac{F_{N_2}^{\text{TCD}} RRF_{CH_4} A_{CH_4}^{\text{TCD}}}{A_{N_2}^{\text{TCD}}} = \frac{0.013 \text{ mol/(g h)} \cdot 1.50 \cdot 421.0}{1371.5} \quad (\text{A.30})$$

$$= 6.0 \cdot 10^{-3} \text{ mol/(g h)}$$

$$F_{CO_2}^{\text{TCD}} = \frac{F_{N_2}^{\text{TCD}} RRF_{CO_2} A_{CO_2}^{\text{TCD}}}{A_{N_2}^{\text{TCD}}} = \frac{0.013 \text{ mol/(g h)} \cdot 1.23 \cdot 7.65}{1371.5} \quad (\text{A.31})$$

$$= 8.9 \cdot 10^{-5} \text{ mol/(g h)}$$

Product flows based on relative responses to CH₄, FID:

The product flows of the hydrocarbons are calculated by intertwining the TCD data and the FID data on basis of methane, as shown below.

$$\begin{aligned}
F_{C_{2-}}^{\text{FID}} &= F_{\text{CH}_4}^{\text{TCD}} \frac{A_{C_{2-}}^{\text{FID}}}{A_{\text{CH}_4}^{\text{FID}} \cdot \text{RRF}_{C_2}} = 6.0 \cdot 10^{-3} \text{ mol}/(\text{g h}) \times \frac{43.2}{491.9 \cdot 2} & (\text{A.32}) \\
&= 2.6 \cdot 10^{-4} \text{ mol}/(\text{g h})
\end{aligned}$$

$$\begin{aligned}
F_{C_{2=}}^{\text{FID}} &= F_{\text{CH}_4}^{\text{TCD}} \frac{A_{C_{2=}}^{\text{FID}}}{A_{\text{CH}_4}^{\text{FID}} \cdot \text{RRF}_{C_2}} = 6.0 \cdot 10^{-3} \text{ mol}/(\text{g h}) \times \frac{7.68}{491.9 \cdot 2} & (\text{A.33}) \\
&= 4.7 \cdot 10^{-5} \text{ mol}/(\text{g h})
\end{aligned}$$

$$\begin{aligned}
F_{C_{3-}}^{\text{FID}} &= F_{\text{CH}_4}^{\text{TCD}} \frac{A_{C_{3-}}^{\text{FID}}}{A_{\text{CH}_4}^{\text{FID}} \cdot \text{RRF}_{C_3}} = 6.0 \cdot 10^{-3} \text{ mol}/(\text{g h}) \times \frac{57.9}{491.9 \cdot 3} & (\text{A.34}) \\
&= 2.4 \cdot 10^{-4} \text{ mol}/(\text{g h})
\end{aligned}$$

$$\begin{aligned}
F_{C_{3=}}^{\text{FID}} &= F_{\text{CH}_4}^{\text{TCD}} \frac{A_{C_{3=}}^{\text{FID}}}{A_{\text{CH}_4}^{\text{FID}} \cdot \text{RRF}_{C_3}} = 6.0 \cdot 10^{-3} \text{ mol}/(\text{g h}) \times \frac{162.4}{491.9 \cdot 3} & (\text{A.35}) \\
&= 6.6 \cdot 10^{-4} \text{ mol}/(\text{g h})
\end{aligned}$$

$$\begin{aligned}
F_{i-C_{4-}}^{\text{FID}} &= F_{\text{CH}_4}^{\text{TCD}} \frac{A_{i-C_{4-}}^{\text{FID}}}{A_{\text{CH}_4}^{\text{FID}} \cdot \text{RRF}_{C_4}} = 6.0 \cdot 10^{-3} \text{ mol}/(\text{g h}) \times \frac{0.7}{491.9 \cdot 4} & (\text{A.36}) \\
&= 2.13 \cdot 10^{-6} \text{ mol}/(\text{g h})
\end{aligned}$$

$$\begin{aligned}
F_{n-C_{4-}}^{\text{FID}} &= F_{\text{CH}_4}^{\text{TCD}} \frac{A_{n-C_{4-}}^{\text{FID}}}{A_{\text{CH}_4}^{\text{FID}} \cdot \text{RRF}_{C_4}} = 6.0 \cdot 10^{-3} \text{ mol}/(\text{g h}) \times \frac{87.9}{491.9 \cdot 4} & (\text{A.37}) \\
&= 2.7 \cdot 10^{-4} \text{ mol}/(\text{g h})
\end{aligned}$$

$$\begin{aligned}
F_{t-2-C_{4=}}^{\text{FID}} &= F_{\text{CH}_4}^{\text{TCD}} \frac{A_{t-2-C_{4=}}^{\text{FID}}}{A_{\text{CH}_4}^{\text{FID}} \cdot \text{RRF}_{C_4}} = 6.0 \cdot 10^{-3} \text{ mol}/(\text{g h}) \times \frac{0.1}{491.9 \cdot 4} & (\text{A.38}) \\
&= 3.0 \cdot 10^{-7} \text{ mol}/(\text{g h})
\end{aligned}$$

$$\begin{aligned}
F_{1-C_{4=}}^{\text{FID}} &= F_{\text{CH}_4}^{\text{TCD}} \frac{A_{1-C_{4=}}^{\text{FID}}}{A_{\text{CH}_4}^{\text{FID}} \cdot \text{RRF}_{C_4}} = 6.0 \cdot 10^{-3} \text{ mol}/(\text{g h}) \times \frac{156.7}{491.9 \cdot 4} & (\text{A.39}) \\
&= 4.8 \cdot 10^{-4} \text{ mol}/(\text{g h})
\end{aligned}$$

$$\begin{aligned}
F_{i-C_4=}^{\text{FID}} &= F_{\text{CH}_4}^{\text{TCD}} \frac{A_{i-C_4=}^{\text{FID}}}{A_{\text{CH}_4}^{\text{FID}} \cdot \text{RRFC}_4} = 6.0 \cdot 10^{-3} \text{ mol}/(\text{g h}) \times \frac{2.2}{491.9 \cdot 4} & (\text{A.40}) \\
&= 6.7 \cdot 10^{-6} \text{ mol}/(\text{g h})
\end{aligned}$$

$$\begin{aligned}
F_{c-2-C_4=}^{\text{FID}} &= F_{\text{CH}_4}^{\text{TCD}} \frac{A_{c-2-C_4=}^{\text{FID}}}{A_{\text{CH}_4}^{\text{FID}} \cdot \text{RRFC}_4} = 6.0 \cdot 10^{-3} \text{ mol}/(\text{g h}) \times \frac{1.8}{491.9 \cdot 4} & (\text{A.41}) \\
&= 5.5 \cdot 10^{-6} \text{ mol}/(\text{g h})
\end{aligned}$$

Conversion of CO:

$$X_{\text{CO}} = 1 - \frac{F_{\text{CO}}}{F_{\text{CO}, o}} = 1 - \frac{F_{\text{CO}}^{\text{TCD}}}{\frac{F_{\text{CO}, o} \cdot 60}{m_{\text{cat.}} \cdot V_{\text{id.}}}} = 1 - \frac{0.150 \text{ mol}/(\text{g h})}{\frac{78.2 \text{ mL}/\text{min} \cdot 60 \text{ min}/\text{h}}{1.0 \text{ g} \cdot 22414 \text{ mL}/\text{mol}}} = 0.28 \quad (\text{A.42})$$

Selectivities:

$$\begin{aligned}
S_{\text{CH}_4} &= \frac{F_{\text{CH}_4}^{\text{TCD}}}{\frac{F_{\text{CO}, o}}{m_{\text{cat.}}} \cdot V_{\text{id.}}} \cdot X_{\text{CO}} \cdot 100 \% = \frac{6.0 \cdot 10^{-3} \text{ mol}/(\text{g h})}{\frac{78.2 \text{ mL}/\text{min} \cdot 60 \text{ min}/\text{h}}{1.0 \text{ g} \cdot 22414 \text{ mL}/\text{mol}}} \cdot 0.28 \cdot 100 \% & (\text{A.43}) \\
&= 10.2 \%
\end{aligned}$$

$$\begin{aligned}
S_{\text{CO}_2} &= \frac{F_{\text{CO}_2}^{\text{TCD}}}{\frac{F_{\text{CO}, o}}{m_{\text{cat.}}} \cdot V_{\text{id.}}} \cdot X_{\text{CO}} \cdot 100 \% = \frac{8.9 \cdot 10^{-5} \text{ mol}/(\text{g h})}{\frac{78.2 \text{ mL}/\text{min} \cdot 60 \text{ min}/\text{h}}{1.0 \text{ g} \cdot 22414 \text{ mL}/\text{mol}}} \cdot 0.28 \cdot 100 \% & (\text{A.44}) \\
&= 0.15 \%
\end{aligned}$$

$$\begin{aligned}
S_{\text{C}_{2-}} &= \frac{F_{\text{C}_{2-}}^{\text{FID}} \cdot \text{RRFC}_2}{\frac{F_{\text{CO}, o}}{m_{\text{cat.}}} \cdot V_{\text{id.}}} \cdot X_{\text{CO}} \cdot 100 \% = \frac{2.6 \cdot 10^{-4} \text{ mol}/(\text{g h}) \cdot 2}{\frac{78.2 \text{ mL}/\text{min} \cdot 60 \text{ min}/\text{h}}{1.0 \text{ g} \cdot 22414 \text{ mL}/\text{mol}}} \cdot 0.28 \cdot 100 \% & (\text{A.45}) \\
&= 0.89 \%
\end{aligned}$$

$$\begin{aligned}
S_{\text{C}_{2=}} &= \frac{F_{\text{C}_{2=}}^{\text{FID}} \cdot \text{RRFC}_2}{\frac{F_{\text{CO}, o}}{m_{\text{cat.}}} \cdot V_{\text{id.}}} \cdot X_{\text{CO}} \cdot 100 \% = \frac{4.7 \cdot 10^{-5} \text{ mol}/(\text{g h}) \cdot 2}{\frac{78.2 \text{ mL}/\text{min} \cdot 60 \text{ min}/\text{h}}{1.0 \text{ g} \cdot 22414 \text{ mL}/\text{mol}}} \cdot 0.28 \cdot 100 \% & (\text{A.46}) \\
&= 0.16 \%
\end{aligned}$$

$$\begin{aligned}
S_{\text{C}_{3-}} &= \frac{F_{\text{C}_{3-}}^{\text{FID}} \cdot \text{RRFC}_3}{\frac{F_{\text{CO}, o}}{m_{\text{cat.}}} \cdot V_{\text{id.}}} \cdot X_{\text{CO}} \cdot 100 \% = \frac{2.4 \cdot 10^{-4} \text{ mol}/(\text{g h}) \cdot 3}{\frac{78.2 \text{ mL}/\text{min} \cdot 60 \text{ min}/\text{h}}{1.0 \text{ g} \cdot 22414 \text{ mL}/\text{mol}}} \cdot 0.28 \cdot 100 \% & (\text{A.47}) \\
&= 1.2 \%
\end{aligned}$$

$$S_{C_3=} = \frac{F_{C_3=}^{\text{FID}} \cdot \text{RRF}_{C_3}}{\frac{F_{\text{CO}_2, \text{o}}}{m_{\text{cat}} \cdot V_{\text{id}}} X_{\text{CO}}} \cdot 100 \% = \frac{6.6 \cdot 10^{-4} \text{ mol}/(\text{g h}) \cdot 3}{\frac{78.2 \text{ mL}/\text{min} \cdot 60 \text{ min}/\text{h}}{1.0 \text{ g} \cdot 22\,414 \text{ mL}/\text{mol}} \cdot 0.28} \cdot 100 \% \quad (\text{A.48})$$

$$= 3.4 \%$$

$$S_{i-C_4-} = \frac{F_{i-C_4-}^{\text{FID}} \cdot \text{RRF}_{C_4}}{\frac{F_{\text{CO}_2, \text{o}}}{m_{\text{cat}} \cdot V_{\text{id}}} X_{\text{CO}}} \cdot 100 \% = \frac{2.13 \cdot 10^{-6} \text{ mol}/(\text{g h}) \cdot 4}{\frac{78.2 \text{ mL}/\text{min} \cdot 60 \text{ min}/\text{h}}{1.0 \text{ g} \cdot 22\,414 \text{ mL}/\text{mol}} \cdot 0.28} \cdot 100 \% \quad (\text{A.49})$$

$$= 0.015 \%$$

$$S_{n-C_4-} = \frac{F_{n-C_4-}^{\text{FID}} \cdot \text{RRF}_{C_4}}{\frac{F_{\text{CO}_2, \text{o}}}{m_{\text{cat}} \cdot V_{\text{id}}} X_{\text{CO}}} \cdot 100 \% = \frac{2.7 \cdot 10^{-4} \text{ mol}/(\text{g h}) \cdot 4}{\frac{78.2 \text{ mL}/\text{min} \cdot 60 \text{ min}/\text{h}}{1.0 \text{ g} \cdot 22\,414 \text{ mL}/\text{mol}} \cdot 0.28} \cdot 100 \% \quad (\text{A.50})$$

$$= 1.8 \%$$

$$S_{t-2-C_4=} = \frac{F_{t-2-C_4=}^{\text{FID}} \cdot \text{RRF}_{C_4}}{\frac{F_{\text{CO}_2, \text{o}}}{m_{\text{cat}} \cdot V_{\text{id}}} X_{\text{CO}}} \cdot 100 \% = \frac{3.0 \cdot 10^{-7} \text{ mol}/(\text{g h}) \cdot 4}{\frac{78.2 \text{ mL}/\text{min} \cdot 60 \text{ min}/\text{h}}{1.0 \text{ g} \cdot 22\,414 \text{ mL}/\text{mol}} \cdot 0.28} \cdot 100 \% \quad (\text{A.51})$$

$$= 0.002 \%$$

$$S_{1-C_4=} = \frac{F_{1-C_4=}^{\text{FID}} \cdot \text{RRF}_{C_4}}{\frac{F_{\text{CO}_2, \text{o}}}{m_{\text{cat}} \cdot V_{\text{id}}} X_{\text{CO}}} \cdot 100 \% = \frac{4.8 \cdot 10^{-4} \text{ mol}/(\text{g h}) \cdot 4}{\frac{78.2 \text{ mL}/\text{min} \cdot 60 \text{ min}/\text{h}}{1.0 \text{ g} \cdot 22\,414 \text{ mL}/\text{mol}} \cdot 0.28} \cdot 100 \% \quad (\text{A.52})$$

$$= 3.28 \%$$

$$S_{i-C_4=} = \frac{F_{i-C_4=}^{\text{FID}} \cdot \text{RRF}_{C_4}}{\frac{F_{\text{CO}_2, \text{o}}}{m_{\text{cat}} \cdot V_{\text{id}}} X_{\text{CO}}} \cdot 100 \% = \frac{6.7 \cdot 10^{-6} \text{ mol}/(\text{g h}) \cdot 4}{\frac{78.2 \text{ mL}/\text{min} \cdot 60 \text{ min}/\text{h}}{1.0 \text{ g} \cdot 22\,414 \text{ mL}/\text{mol}} \cdot 0.28} \cdot 100 \% \quad (\text{A.53})$$

$$= 0.046 \%$$

$$S_{c-2-C_4=} = \frac{F_{c-2-C_4=}^{\text{FID}} \cdot \text{RRF}_{C_4}}{\frac{F_{\text{CO}_2, \text{o}}}{m_{\text{cat}} \cdot V_{\text{id}}} X_{\text{CO}}} \cdot 100 \% = \frac{5.5 \cdot 10^{-6} \text{ mol}/(\text{g h}) \cdot 4}{\frac{78.2 \text{ mL}/\text{min} \cdot 60 \text{ min}/\text{h}}{1.0 \text{ g} \cdot 22\,414 \text{ mL}/\text{mol}} \cdot 0.28} \cdot 100 \% \quad (\text{A.54})$$

$$= 0.038 \%$$

$$S_{C_{5+}} = 100 \% - \sum S_{\text{hydrocarbons}} - S_{\text{CO}_2} = 78.8 \% \quad (\text{A.55})$$

$$S_{C_{5+}, \text{CO}_2 \text{ free}} = 100 \% - \sum S_{\text{hydrocarbons}} = 79.0 \% \quad (\text{A.56})$$

A.3.3 Calculation of Site Time Yield

Given the conversion calculated in the previous section and the data rendered in Table A.5, the STY is calculated as follows.

Site time yield:

$$\begin{aligned} STY &= \frac{F_{CO,0}}{m_{cat.} \cdot V_m} \times \frac{X_{CO} \cdot M_{CO}}{w_m \cdot D} && (A.57) \\ &= \frac{78.2 \text{ mL/min}}{1.0 \text{ g} \cdot 22414 \text{ mL/mol} \cdot 60 \text{ s/min}} \times \frac{0.28 \cdot 58.93 \text{ g/mol}}{0.20 \cdot 0.073} \\ &= 0.066 \text{ s}^{-1} \end{aligned}$$

Additional Experimental Data

B.1 Effect of Reaction Time, 230 °C

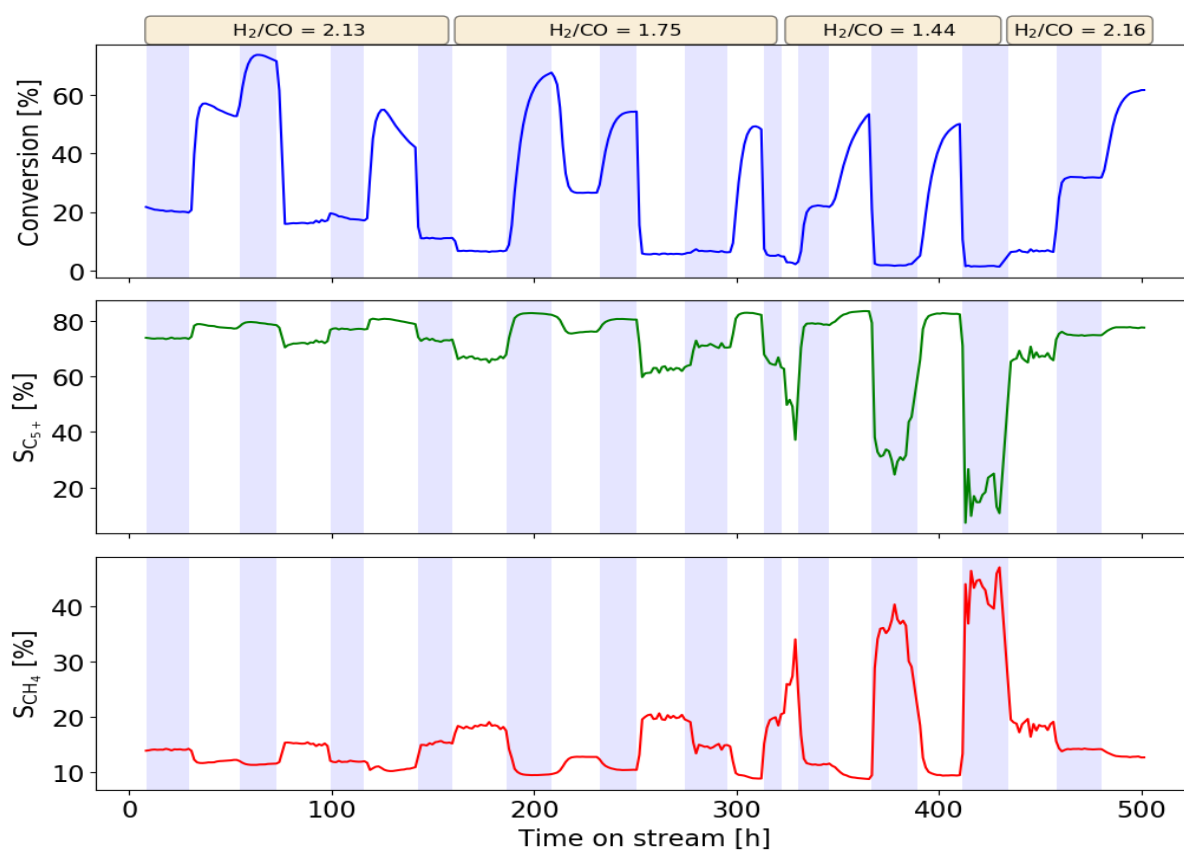


Figure B.1: Activity and selectivity data for the 500 h experiment operated at 230 °C. Conditions: $p_{\text{total}} = 20$ bar with $p_{\text{total}} = 22$ bar when adding water in the feed, $T = 230$ °C, $m_{\text{cat.}} = 0.3$ g, $\text{H}_2/\text{CO}(\text{feed}) = 2.13, 1.75, 1.44$ and 2.16 . CO_2 is included in the C_{5+} fraction. The background shading represents changes in the flow rate. Outliers have been omitted.

Raw Data

C.1 Adsorption/Desorption Curves

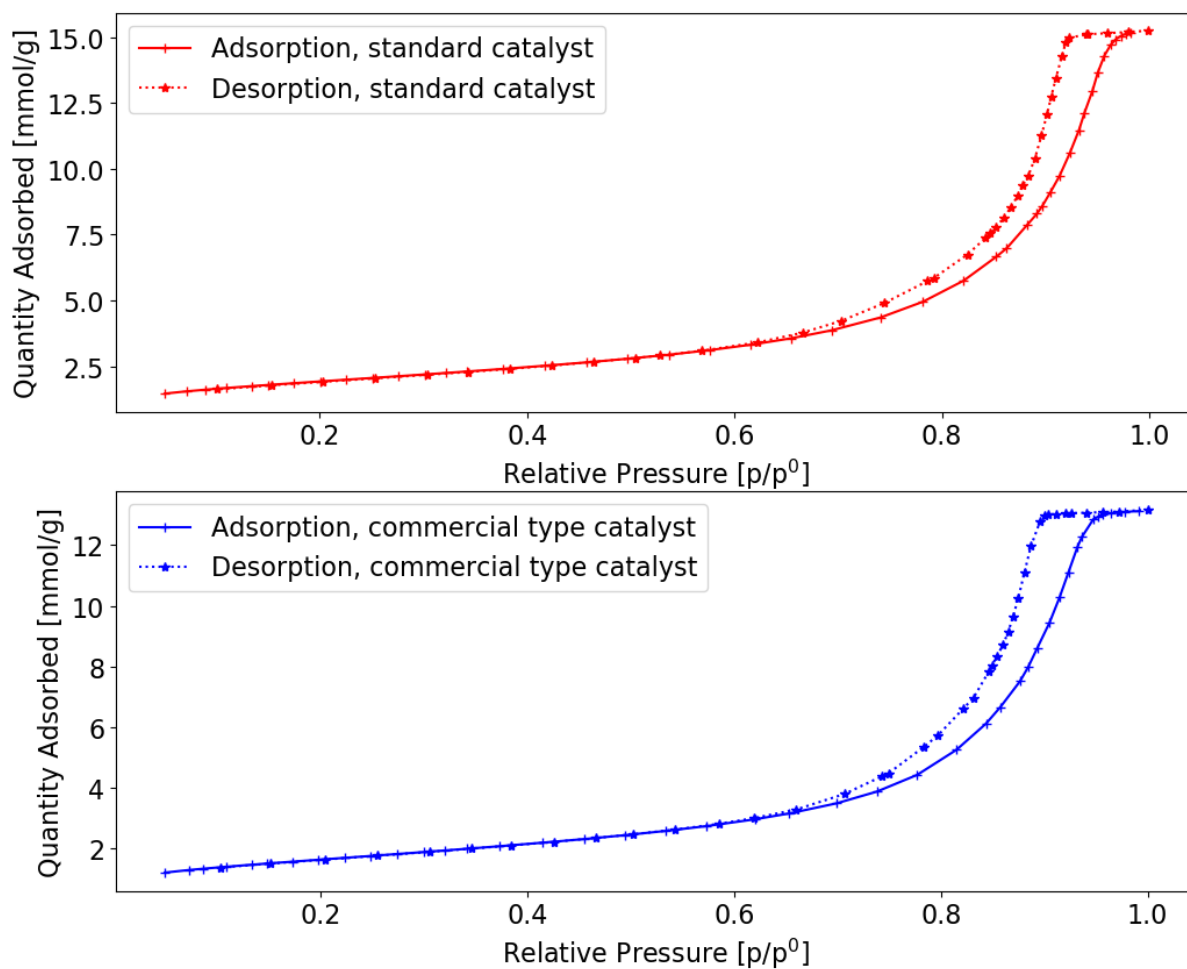


Figure C.1: Adsorption/desorption curves for the catalysts, obtained from N₂ physisorption.

Appendix D

Python Code

D.1 Main Script

```
## Import modules ##
import sys
import pandas as pd
import csv
import os
import codecs
import numpy as np
import matplotlib.pyplot as plt

## Import functions ##
from ftdata import getExpData
from calc import getCalc
from calibration import getCalibration
from feedgas import getFGA

mother = os.getcwd()

## Import the experimental data ##
for dir in os.listdir(mother):
    if 'R1' in dir and 'FT' in dir:
        name = '_Reactor1'
        mcat = 1.0 # [gram]
        tab_fd, tab_tcd, df_fd, df_tcd, titles = getExpData(mother+'\\'+dir, name)

## Import the feed gas analysis ##
for dir in os.listdir(mother):
    if 'AGA' in dir:
        feedratio, ratio, COfeedanal, N2feedanal = getFGA(mother+'\\'+dir)

## Import the relative response factors from the calibration data ##
fN2, fCO, fCH4, fCO2, fC2, fC3, fC4, respN2, respCO, respCH4, respCO2,
N2area, COarea, CH4area, CO2area = getCalibration()

## Calculate the feed gas composition ##
```

```
N2feed = 3 # [%]
COfeed = ratio*N2feed*fCO # [%]
H2feed = 100 - N2feed - COfeed #[-]
print('H2/CO (syngas bottle) = ', H2feed/COfeed) #[-]
print('Feed gas ratio = ', ratio)

## Constants ##
D = 7.3 # [%]

## Make a list of syngas flow rates ##
syngas = []
H2bottleflow = []
waterflow = []
if 'Reactor1' in name:
    for i in range(21):
        syngas.append(161.3)
        H2bottleflow.append(88.7)
        waterflow.append(0)
    for i in range(17):
        syngas.append(86.5)
        H2bottleflow.append(47.5)
        waterflow.append(0)
    for i in range(14):
        syngas.append(61.7)
        H2bottleflow.append(33.9)
        waterflow.append(0)
    for i in range(15):
        syngas.append(161.3)
        H2bottleflow.append(88.7)
        waterflow.append(0)
    for i in range(16):
        syngas.append(161.3)
        H2bottleflow.append(88.7)
        waterflow.append(25)
    for i in range(18):
        syngas.append(66.9)
        H2bottleflow.append(36.7)
        waterflow.append(10.36)
    for i in range(13):
        syngas.append(161.3)
        H2bottleflow.append(88.7)
        waterflow.append(0)

if 'tab_tcd' in locals():
    X, df_plot, df_model = getCalc(syngas, H2bottleflow, H2feed, COfeed,
                                  N2feed, mcat, fN2, fCH4, fCO, fCO2, fC2,
                                  fC3, fC4, tab_tcd, tab_fid, titles, name,
                                  D, waterflow)

    switchtime = []
    switchtime.append(0)
    for i in range(1,len(df_plot['Total feed flow'])):
        if df_plot['Total feed flow'][i] != df_plot['Total feed flow'][i-1]:
```

```

    switchtime.append(i)
    if df_plot['Water flow'][i] != df_plot['Water flow'][i-1]:
        switchtime.append(i)
switchtime.append(len(df_plot['Total feed flow'])-1)
df_plot.to_csv('data' + name + '.csv', sep=',', header = True, index = False)
df_model.to_csv('model_data' + name + '.csv', sep=',', header = True, index = False)

```

D.1.1 Function: Collecting the Experimental Data

```

def getExpData(path, name):
    import pandas as pd
    import csv
    import os
    import codecs
    import numpy as np
    import matplotlib.pyplot as plt

    ## Find adress ##
    mother = path + '\\'
    title = ".join(mother).rpartition("\\")[2]
    csv.register_dialect('gs', delimiter=' ', skipinitialspace=True)
    counter = len(next(os.walk(mother))[1])-1
    titles = []

    retTime_tcd = []
    area_tcd = []
    title_tcd = []
    retTime_fid = []
    area_fid = []
    title_fid = []
    tit_n = []

    ## TCD and FID data. For loop that reads all folders, then all files ##
    for directories in os.listdir(mother):
        if directories[0].startswith('o'):
            working_file = mother+'\\'+directories + '\\Report.txt'
            titles.append(directories)
            with open(working_file, 'r') as f:
                reader = csv.reader(codecs.open(working_file, 'rU', 'utf-16'), 'gs')
                for row in reader:
                    if not row:
                        continue
                    if len(row) >= 3:
                        if any(t == 'METAN' or t == 'Metan' for t in row):
                            if any(t == 'S' or t == 'X' or t == 'T' for t in row):
                                area_fid.append(row[3])
                            else:
                                area_fid.append(row[2])
                                retTime_fid.append(row[0])
                                title_fid.append(titles[-1])
                        if any(t == 'ETAN' or t == 'Etan' for t in row):
                            if any(t == 'S' or t == 'X' or t == 'T' for t in row):
                                area_fid.append(row[3])
                            else:
                                area_fid.append(row[2])

```

```
retTime_fid.append(row[0])
title_fid.append(titles[-1])
if any(t == 'ETEN' or t == 'Eten' for t in row):
    if any(t == 'S' or t == 'X' or t == 'T' for t in row):
        area_fid.append(row[3])
    else:
        area_fid.append(row[2])
        retTime_fid.append(row[0])
        title_fid.append(titles[-1])
if any(t == 'PROPAN' or t == 'Propan' for t in row):
    if any(t == 'S' or t == 'X' or t == 'T' for t in row):
        area_fid.append(row[3])
    else:
        area_fid.append(row[2])
        retTime_fid.append(row[0])
        title_fid.append(titles[-1])
if any(t == 'PROPEN' or t == 'Propen' for t in row):
    if any(t == 'S' or t == 'X' or t == 'T' for t in row):
        area_fid.append(row[3])
    else:
        area_fid.append(row[2])
        retTime_fid.append(row[0])
        title_fid.append(titles[-1])
if any(t == 'i-BUTAN' or t == 'i-Butan' for t in row):
    if any(t == 'S' or t == 'X' or t == 'T' for t in row):
        area_fid.append(row[3])
    else:
        area_fid.append(row[2])
        retTime_fid.append(row[0])
        title_fid.append(titles[-1]) # 'Peaks' since Butan is listed twice in the reorts
if any(t == 'n-BUTAN' or t == 'n-Butan' for t in row)
    and not any(t == 'Peaks' for t in row):
    if any(t == 'S' or t == 'X' or t == 'T' for t in row):
        area_fid.append(row[3])
    else:
        area_fid.append(row[2])
        retTime_fid.append(row[0])
        title_fid.append(titles[-1])
if any(t == 'trans-2-BUTEN' or t == 'trans-2-Buten' for t in row):
    if any(t == 'S' or t == 'X' or t == 'T' for t in row):
        area_fid.append(row[3])
    else:
        area_fid.append(row[2])
        retTime_fid.append(row[0])
        title_fid.append(titles[-1])
if any(t == '1-BUTEN' or t == '1-Buten' or t == '1-BUTAN'
        or t == '1-Butan' for t in row):
    if any(t == 'S' or t == 'X' or t == 'T' for t in row):
        area_fid.append(row[3])
    else:
        area_fid.append(row[2])
        retTime_fid.append(row[0])
        title_fid.append(titles[-1])
if any(t == 'i-BUTEN' or t == 'i-Buten' for t in row):
    if any(t == 'S' or t == 'X' or t == 'T' for t in row):
        area_fid.append(row[3])
```

```

else:
    area_fid.append(row[2])
    retTime_fid.append(row[0])
    title_fid.append(titles[-1])
if any(t == 'cis-2-BUTEN' or t == 'cis-2-Buten' for t in row):
    tit_n.append(titles[-1])
    if any(t == 'S' or t == 'X' or t == 'T' for t in row):
        area_fid.append(row[3])
    else:
        area_fid.append(row[2])
        retTime_fid.append(row[0])
        title_fid.append(titles[-1])
if any(t == 'H2' for t in row):
    area_tcd.append(row[2])
    retTime_tcd.append(row[0])
    title_tcd.append(titles[-1])
if any(t == 'N2' for t in row):
    area_tcd.append(row[2])
    retTime_tcd.append(row[0])
    title_tcd.append(titles[-1])
if any(t == 'CO' for t in row):
    area_tcd.append(row[2])
    retTime_tcd.append(row[0])
    title_tcd.append(titles[-1])
if any(t == 'CH4' for t in row):
    area_tcd.append(row[2])
    retTime_tcd.append(row[0])
    title_tcd.append(titles[-1])
if any(t == 'CO2' for t in row):
    area_tcd.append(row[2])
    retTime_tcd.append(row[0])
    title_tcd.append(titles[-1])

### Treat the TCD and FID data ###
# Set the areas not detected to zero
for i in range(len(area_tcd)):
    if area_tcd[i] == '-':
        area_tcd[i] = 0
    area_tcd[i] = float(area_tcd[i])
for i in range(len(area_fid)):
    if area_fid[i] == '-':
        area_fid[i] = 0
    area_fid[i] = float(area_fid[i])
### Create table of the TCD areas
### Order: [H2, N2, CO, CH4, CO2]
tab_tcd = []
for i in range(5):
    tab_tcd.append([])
    tab_tcd[i] = area_tcd[i::5]
### Create table of the FID areas
### Order: [C1, C2-, C2=, C3-, C3=, i-C4-, n-C4-, t-2-C4=, 1-C4=, i-C4=, c-2-C4=]
tab_fid = []
for i in range(11):
    tab_fid.append([])
    tab_fid[i] = area_fid[i::11]

```

```
for i in range(len(tab_tcd)):
    for j in range(len(tab_tcd[0])):
        if tab_tcd[i][j] == 0:
            tab_tcd[i][j] = 0.1
for i in range(len(tab_fid)):
    for j in range(len(tab_fid[0])):
        if tab_fid[i][j] == 0:
            tab_fid[i][j] = 0.1

### Create DataFrame and print to CSV, ORDER IS DIFFERENT FROM THE TABLES ###
df_fid = pd.DataFrame({'Title':titles, 'Methane':tab_fid[0], 'Ethane':tab_fid[1],
                      'Ethene':tab_fid[2], 'Propane':tab_fid[3], 'Propene':tab_fid[4],
                      'i-Butane':tab_fid[5], 'n-Butane':tab_fid[6], 'trans-2-Butene':tab_fid[7],
                      '1-Butene':tab_fid[8], 'i-Butene':tab_fid[9], 'cis-2-Butene':tab_fid[10]})

df_tcd = pd.DataFrame({'Title':titles, 'H2':tab_tcd[0], 'N2':tab_tcd[1], 'CH4':tab_tcd[3],
                      'CO':tab_tcd[2], 'CO2':tab_tcd[4]})
df_fid.to_csv('FID' + name + '.csv', sep=',', header = True, index = False)
df_tcd.to_csv('TCD' + name + '.csv', sep=',', header = True, index = False)

return(tab_fid, tab_tcd, df_fid, df_tcd, titles)
```

D.1.2 Function: Collecting the Feed Gas Analysis Data

```
def getFGA(args):
    import pandas as pd
    import csv
    import os
    import codecs
    import numpy as np
    import matplotlib.pyplot as plt

    ### Find adress ###
    mother = args + '\\\
title = ".join(mother).rpartition("\\\")[2]
csv.register_dialect('gs', delimiter=' ', skipinitialspace=True)
counter = len(next(os.walk(mother))[1])-1
titles = []

### Import feed gas analysis data ###
datastart = False
numberline = True
N2feedanal = []
COfeedanal = []
feedanaltitles = []
for directories in os.listdir(mother):
    if directories.startswith('FEED'):
        path = mother + '\\\ + directories
        for filename in os.listdir(path):
            if filename[0].startswith('o'):
                working_file = mother+directories+'\\\' +filename + '\\\Report.txt'
                feedanaltitles.append(filename)
                with open(working_file, 'r') as f:
                    reader = csv.reader(codecs.open(working_file, 'rU', 'utf-16'), 'gs')
```

```

for row in reader:
    if not row:
        continue
    if len(row) > 3:
        if row[3] == 'B,':
            datastart = True
        if datastart == True:
            if any(t == 'N2' for t in row):
                N2feedanal.append(float(row[2]))
            if any(t == 'CO' for t in row):
                COfeedanal.append(float(row[2]))
            datastart = False
        else:
            try:
                isinstance(float(row[1]), float)
            except:
                continue
            if abs(float(row[1])-4.7) < 0.2:
                N2feedanal.append(float(row[4]))
            if abs(float(row[1])-6.1) < 0.2:
                COfeedanal.append(float(row[4]))
            datastart = False

# Find the CO/N2 ratios
feedratio = [COfeedanal[i]/N2feedanal[i] for i in range(len(COfeedanal))]

# Take the average of the 4 last measurements
ratio = sum(feedratio[-4:])/len(feedratio[-4:])
Vm = 24789.598 # [ml/mol]

return(feedratio, ratio, COfeedanal, N2feedanal)

```

D.1.3 Function: Collecting the GC Calibration Data

```

def getCalibration():
    import sys
    import pandas as pd
    import csv
    import os
    import codecs
    import numpy as np
    import matplotlib.pyplot as plt

    ## Find adress ##
    mother = 'C:\\Users\\Erik\\OneDrive - NTNU\\MTKJ\\10. Semester\\Python' + '\\'
    title = ".join(mother).rpartition("\\")[2]
    csv.register_dialect('gs', delimiter=',', skipinitialspace=True)
    counter = len(next(os.walk(mother))[1])-1
    titles = []
    N2area = []
    COarea = []
    CH4area = []
    CO2area = []

```

```
## TCD and FID data. For loop that reads all folders, then all files ##
for directories in os.listdir(mother):
    if directories.startswith('Kalibrering'):
        path = mother + '\\\' + directories
        for filename in os.listdir(path):
            if filename[0].startswith('o'):
                working_file = mother+directories+'\\\'+filename + '\\\'Report.txt'
                titles.append(filename)
                with open(working_file, 'r') as f:
                    reader = csv.reader(codecs.open(working_file, 'rU', 'utf-16'), 'gs')
                    for row in reader:
                        if not row:
                            continue
                        if len(row) >= 3:
                            if any(t == 'N2' for t in row):
                                N2area.append(row[2])
                            if any(t == 'CO' for t in row):
                                COarea.append(row[2])
                            if any(t == 'CH4' for t in row):
                                CH4area.append(row[2])
                            if any(t == 'CO2' for t in row):
                                CO2area.append(row[2])
for i in range(len(N2area)):
    if N2area[i] == '-':
        N2area[i] = 0
    N2area[i] = float(N2area[i])/3
    if COarea[i] == '-':
        COarea[i] = 0
    COarea[i] = float(COarea[i])/30
    if CH4area[i] == '-':
        CH4area[i] = 0
    CH4area[i] = float(CH4area[i])/1
    if CO2area[i] == '-':
        CO2area[i] = 0
    CO2area[i] = float(CO2area[i])/1

respN2 = sum(N2area[-4:])/len(N2area[-4:])
respCO = sum(COarea[-4:])/len(COarea[-4:])
respCH4 = sum(CH4area[-4:])/len(CH4area[-4:])
respCO2 = sum(CO2area[-4:])/len(CO2area[-4:])

fN2 = respN2/respN2
fCO = respN2/respCO
fCH4 = respN2/respCH4
fCO2 = respN2/respCO2
fC2 = 2
fC3 = 3
fC4 = 4

return(fN2, fCO, fCH4, fCO2, fC2, fC3, fC4, respN2, respCO, respCH4, respCO2, N2area,
        COarea, CH4area, CO2area)
```


D.1.4 Function: Making All Calculations

```
def getCalc(syngas, H2bottleflow, H2feed, COfeed, N2feed, mcat, fN2, fCH4, fCO,
           fCO2, fC2, fC3, fC4, tab_tcd, tab_fid, titles, name, D, waterflow):

    import pandas as pd
    import matplotlib.pyplot as plt

    ## Feed flows [ml/min] ##
    H2flow = [syngas[i]*H2feed/100 + H2bottleflow[i] for i in range(len(syngas))]
    COflow = [syngas[i]*COfeed/100 for i in range(len(syngas))]
    N2flow = [syngas[i]*N2feed/100 for i in range(len(syngas))]
    feedflowtot = [H2flow[i] + COflow[i] + N2flow[i] for i in range(len(H2flow))]
    H2COtot = [H2flow[i]/COflow[i] for i in range(len(H2flow))]
    print('H2/CO(total) = ', (sum(H2flow)/len(H2flow))/(sum(COflow)/len(COflow)))

    ## Time on stream ##
    if '1' in name:
        TOS = [42/60*(2*i+1) for i in range(len(syngas))] # [h]
    elif '2' in name:
        TOS = [42/60*(2*i+2) for i in range(len(syngas))] # [h]

    ## Constants ##
    Vm = 22414 # [ml/mol]
    MCo = 58.93319 # [g/mol]
    Xm = 20 # [%]

    ## Product flows [mol/g*h] ## tab_tcd: H2 & N2 & CO & CH4 & CO2
    N2flowprod = [(N2flow[i]*60.0/(mcat*Vm)) for i in range(len(N2flow))]
    CH4flowprod = [N2flowprod[i]*fCH4*tab_tcd[3][i]/tab_tcd[1][i]
                   for i in range(len(N2flowprod))]
    COflowprod = [N2flowprod[i]*fCO*tab_tcd[2][i]/tab_tcd[1][i]
                  for i in range(len(N2flowprod))]
    CH4flowprod = [N2flowprod[i]*fCH4*tab_tcd[3][i]/tab_tcd[1][i]
                   for i in range(len(N2flowprod))]
    CO2flowprod = [N2flowprod[i]*fCO2*tab_tcd[4][i]/tab_tcd[1][i]
                   for i in range(len(N2flowprod))]
    etanflowprod = [CH4flowprod[i]*tab_fid[1][i]/(tab_fid[0][i]*fC2)
                    for i in range(len(CH4flowprod))]
    etenflowprod = [CH4flowprod[i]*tab_fid[2][i]/(tab_fid[0][i]*fC2)
                    for i in range(len(CH4flowprod))]
    propanflowprod = [CH4flowprod[i]*tab_fid[3][i]/(tab_fid[0][i]*fC3)
                      for i in range(len(CH4flowprod))]
    propenflowprod = [CH4flowprod[i]*tab_fid[4][i]/(tab_fid[0][i]*fC3)
                      for i in range(len(CH4flowprod))]
    ibutanflowprod = [CH4flowprod[i]*tab_fid[5][i]/(tab_fid[0][i]*fC4)
                      for i in range(len(CH4flowprod))]
    nbutanflowprod = [CH4flowprod[i]*tab_fid[6][i]/(tab_fid[0][i]*fC4)
                      for i in range(len(CH4flowprod))]
    t2butenflowprod = [CH4flowprod[i]*tab_fid[7][i]/(tab_fid[0][i]*fC4)
                       for i in range(len(CH4flowprod))]
    onebutenflowprod = [CH4flowprod[i]*tab_fid[8][i]/(tab_fid[0][i]*fC4)
                        for i in range(len(CH4flowprod))]
    ibutenflowprod = [CH4flowprod[i]*tab_fid[9][i]/(tab_fid[0][i]*fC4)
                      for i in range(len(CH4flowprod))]
```

```

cis2butenflowprod = [CH4flowprod[i]*tab_fid[10][i]/(tab_fid[0][i]*fC4)
                    for i in range(len(CH4flowprod))]

## Conversion ##
X = [(COflow[i]*60.0/(mcat*Vm)-COflowprod[i])/(COflow[i]*60.0/(mcat*Vm))
     for i in range(len(COflow))] #[-]
STY = [(COflow[i]*X[i]*60/mcat)*MCo/(Vm*3600*Xm/100*D/100)
       for i in range(len(COflow))] # [s^-1]
GHSV = [(COflow[i]*X[i]*60/mcat) for i in range(len(COflow))] # [mL/(gcat*h)]
rCO = [COflow[i]*X[i]/(mcat*60*Vm) for i in range(len(COflow))] # [mol/(gcat*s)]

## Selectivity ##
SCH4 = [CH4flowprod[i]*100/(COflow[i]*60*X[i]/(mcat*Vm))
        for i in range(len(CH4flowprod))] # [%]
SCO2 = [CO2flowprod[i]*100/(COflow[i]*60*X[i]/(mcat*Vm))
        for i in range(len(CO2flowprod))] # [%]
Setan = [etanflowprod[i]*fC2*100/(COflow[i]*60.0*X[i]/(mcat*Vm))
         for i in range(len(etanflowprod))] # [%]
Seten = [etenflowprod[i]*fC2*100/(COflow[i]*60.0*X[i]/(mcat*Vm))
         for i in range(len(etenflowprod))] # [%]
Spropan = [propanflowprod[i]*fC3*100/(COflow[i]*60.0*X[i]/(mcat*Vm))
           for i in range(len(propanflowprod))] # [%]
Spropen = [propenflowprod[i]*fC3*100/(COflow[i]*60.0*X[i]/(mcat*Vm))
           for i in range(len(propenflowprod))] # [%]
Sibutan = [ibutanflowprod[i]*fC4*100/(COflow[i]*60.0*X[i]/(mcat*Vm))
           for i in range(len(ibutanflowprod))] # [%]
Snbutan = [nbutanflowprod[i]*fC4*100/(COflow[i]*60.0*X[i]/(mcat*Vm))
           for i in range(len(nbutanflowprod))] # [%]
St2buten = [t2butenflowprod[i]*fC4*100/(COflow[i]*60.0*X[i]/(mcat*Vm))
            for i in range(len(t2butenflowprod))] # [%]
Sonebuten = [onebutenflowprod[i]*fC4*100/(COflow[i]*60.0*X[i]/(mcat*Vm))
            for i in range(len(onebutenflowprod))] # [%]
Sibuten = [ibutenflowprod[i]*fC4*100/(COflow[i]*60.0*X[i]/(mcat*Vm))
           for i in range(len(ibutenflowprod))] # [%]
Scis2buten = [cis2butenflowprod[i]*fC4*100/(COflow[i]*60.0*X[i]/(mcat*Vm))
              for i in range(len(cis2butenflowprod))] # [%]
SC5plus = [100 - (SCH4[i] + SCO2[i] + Setan[i] + Spropan[i] + Spropen[i]
                + Sibutan[i] + Snbutan[i] + St2buten[i] + Sonebuten[i] + Sibuten[i]
                + Scis2buten[i]) for i in range(len(SCH4))] # [%]
SC5plusCO2free = [SC5plus[i]*100/(100-SCO2[i]) for i in range(len(SC5plus))] # [%]
SC2olefins = Seten
SC2paraffins = Setan
SC3olefins = Spropen
SC3paraffins = Spropan
SC4olefins = [St2buten[i]+Sonebuten[i]+Sibuten[i]+Scis2buten[i]
              for i in range(len(St2buten))]
SC4paraffins = [Sibutan[i] + Snbutan[i] for i in range(len(Sibutan))]
Solefins = [SC2olefins[i] + SC3olefins[i] + SC4olefins[i]
            for i in range(len(SC2olefins))]
Sparaffins = [SC2paraffins[i] + SC3paraffins[i] + SC4paraffins[i]
              for i in range(len(SC2paraffins))]
C2op = [SC2olefins[i]/SC2paraffins[i] for i in range(len(SC2olefins))]
C3op = [SC3olefins[i]/SC3paraffins[i] for i in range(len(SC3olefins))]

```

```

C4op = [SC4olefins[i]/SC4paraffins[i] for i in range(len(SC4olefins))]
op = [(SC2olefins[i] + SC3olefins[i] + SC4olefins[i])/(SC2paraffins[i] + SC3paraffins[i]
+ SC4paraffins[i]) for i in range(len(SC2olefins))]

# Usage ratio of H2/CO: CH4, C2-,C2=,C3-,C3=,C4-,C4=,C5+
if 'waterflow' in locals():
    Uratios = [3.0, 2.5, 2.0, 2.33, 2.0, 2.25, 2.0, 2.05]
    UH2CO = [(SCH4[i]*Uratios[0]+Setan[i]*Uratios[1]+Seten[i]*Uratios[2]
+ Spropan[i]*Uratios[3]+Spropen[i]*Uratios[4]+
(Sibutan[i]+Snbutan[i])*Uratios[5]
+(St2buten[i]+Sonebuten[i]+Sibuten[i]+Scis2buten[i])*Uratios[6]
+ SC5plus[i]*Uratios[7] - SCO2[i])/100 for i in range(len(SCH4))]
    XH2 = [COflow[i]*X[i]*UH2CO[i]/H2flow[i] for i in range(len(COflow))] # [%]
    H2ex = [H2flow[i]*(1.0-XH2[i]) for i in range(len(H2flow))] # [ml/min]
    COex = [COflow[i]*(1.0-X[i]) for i in range(len(COflow))] # [ml/min]
    CO2ex = [CO2flowprod[i]*Vm*mcats/60 for i in range(len(CO2flowprod))] # [ml/min]
    CH4ex = [CH4flowprod[i]*Vm*mcats/60 for i in range(len(CH4flowprod))] # [ml/min]
    C2ex = [(etanflowprod[i]+etenflowprod[i])*Vm*mcats/60
for i in range(len(CO2flowprod))] # [ml/min]
    C3ex = [(propanflowprod[i]+propenflowprod[i])*Vm*mcats/60
for i in range(len(CO2flowprod))] # [ml/min]
    C4ex = [(ibutanflowprod[i]+nbutanflowprod[i]+t2butenflowprod[i]
+onebutenflowprod[i]+ibutenflowprod[i]
+cis2butenflowprod[i])*Vm*mcats/60 for i in range(len(CO2flowprod))] # [ml/min]
    C5plusex = [COflow[i]*X[i]*SC5plus[i]/100/5 for i in range(len(COflow))] # [ml/min]

pH2O = []
H2Oex = []
for i in range(len(waterflow)):
    H2Oex.append((COflow[i]*60/(Vm*mcats)-COflowprod[i]-
2*CO2flowprod[i])*mcats*Vm/60 + waterflow[i]) # [ml/min]
    if waterflow[i] != 0:
        pH2O.append(H2Oex[i]*22/(H2ex[i]+COex[i]+CO2ex[i]+CH4ex[i]
+C2ex[i]+C3ex[i]+C4ex[i]+H2Oex[i]+C5plusex[i])) # [bar]
    else:
        pH2O.append(H2Oex[i]*20/(H2ex[i]+COex[i]+CO2ex[i]+CH4ex[i]
+C2ex[i]+C3ex[i]+C4ex[i]+H2Oex[i] + C5plusex[i])) # [bar]

pH2 = []
pCO = []
pCO2 = []
pCH4 = []
pC2 = []
pC3 = []
pC4 = []
pC5plus = []
for i in range(len(waterflow)):
    if waterflow[i] != 0:
        pH2.append(H2ex[i]*22/(H2ex[i]+COex[i]+CO2ex[i]+CH4ex[i]+C2ex[i]+
C3ex[i]+C4ex[i]+H2Oex[i] + C5plusex[i])) # [bar]
        pCO.append(COex[i]*22/(H2ex[i]+COex[i]+CO2ex[i]+CH4ex[i]+C2ex[i]+
C3ex[i]+C4ex[i]+H2Oex[i] + C5plusex[i])) # [bar]
        pCO2.append(CO2ex[i]*22/(H2ex[i]+COex[i]+CO2ex[i]+CH4ex[i]+C2ex[i]+
C3ex[i]+C4ex[i]+H2Oex[i] + C5plusex[i])) # [bar]
        pCH4.append(CH4ex[i]*22/(H2ex[i]+COex[i]+CO2ex[i]+CH4ex[i]+C2ex[i]+
C3ex[i]+C4ex[i]+H2Oex[i] + C5plusex[i])) # [bar]

```

```

pC2.append(C2ex[i]*22/(H2ex[i]+COex[i]+CO2ex[i]+CH4ex[i]+C2ex[i]+
C3ex[i]+C4ex[i]+H2Oex[i] + C5plusex[i])) # [bar]
pC3.append(C3ex[i]*22/(H2ex[i]+COex[i]+CO2ex[i]+CH4ex[i]+C2ex[i]+
C3ex[i]+C4ex[i]+H2Oex[i] + C5plusex[i])) # [bar]
pC4.append(C4ex[i]*22/(H2ex[i]+COex[i]+CO2ex[i]+CH4ex[i]+C2ex[i]+
C3ex[i]+C4ex[i]+H2Oex[i] + C5plusex[i])) # [bar]
pC5plus.append(C5plusex[i]*22/(H2ex[i]+COex[i]+CO2ex[i]+CH4ex[i]+
C2ex[i]+C3ex[i]+C4ex[i]+H2Oex[i] + C5plusex[i])) # [bar]
else:
pH2.append(H2ex[i]*20/(H2ex[i]+COex[i]+CO2ex[i]+CH4ex[i]+
C2ex[i]+C3ex[i]+C4ex[i]+H2Oex[i] + C5plusex[i])) # [bar]
pCO.append(COex[i]*20/(H2ex[i]+COex[i]+CO2ex[i]+CH4ex[i]+
C2ex[i]+C3ex[i]+C4ex[i]+H2Oex[i] + C5plusex[i])) # [bar]
pCO2.append(CO2ex[i]*20/(H2ex[i]+COex[i]+CO2ex[i]+CH4ex[i]+
C2ex[i]+C3ex[i]+C4ex[i]+H2Oex[i] + C5plusex[i])) # [bar]
pCH4.append(CH4ex[i]*20/(H2ex[i]+COex[i]+CO2ex[i]+CH4ex[i]+
C2ex[i]+C3ex[i]+C4ex[i]+H2Oex[i] + C5plusex[i])) # [bar]
pC2.append(C2ex[i]*20/(H2ex[i]+COex[i]+CO2ex[i]+CH4ex[i]+
C2ex[i]+C3ex[i]+C4ex[i]+H2Oex[i] + C5plusex[i])) # [bar]
pC3.append(C3ex[i]*20/(H2ex[i]+COex[i]+CO2ex[i]+CH4ex[i]+
C2ex[i]+C3ex[i]+C4ex[i]+H2Oex[i] + C5plusex[i])) # [bar]
pC4.append(C4ex[i]*20/(H2ex[i]+COex[i]+CO2ex[i]+CH4ex[i]+
C2ex[i]+C3ex[i]+C4ex[i]+H2Oex[i] + C5plusex[i])) # [bar]
pC5plus.append(C5plusex[i]*20/(H2ex[i]+COex[i]+CO2ex[i]+
CH4ex[i]+C2ex[i]+C3ex[i]+C4ex[i]+H2Oex[i] + C5plusex[i])) # [bar]

sum_p = [pH2[i]+pCO[i]+pH2O[i] + pCO2[i] + pCH4[i] + pC2[i] + pC3[i]
+ pC4[i] + pC5plus[i] for i in range(len(pH2))] # [bar]

pH2av = [(pH2[i]+H2flow[i]*20/(H2flow[i]+COflow[i]+N2flow[i]))/2
for i in range(len(pH2))] # [bar]
pCOav = [(pCO[i]+COflow[i]*20/(H2flow[i]+COflow[i]+N2flow[i]))/2
for i in range(len(pH2))] # [bar]
pH2Oav = [(pH2O[i]+2)/2 for i in range(len(pH2O))] # [bar]
sum_pav = [pH2av[i]+pCOav[i]+pH2Oav[i] for i in range(len(pH2av))] # [bar]

rHC_C1 = [COflowprod[i]*SCH4[i]*16/100 for i in range(len(SCH4))] # [g/g*h]
rHC_C2 = [COflowprod[i]*(Setan[i]*15+Seten[i]*14)/100
for i in range(len(Setan))] # [g/g*h]
rHC_C3 = [COflowprod[i]*(Spropan[i]*14.67+Spropan[i]*14)/100
for i in range(len(Spropan))] # [g/g*h]
rHC_C4 = [COflowprod[i]*((Sibutan[i]+Snbutan[i])*14.5+
(St2buten[i]+Sonebuten[i]+Scis2buten[i])*14)/100
for i in range(len(Sibutan))] # [g/g*h]
rHC_C5plus = [COflowprod[i]*SC5plus[i]*14/100 for i in range(len(SC5plus))] # [g/g*h]
rHC_tot = [rHC_C1[i]+rHC_C2[i]+rHC_C3[i]+rHC_C4[i]+rHC_C5plus[i]
for i in range(len(rHC_C1))] # [g/g*h]

df_model = pd.DataFrame({'Usage ratio':UH2CO, 'XCO':X, 'XH2':XH2,
'H2 exit flow':H2ex,'CO exit flow':COex,'CO2 exit flow':CO2ex,
'CH4 exit flow':CH4ex,'C2 exit flow':C2ex, 'C3 exit flow':C3ex,
'C4 exit flow':C4ex,'C5+ exit flow':C5plusex, 'H2O exit flow':H2Oex,
'pH2':pH2,'pCO':pCO, 'pCO2':pCO2, 'pCH4':pCH4, 'pC2':pC2, 'pC3':pC3,
'pC4':pC4, 'pC5plus':pC5plus, 'pH2O':pH2O, 'sum_p':sum_p, 'pH2av':pH2av,
'pCOav':pCOav, 'pH2Oav':pH2Oav, 'Sum Pav':sum_pav, 'rHC_C1':rHC_C1,
'rHC_C2':rHC_C2,'rHC_C3':rHC_C3,'rHC_C4':rHC_C4,'rHC_C5plus':rHC_C5plus,

```

```
'rHC_tot':rHC_tot})

## Create a matrix of key values for plotting ##
df_plot = pd.DataFrame({'Titles':titles, 'TOS':TOS, 'X':X, 'STY':STY, 'GHSV':GHSV,
  'rCO':rCO, 'H2/CO':H2COtot, 'Total feed flow':feedflowtot, 'Water flow':waterflow,
  'SCH4':SCH4, 'SCO2':SCO2, 'S ethane':Setan, 'S ethene':Seten, 'S propane':Spropan,
  'S propene':Spropen, 'S i-butane':Sibutan, 'S n-butane':Snbutan,
  'S trans-2-butene':St2buten, 'S 1-butene':Sonebuten, 'S i-butene':Sibuten,
  'S cis-2-butene':Scis2buten, 'SC5plus':SC5plus, 'SC5plusCO2free':SC5plusCO2free,
  'S C2 olefins':SC2olefins, 'S C2 paraffins':SC2paraffins, 'S C3 olefins':SC3olefins,
  'S C3 paraffins':SC3paraffins, 'S C4 olefins':SC4olefins, 'S C4 paraffins':SC4paraffins,
  'SC2op':C2op, 'SC3op':C3op, 'SC4op':C4op, 'op':op, 'Usage ratio':UH2CO, 'XCO':X,
  'XH2':XH2, 'H2 exit flow':H2ex, 'CO exit flow':COex, 'CO2 exit flow':CO2ex,
  'CH4 exit flow':CH4ex, 'C2 exit flow':C2ex, 'C3 exit flow':C3ex, 'C4 exit flow':C4ex,
  'C5+ exit flow':C5plusex, 'H2O exit flow':H2Oex, 'pH2':pH2, 'pCO':pCO, 'pCO2':pCO2,
  'pCH4':pCH4, 'pC2':pC2, 'pC3':pC3, 'pC4':pC4, 'pC5plus':pC5plus, 'pH2O':pH2O,
  'sum_p':sum_p, 'pH2av':pH2av, 'pCOav':pCOav, 'pH2Oav':pH2Oav, 'Sum Pav':sum_pav,
  'rHC_C1':rHC_C1, 'rHC_C2':rHC_C2, 'rHC_C3':rHC_C3, 'rHC_C4':rHC_C4,
  'rHC_C5plus':rHC_C5plus, 'rHC_tot':rHC_tot})

return(X, df_plot, df_model)
```


Risk Assessment

ID	29644	Status	Dato
Risikoområde	Risikovurdering: Helse, miljø og sikkerhet (HMS)	Opprettet	06.09.2018
Opprettet av	Erik Andreas Jørgensen	Vurdering startet	06.09.2018
Ansvarlig	Edd Anders Blekkan	Tiltak besluttet	
		Avsluttet	

Risikovurdering: CAT, 2018, Erik Andreas Jørgensen

Gyldig i perioden:
9/6/2018 - 9/6/2021

Sted:
Chemistry Hall D, K5

Mål / hensikt

- Synthesis of a CoRe /Al₂O₃ catalyst
- Synthesis of a CoRe /TiO₂ catalyst
- Calcination of the catalysts and support
- Operation of a Fischer-Tropsch rig
- Characterization of catalyst

Bakgrunn
Experimental work involving synthesis and characterization of the catalysts and operation of a Fischer-Tropsch rig.

Beskrivelse og avgrensninger
Catalyst synthesis using Alumina, Cobalt Nitrate Hexahydrate and Perrhenic Acid. The alumina is pre-dried in a heating cabinet prior to mixing and the mixture is also dried. The heating cabinet operates at 110 C. The catalyst is then calcined at 300 C for 16 h.

Catalyst synthesis using Titania, Cobalt Nitrate Hexahydrate and Perrhenic Acid. The Titania is pre-calcined in the calcination oven prior to mixing at 700 C for 10h. The mixture is then dried in a heating cabinet which operates at 110 C and the catalyst is calcined at 700 C for 10 h.

In situ catalyst reduction: Hydrogen flow of 250 mL/min through the reactor at 350 C for 16 h.

Operation of the Fischer-Tropsch rig involves use of pressurized, flammable and toxic gases (He, H₂ and CO) and handling of hot liquid products (mostly water and wax). The work related to the FTS operation includes preparation of operation, loading the catalyst into the reactor followed by mounting of the reactor to the rig, pressurizing, leak testing, adjusting operating conditions (temperature, gas flow rates, pressure), emptying the product containers and changing gas bottles. The operation will be continuously performed over long periods (weeks), and thus may require after hours work, however the work involving risks (changing gas bottles etc.) will be arranged to take place at day time. Activity regarding catalyst synthesis is performed in the prep lab in Chemistry Hall D, first floor, while operation of the rig is performed in the first floor of Chemistry Hall D.

Nitrogen physisorption and chemisorption are performed in K5, 4th floor, and includes use of liquid nitrogen at 77 K and hydrogen gas at high temperature, respectively. Temperature-programmed reduction is performed in Chemistry Hall D, 2nd floor and uses 7 % hydrogen in argon as reduction gas, and also involves high temperatures. All the characterizations will be performed within working hours.

Forutsetninger, antakelser og forenklinger
[Ingen registreringer]

Vedlegg



Apparaturkort.pdf
Al.pdf
perr.pdf
H2.pdf
Co.pdf
He.pdf
Ti.pdf
CO.pdf
N2.pdf

Referanser

[Ingen registreringer]



Oppsummering, resultat og endelig vurdering

I oppsummeringen presenteres en oversikt over farer og uønskede hendelser, samt resultat for det enkelte konsekvensområdet.

Farekilde: Use of Chemicals; Perhanic Acid, Cobalt Nitrate Hexahydrate and Alumina and Titania

Uønsket hendelse: Coming in contact with the chemicals; skin contact, eye contact, ingestion and/or inhalation

Konsekvensområde: Helse Risiko før tiltak:  Risiko etter tiltak: 

Farekilde: Use of heating cabinet (110 C)

Uønsket hendelse: Burns/scalds

Konsekvensområde: Helse Risiko før tiltak:  Risiko etter tiltak: 


Farekilde: Use of flammable/explosive gas (H2)

Uønsket hendelse: Gas leak

Konsekvensområde: Helse Risiko før tiltak:  Risiko etter tiltak: 
Materielle verdier Risiko før tiltak:  Risiko etter tiltak: 

Farekilde: Use of electrical equipment

Uønsket hendelse: Shocks and/or ignition of a potential gas leak

Konsekvensområde: Helse Risiko før tiltak:  Risiko etter tiltak: 
Materielle verdier Risiko før tiltak:  Risiko etter tiltak: 

Farekilde: Use of toxic gas (CO)

Uønsket hendelse: Inhalation of CO

Konsekvensområde: Helse Risiko før tiltak:  Risiko etter tiltak: 

Farekilde: Calcination of the catalyst

Uønsket hendelse: Inhalation of NOx gases that are formed

Konsekvensområde: Helse Risiko før tiltak:  Risiko etter tiltak: 

Norges teknisk-naturvitenskapelige universitet (NTNU)

Unntatt offentlighet jf. Offentlighetsloven § 14

Utskriftsdato:

10.06.2019

Utskrift foretatt av:

Erik Andreas Jørgensen

Side:

3/16



Farekilde: Calcination of the catalyst

Uønsket hendelse: High temperature surfaces

Konsekvensområde: Helse

Risiko før tiltak:  Risiko etter tiltak: 

Farekilde: Operation of FT-rig

Uønsket hendelse: Burns/scalds from hot surfaces

Konsekvensområde: Helse

Risiko før tiltak:  Risiko etter tiltak: 

Uønsket hendelse: Pressure blow-out when draining the condensate pots

Konsekvensområde: Helse

Risiko før tiltak:  Risiko etter tiltak: 

Endelig vurdering



Involverte enheter og personer

En risikovurdering kan gjelde for en, eller flere enheter i organisasjonen. Denne oversikten presenterer involverte enheter og personell for gjeldende risikovurdering.

Enhet /-er risikovurderingen omfatter

- Institutt for kjemisk prosesssteknologi

Deltakere

Ljubisa Gavrilovic

Erik Andreas Jørgensen

Lesere

Estelle Marie M. Vanhaecke

Anne Hoff

Andre involverte/interessenter

[Ingen registreringer]

Følgende akseptkriterier er besluttet for risikoområdet Risikovurdering: Helse, miljø og sikkerhet (HMS):

Helse



Materielle verdier



Omdømme



Ytre miljø



**Oversikt over eksisterende, relevante tiltak som er hensyntatt i risikovurderingen**

I tabellen under presenteres eksisterende tiltak som er hensyntatt ved vurdering av sannsynlighet og konsekvens for aktuelle uønskede hendelser.

Farekilde	Uønsket hendelse	Tiltak hensyntatt ved vurdering
Use of Chemicals; Perhanic Acid, Cobalt Nitrate Hexahydrate and Alumina and Titania	Coming in contact with the chemicals; skin contact, eye contact, ingestion and/or inhalation	Personal protection
Use of heating cabinet (110 C)	Burns/scalds	Personal protection
Use of flammable/explosive gas (H ₂)	Gas leak	Leak test
Use of electrical equipment	Shocks and/or ignition of a potential gas leak	
Use of toxic gas (CO)	Inhalation of CO	Leak test
	Inhalation of CO	CO-detectors
Calcination of the catalyst	Inhalation of NO _x gases that are formed	Pre-installed ventilation in the rig
	High temperature surfaces	Personal protection
Operation of FT-rig	Burns/scalds from hot surfaces	Personal protection
	Pressure blow-out when draining the condensate pots	

Eksisterende og relevante tiltak med beskrivelse:**Personal protection**

Use suitable personal protection for the various procedures

Leak test

Leak test prior to operation

CO-detectors

There is installed local CO-sniffers at the rig and handheld CO-detectors are also available for use.

Pressure release

[Ingen registreringer]

Pre-installed ventilation in the rig

[Ingen registreringer]



Risikoanalyse med vurdering av sannsynlighet og konsekvens

I denne delen av rapporten presenteres detaljer dokumentasjon av de farer, uønskede hendelser og årsaker som er vurdert. Innledningsvis oppsummeres farer med tilhørende uønskede hendelser som er tatt med i vurderingen.

Følgende farer og uønskede hendelser er vurdert i denne risikovurderingen:

- **Use of Chemicals; Perhanic Acid, Cobalt Nitrate Hexahydrate and Alumina and Titania**
 - Coming in contact with the chemicals; skin contact, eye contact, ingestion and/or inhalation
- **Use of heating cabinet (110 C)**
 - Burns/scalds
- **Use of flammable/explosive gas (H2)**
 - Gas leak
- **Use of electrical equipment**
 - Shocks and/or ignition of a potential gas leak
- **Use of toxic gas (CO)**
 - Inhalation of CO
- **Calcination of the catalyst**
 - Inhalation of NOx gases that are formed
 - High temperature surfaces
- **Operation of FT-rig**
 - Burns/scalds from hot surfaces
 - Pressure blow-out when draining the condensate pots



Detaljert oversikt over farekilder og uønskede hendelser:

Farekilde: Use of Chemicals; Perhanic Acid, Cobalt Nitrate Hexahydrate and Alumina and Titania

Uønsket hendelse: Coming in contact with the chemicals; skin contact, eye contact, ingestion and/or inhalation
.....

Sannsynlighet for hendelsen (felles for alle konsekvensområder): **Lite sannsynlig (2)**

Kommentar:

Using the suggested protection minimizes the probability of exposure.

Konsekvensområde: Helse

Vurdert konsekvens: **Stor (3)**

Kommentar: The chemicals are harmful, so if exposed the consequence is large.

Risiko:





Farekilde: Use of heating cabinet (110 C)

Uønsket hendelse: Burns/scalds

.....

Sannsynlighet for hendelsen (felles for alle konsekvensområder): **Lite sannsynlig (2)**

Kommentar:

Use of personal protection minimizes the risk.

Konsekvensområde: Helse

Vurdert konsekvens: **Middels (2)**

Kommentar: The temperature that is used corresponds to a medium consequence.

Risiko:





Farekilde: Use of flammable/explosive gas (H2)

Uønsket hendelse: Gas leak

Sannsynlighet for hendelsen (felles for alle konsekvensområder): **Lite sannsynlig (2)**

Kommentar:

Even though a leak test is performed, minimizing the probability of a leak, it still may happen afterwards.

Konsekvensområde: Helse

Vurdert konsekvens: **Svært stor (4)**

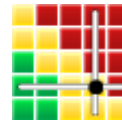
Kommentar: A H2 gas leak may cause an explosion and if someone is closeby when that happens they may be seriously injured.

Risiko:

Konsekvensområde: Materielle verdier

Vurdert konsekvens: **Svært stor (4)**

Kommentar: If the leak is undetected it may cause an explosion that destroys a lot of valuable equipment.

Risiko:




Farekilde: Use of electrical equipment

Uønsket hendelse: Shocks and/or ignition of a potential gas leak

Sannsynlighet for hendelsen (felles for alle konsekvensområder): **Lite sannsynlig (2)**

Kommentar:

All electrical equipment is grounded, minimizing the risk shocks.

Konsekvensområde: Helse

Vurdert konsekvens: **Liten (1)**

Kommentar: The current passing through the electrical equipment is not large enough to be harmful.

Risiko:



Konsekvensområde: Materielle verdier

Vurdert konsekvens: **Stor (3)**

Kommentar: The equipment may be broken

Risiko:





Farekilde: Use of toxic gas (CO)

Uønsket hendelse: Inhalation of CO

.....

Sannsynlighet for hendelsen (felles for alle konsekvensområder): **Svært lite sannsynlig (1)**

Kommentar:

The CO detectors will sound the alarm if the concentration of CO is above a certain level, minimizing the probability of long-term exposure. Two CO detectors are installed in the rig, and sentral detectors are installed in the hall. With additional use of handheld detector, the probability of all of them failing at the same time is very low.

Konsekvensområde: Helse

Vurdert konsekvens: **Katastrofal (5)**

Kommentar: Malfunctioning CO detectors can cause a person to be exposed for CO over a longer period, which can cause serious harm and potentially death.

Risiko:





Farekilde: Calcination of the catalyst

Uønsket hendelse: Inhalation of NOx gases that are formed

Sannsynlighet for hendelsen (felles for alle konsekvensområder): **Svært lite sannsynlig (1)**

Kommentar:

The calcination takes place in a ventilated rig and the reactor system is closed. The calcination is performed at ambient pressure, minimizing the probability of a leak.

Konsekvensområde: Helse

Vurdert konsekvens: **Middels (2)**

Kommentar: The amount of NOx formed is very small.

Risiko:**Uønsket hendelse: High temperature surfaces**

Sannsynlighet for hendelsen (felles for alle konsekvensområder): **Lite sannsynlig (2)**

Kommentar:

Using personal protection minimizes the probability of exposure.

Konsekvensområde: Helse

Vurdert konsekvens: **Stor (3)**

Kommentar: If exposed, the temperature is high enough to cause severe burns.

Risiko:



Farekilde: Operation of FT-rig

Uønsket hendelse: Burns/scalds from hot surfaces

Sannsynlighet for hendelsen (felles for alle konsekvensområder): **Lite sannsynlig (2)**

Kommentar:

Hot surfaces are isolated. Use of personal protection minimized the risk of exposure.

Konsekvensområde: Helse

Vurdert konsekvens: **Stor (3)**

Kommentar: The temperature is at maximum 350 C, which can cause severe burns if exposed to it.

Risiko:

Uønsket hendelse: Pressure blow-out when draining the condensate pots

Contains hot wax, olefins and paraffins.

Sannsynlighet for hendelsen (felles for alle konsekvensområder): **Sannsynlig (3)**

Kommentar:

[Ingen registreringer]

Konsekvensområde: Helse

Vurdert konsekvens: **Middels (2)**

Kommentar: [Ingen registreringer]

Risiko:




Oversikt over besluttede risikoreducerende tiltak:

Under presenteres en oversikt over risikoreducerende tiltak som skal bidra til å reduseres sannsynlighet og/eller konsekvens for uønskede hendelser.

Detaljert oversikt over besluttede risikoreducerende tiltak med beskrivelse:



Detaljert oversikt over vurdert risiko for hver farekilde/uønsket hendelse før og etter besluttede tiltak

Norges teknisk-naturvitenskapelige universitet (NTNU)

Unntatt offentlighet jf. Offentlighetsloven § 14

Utskriftsdato:

10.06.2019

Utskrift foretatt av:

Erik Andreas Jørgensen

Side:

16/16
